Abstract

Steady-state Ab Initio Laser Theory and its Applications in Random and Complex Media

Li Ge
2010

A semiclassical theory of single and multimode lasing, the Steady-state Ab Initio Laser Theory (SALT), is presented in this thesis. It is a generalization of the previous work by Türeci *et al* which determines the steady-state solutions of the Maxwell-Bloch (MB) equations, based on a set of self-consistent equations for the modal fields and frequencies expressed as expansion coefficients in the basis of the constant-flux (CF) states. Multiple techniques to calculate the CF states in 1D and 2D are discussed. Stable algorithms for the SALT based on the CF states are developed, which generate all the stationary lasing properties in the multimode regime (frequencies, thresholds, internal and external fields, output power and emission pattern) from simple inputs: the dielectric function of the passive cavity, the atomic transition frequency, and the transverse relaxation time of the lasing transition. We find that the SALT gives excellent quantitative agreement with full time-dependent simulations of the Maxwell-Bloch equations after it has been generalized to drop the slowly-varying envelope approximation. The SALT is infinite order in the non-linear hole-burning interaction; the widely used third order approximation is shown to fail badly. Using the SALT we investigate various lasers including the asymmetric resonance cavity (ARC) lasers and random lasers. The mode selection and the quasi-exponential power growth observed in quadrupole lasers by Gmachl *et al* are qualitatively reproduced, and strong modal interaction in random lasers is discussed. Lasers with a spatial inhomogeneous gain profile are considered, and new modes due to the scattering from the gain boundaries are analyzed in 1D cavities.

Steady-state Ab Initio Laser Theory and its Applications in Random and Complex Media

A Dissertation
Presented to the Faculty of the Graduate School
of
Yale University
in Candidacy for the Degree of
Doctor of Philosophy

Li Ge

Dissertation Director: A. Douglas Stone

May 2010

Copyright © 2010 by Li Ge
All rights reserved.

Contents

List of Figures

Acknowledgements

There are many friends and colleagues who deserve my heartfelt thanks for having helped me through my years at Yale. I'm deeply indebted to my thesis advisor Douglas Stone for his guidance, patience, and support, on both a educational and a personal level; they were essential to the completion of this thesis. I have benefited enormously from his knowledge in a wide range of fields, his extraordinary insights of approaching and analyzing complex problems, and his enthusiasm for physics. They have greatly inspired me and are invaluable for my further scientific career.

I'm grateful to have Hakan Türeci as a friend and a collaborator. Although there was only a short overlap between our stays at Yale, I feel that I have known him for many years and I treasure our friendship. The work he did with my advisor on the "modernization" of the semi-classical laser theory is largely the foundation of this thesis, and I'm thankful for his stimulating discussions in the course of our collaboration.

I would also like to express my appreciation to all the other previous and current members of the Stone group with whom I became acquainted. Stefan Rotter wrote the prototype of the 2D CF solver in polar coordinates, which I modified in the study of the 2D random lasers and the asymmetric resonant cavity lasers. His warmheartedness and love for music deeply impressed me. Robert Tandy did the numerical integration of the Maxwell-Bloch equations in our verification of the SALT theory, through which we found the numerical criterion of the breakdown of the stationary inversion approximation, impelling me to derive the perturbative corrections. Yidong Chong helped me migrating the non-linear SALT solver in MatLab to Octave on the Bulldog clusters, which made the statistical study of the random lasers possible. Harald Schwefel kindly showed me how to use the ray simulation program for wave-chaotic cavities, although I ended up writing my own in MatLab. Jens Nöckel aroused my curiosity about the vectorial generalization of the SALT equation, and his thesis helped clarifying the question I had about the modified Fresnel rule on a curved surface. Evgenii Narimanov explained to me carefully various aspects of meta-materials, and I'm grateful that he agreed to be my external reader upon a short notice.

Special thanks go to Prof. Hui Cao and her group. I learned a lot about lasers and optics in general through our collaboration and in the nonlinear optics class she taught with my advisor. I would also like to extend my thanks to Prof. Yoram Alhassid and Prof. Sohrab Ismail-Beigi for their careful reading of this thesis.

Yang Bai, John Challis, Qi Yan, Hanghui Cheng, Hui Tang, Xinhui Lu, Jiji Fan, and other fellow graduate students have added so much fun to my study and life. I wish you all success in the career you choose.

Finally, my parents, Yiping Ge and Yuanzhen Liu, and my wife, Qijuan Li. Without your unconditional love and support I couldn't have made it this far.

Chapter 1

Introduction

From price scanners in supermarkets to DVD and Blue-ray players at home, the application of lasers are ubiquitous in our daily lives. In the world of science, lasers are used widely in spectroscopy, microscopy, material processing, remote sensing and etc. This year (2010) marks the fifty-year anniversary of the inventions of the ruby laser and the gas laser, and during this period five Nobel Prizes in Physics have been given to researches directly related to lasers, with the first one in 1964 to Charles H. Townes, Nicolay G. Basov and Aleksandr M. Prokhorov for their fundamental work leading to the constructions of lasers and the most recently one in 2000 to Zhores I. Alferov and Herbert Kroemer for developing semiconductor heterostructures which makes semiconductor lasers possible[1].

The word "laser" is the acronym for Light Amplification by the Stimulated Emission of Radiation, and its invention can be dated back to more than ninety years ago when Albert Einstein introduced the concept of the photon and predicted the phenomenon of the stimulated emission [1]. The laser is a device that produces a coherent light beam with low-divergence at frequencies ranging from the infrared to ultraviolet region, and it has two essential components: a laser cavity that traps light and supplies the needed optical feedback, and a gain medium that amplifies light in the presence of an external pump. The early lasers are all of Fabry-Perot type (see Fig. 1.1(a)) where the light undergoes multiple reflections between two facing mirrors, one of 100% reflectivity and the other slightly less (about 95% in the first ruby laser). Due to the good confinement of light in the cavity,

[1]The 2000 Nobel Prize in physics was also shared by Jack S. Kilby for inventing the integrated circuit.

the openness of the cavity is often neglected when predicting possible lasing modes in the standard treatment. These modes are known as "closed cavity modes", which are the solutions of the Helmholtz equation (derived from Maxwell's equations)

$$\left[\nabla^2 + \frac{\epsilon_c(\boldsymbol{x})\omega^2}{c^2}\right]\phi(\boldsymbol{x},\omega) = 0 \tag{1.1}$$

with vanishing amplitude at the cavity boundaries. $\epsilon_c(x)$ is the dielectric function of the passive cavity (without the gain medium).

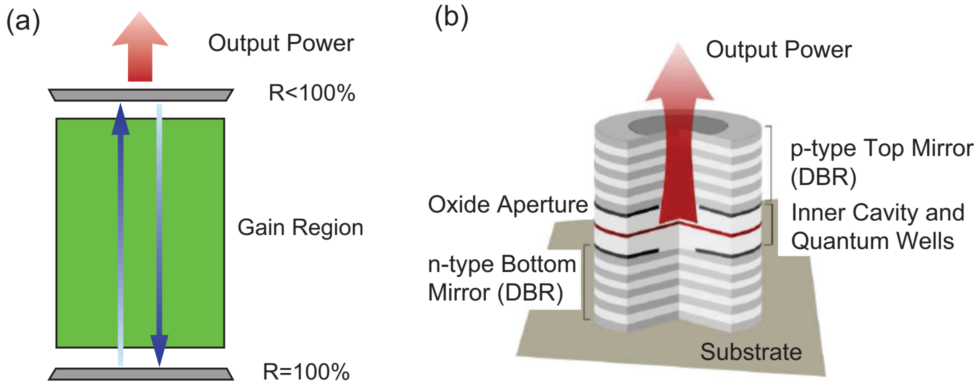

Figure 1.1: Schematic diagram of (a) a Pabry-Perot laser cavity and (b) a VCSEL device [2].

Modern laser cavities

One shortcoming of Fabry-Perot lasers is that they cannot maintain stable single-mode operation under high-speed modulation [3, 4]. The advent of dynamic single mode (DSM) lasers [5, 6] solves this problem. Due to their small sizes (a few wavelengths of the emitted light), the frequency spacing of the axial modes is large compared with the gain width and typically only one axial mode is underneath the gain curve, which gives rise to robust single-mode operation. Depending on whether the diffraction grating is incorporated inside the gain region or outside, DSM lasers are classified as distributed feedback (DFB) lasers and distributed Bragg Reflector (DBR) lasers. The lasing frequency in these lasers can be tuned precisely by varying the spatial period of the diffraction grating. One important design of DFB lasers is the vertical cavity surface emitting laser (VCSEL) shown in Fig. 1.1(b). Thanks to its small size and vertical emission direction, tens of thousands of VCSELs can be fabricated and tested simultaneously on a wafer. VCSELs' high coupling efficiency to optical fibers and good reliability make them key to fiber optics and data communications [7, 8], and tens of millions of VCSEL based transceivers had been deployed as of 2001 [9].

As fabrication techniques advance, novel science-driven laser cavities were introduced which can be arbitrarily complex or even random spatially. Among them are dielectric micro-disk and micro-sphere based lasers [10, 11, 12, 13, 14, 15], photonic crystal slab (PhCS) defect mode lasers [16, 17] and random lasers [18, 19].

The experimental group led by Richard K. Chang at Yale have studied micro-disk and micro-sphere based lasers for more than two decades [20, 21, 22]. Light confinement in these lasers comes from the high reflectivity at the dielectric-air interface when the incident angle is above the critical angle. Thus they support high-Q cavity modes even at the scale of a few microns. These modes circulate around the cavity within a few wavelengths from the perimeter and are known as the "whispering-gallery" (WG) modes [23]. The high quality factor of these modes helps to reduce the lasing threshold, but it also limits the output power as the main leakage mechanism is the evanescent tunneling due to the curvature of the boundary. The rotational symmetry of the micro-disks and micro-spheres determines the emission is also isotropic, and to extract light from these cavities efficiently one needs to couple a waveguide or a fiber taper [24, 25, 26, 27] to them by evanescent waves. This inconvenience further limits their application as a micro-scale on-chip coherent light source. Nöckel and Stone [28] suggested that directional emission can be achieved in these micro-lasers by smoothly deforming their boundary, giving rise to the asymmetric resonant cavity (ARC) lasers. By "phase space engineering", i. e., monitoring the ray motions inside the cavity on the Poincaré surface-of-section (SOS) [29], one can predict the output directionality of lasing modes, which has then been confirmed by a number of experiments [14, 30, 31, 32].

PhCS lasers are made of two-dimensional photonic crystals with finite vertical extension. The light confinement within the plane is achieved by Bragg scattering of the

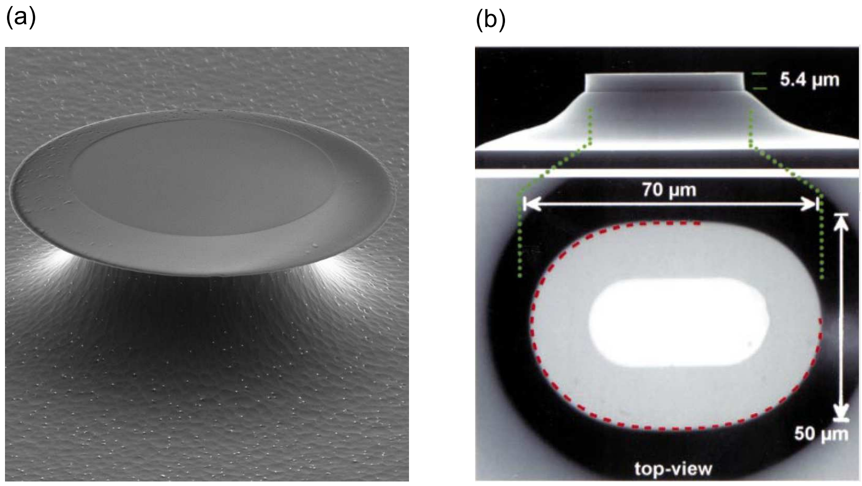

Figure 1.2: Scanning electron microscope images of (a) a micro-disk laser [33] and (b) a quadrupole cylindrical laser [14].

periodic dielectric structures. A manually introduced single defect [34, 35] or unavoidable imperfections during the fabrication [36] lead to spatially localized modes with frequencies near the edges of photonic band gap, which have high quality factors and low thresholds. The random lasers (RLs), like the PhCS, have no traditional resonator to trap light. In its most basic realization, a RL consists of a random aggregate of particles which scatter light and have gain or are embedded in a background medium with gain [37, 38, 39, 40, 41, 42, 43, 44, 45, 46, 47]. Photons generated by stimulated emission are only very weakly "confined" by multiple scattering as it leaks out of the medium. When operated outside the strongly disordered regime, the photon escape is so rapid that *the medium exhibits no isolated resonances* in the absence of gain. Despite the lack of sharp resonances, the laser emission from RLs was observed to have the essential properties of conventional lasers: the appearance of coherent emission with line-narrowing above a series of thresholds, and uncorrelated photon statistics above threshold indicative of gain saturation [37, 39, 42, 44]. Newly proposed deterministic aperiodic lasers intermediate between PhCS lasers and random lasers by having structures determined by mathematical inflation roles (e. g., the Fibonacci series and the Penrose tilting). One unique property of aperiodic structures is the coexistence of extended, critically-localized and exponentially-localized modes [48, 49, 50].

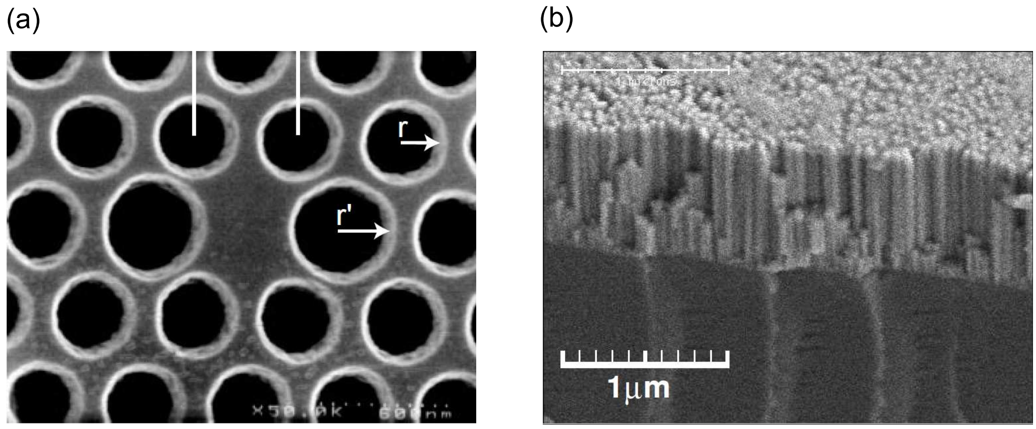

Figure 1.3: Scanning electron microscope images of (a) a photonic crystal slab laser with hexagonal array of air holes in a thin InGaAsP membrane [16] and (b) ZnO nanorods on a sapphire substrate [44].

Treating open cavities

One of the theoretical challenges of modeling these novel lasers is the correct treatment of the openness of the cavity. One way to go beyond the closed cavity approximation is using the quasi-bound (QB) modes or resonances [15, 28, 51]. In an arbitrary passive cavity described by a linear dielectric function $\epsilon_c(\boldsymbol{x})$ the QB modes can be defined in terms of an electromagnetic scattering matrix S for the cavity. This matrix relates incoming waves at wavevector k (frequency $\omega = ck$) to all outgoing asymptotic channels. The QB modes are then the eigenvectors of the passive cavity S-matrix with eigenvalue equal to infinity, i. e., there are outgoing waves but no incoming waves. Equivalently, the QB modes can be defined as the solutions of the wave equation (1.1) both inside the cavity and outside, with the outgoing boundary condition. Although QB modes have been used extensively in the standard open cavity analysis, we emphasize that they are not orthogonal to each other and the photon flux outside the gain medium is not conserved in QB modes. Therefore, they are unsuitable for describing complex and random lasers where the modal interaction is important and a multi-mode laser theory must be applied. This difficulty is overcome by the introduction of the constant-flux (CF) states by Türeci, Stone *et al* [52]. As the name suggests, the CF states conserve the photon flux outside the gain region, and it was shown that the CF states satisfy a bi-orthogonality relation with their dual functions and they form a complete basis for the lasing modes. In high-Q cavities the QB modes are similar to the CF states but distinct; in more open cavities they can be very different with the extreme example being the random lasers in the quasi-ballistic regime (Section 3.5).

Light-matter interaction

Besides the correct treatment of the openness of the passive cavity, a successful laser theory also needs to treat the interaction of light and the gain medium properly. Otherwise, one can only "post-dict" what the lasing modes are by comparing the experimental results with the cavity modes [14, 51]. The gain medium can be a collection of ions (e. g., in solid-state lasers such as the ruby laser), atoms (in gas lasers), molecules (in dye lasers) or heterostructures in semiconductor lasers, which we will refer to as "atoms" in general. For the laser action to happen, the gain medium needs to be inverted, meaning there are more atoms in an excited state than in the ground state. The simplest approach to take into account the dynamics of the gain medium is using rate equations [3, 53], which deal with the temporal changes of light intensity in the cavity (cavity rate equation) and the inversion of the gain media (atomic rate equation). The rate equation approach is useful in studying global properties of a laser such as modal intensities and thresholds [53], but since it is motivated heuristically some important aspects are left out. For example, there is no equation in the rate equation approach that governs the spatial variation of the electric field (light); it is either completely neglected or one assumes each lasing mode is one cavity mode. As a result, coherent effects such as mode instability cannot be explained by the rate equations [54].

The deficiency is remedied in the semiclassical laser theory developed independently by Haken [53] and Lamb [55] in the 1960s. In the semiclassical laser theory the electric field $E(\boldsymbol{x}, t)$ is treated as a classical quantity satisfying the Maxwell's equations and the gain medium is described quantum-mechanically by a density matrix. This leads to coupled nonlinear equations of the electric field, the induced polarization and population inversion in the gain medium; these fundamental equations are known as the Maxwell-Bloch (MB) equations (Chapter 2) for a medium consisting of two-level atoms. It should be noted that spontaneous emission (SE) is not included in the semi-classical laser theory[2]. As a result, the semiclassical laser theory gives clear thresholds, below which the corresponding lasing modes and the polarizations are both zero and above which the lasing peaks are taken to be infinitely sharp. Due to the nonlinear coupling terms the MB equations cannot be solved analytically in the multi-mode regime without invoking some approximations. The conventional approaches either involve brute-force numerical simulations [38, 57, 58, 59] or expansions of the lasing modes in the closed cavity modes [53, 60]. The first approach can be employed to study the steady-state solutions as well as the transient dynamics, but it becomes numerically intractable in the short wave length for complex geometries especially in 3D. It is also difficult to gain qualitative physical insights from such an approach. The modal expansion approach solves for the steady-state solutions of the MB equations in the form of periodic or multi-periodic waves. The adoption of closed cavity modes simplifies the mathematical description, but it also limits the application of this method since no prediction can be made for the power and directionality of the output beams without some *ad hoc* assumptions.

Gain saturation and spatial hole burning

It is well known that lasers with a homogeneously broadened gain medium maintain single-mode operation above threshold if the gain is saturated uniformly in space (e. g., in an ideal ring laser) [3, 61]. However, lasing modes in most cavities have spatial intensity modulation, which creates an inhomogeneous inverted population in space. This phenomenon is known as the spatial hole burning which is the most significant effect leading to multimode operation: Cavity modes with maximum intensity located at the points with less depleted or undepleted inversion feel less gain competition, and they start to oscillate once the pump power is sufficiently strong. One challenge in finding the steady-state solutions of the MB equations is how to treat the above described nonlinear dependency of the population inversion $D(\boldsymbol{x}, t)$ on the electric field correctly. In his book Haken uses the

[2]Recent efforts have been made to include the SE by adding a classical noise term in the numerical simulations of the MB equations [56].

stationary inversion approximation (SIA) $D(\boldsymbol{x},t) \approx D(\boldsymbol{x})$ and derives [53]

$$D(\boldsymbol{x}) = \frac{D_0}{1 + 2T_1\Gamma(\omega^\mu)I_\mu|\phi_\mu(\boldsymbol{x})|^2} \tag{1.2}$$

for single-mode (the μth closed-cavity mode $\phi_\mu(\boldsymbol{x})$) laser action, which we will refer to as the infinite-order nonlinearity. In this equation I_μ and ω^μ are the intensity and frequency of the μth mode, D_0 indicates the pump strength, T_1 is the non-radiative relaxation rate of the inversion, and $\Gamma(\omega^\mu)$ is a frequency-dependent weighting factor, which when combined with $I_\mu|\phi_\mu(\boldsymbol{x})|^2$ gives the stimulated transition probability. In the multi-mode regime, however, the most pursued treatment of $D(\boldsymbol{x})$ is expanding the nonlinearity to the second-order:

$$D(\boldsymbol{x}) \approx D_0\left(1 - 2T_1\sum_\mu \Gamma(\omega^\mu)I_\mu|\phi_\mu(\boldsymbol{x})|^2\right). \tag{1.3}$$

By inserting this expression into the MB equations one derives the Haken-Sauermann equations [61] for the steady-state intensity I_ν:

$$1 - \frac{\kappa_\mu}{D_0} = \sum_\nu \Gamma(\omega^\nu)A_{\mu\nu}I_\nu, \tag{1.4}$$

where κ_μ is the cavity decay rate. The matrix $A_{\mu\nu}$ is defined as the overlapping integral $\int d\boldsymbol{x}|\phi_\mu(\boldsymbol{x})|^2|\phi_\nu(\boldsymbol{x})|^2$, and it describes the modal interaction of the closed-cavity modes $\phi_\mu(\boldsymbol{x}), \phi_\mu(\boldsymbol{x})$. The Haken-Sauermann equations are good at threshold but breaks down at high pump power. Fu and Haken [60] go beyond the approximation (1.3) and take into account the infinite order nonlinearity (1.2) in a 1D edge-emitting laser, but it is still of limited use due to the framework of closed-cavity modes.

The first effort to solve for the steady-state multimode solutions of the MB equation with correct treatments of the openness of the cavity and the infinite order nonlinearity was reported in Ref. [52] by Türeci, Stone *et al.* By assuming the scalar electric field has the multi-periodic form $E(\boldsymbol{x},t) = \sum_\mu \Psi_\mu(\boldsymbol{x})\exp(i\omega^\mu t) + c.c.$ the authors derived the fundamental equation of Steady State Ab Initio Laser Theory (SALT) assuming the slowly-varying envelope approximation (SVEA) holds. Later in this thesis we will derive and use extensively the corresponding equation without the SVEA. These authors introduced the key concept of the constant flux states and expanded the complex amplitude $\Psi_\mu(\boldsymbol{x})$ in the constant-flux basis $\{\phi_m(\boldsymbol{x}, \omega^\mu)\}$, $\Psi_\mu(\boldsymbol{x}) = \sum_m a_m^\mu \phi_m(\boldsymbol{x}, \omega^\mu)$. The SALT equation led to an equation for the expansion coefficient a_m^μ:

$$a_m^\mu = \sum_n B_{mn} a_n^\mu. \tag{1.5}$$

The matrix B_{mn} is proportional to the overlapping integral of $\phi_m(\boldsymbol{x}, \omega^\mu)$, $\phi_n(\boldsymbol{x}, \omega^\nu)$ and the saturated gain

$$D(\boldsymbol{x}) = \frac{D_0}{1 + \sum_\mu \Gamma(\omega^\mu)|\Psi_\mu(\boldsymbol{x})|^2}. \tag{1.6}$$

Notice that the lasing frequency ω^μ and amplitude $\Psi_\mu(\boldsymbol{x})$ are to be determined by Eq. (1.5) and they bear no *a priori* relationship to the those of the closed-cavity modes. The authors then showed that using the "single-pole" approximation in which B_{mn} is taken to be diagonal and only a single term is kept in the CF expansion leads to a generalization of the Haken-Sauermann equations to treat openness exactly [52] and the non-linearity to all orders.

Although in this pioneering work the authors only demonstrate the solutions of Eq. (1.5) when B_{mn} can be approximated by a diagonal matrix and within the SVEA, the concepts of the CF states and the fundamental equation (1.5) laid the groundwork for the Steady-state Ab Initio Laser Theory (SALT), which is the main theme of this thesis. My contributions to the SALT include:

- Developed stable algorithms for the self-consistent equation (1.5) in the multi-mode regime (with Türeci and Stone; Chapter 4).
- Removed the slowly-varying envelope approximation (SVEA) which leads to a much better agreement with the numerical integration of the Maxwell-Bloch equations (Section 2.2 and Section 5.1).
- Reformulated the integral equation of the lasing modes as a differential equation clarifying relation to previous work based on the effective index of refraction (Section 2.2).
- Generalized the SALT to treat multi-level lasing schemes (Section 2.3).

- Verified the SALT quantitatively in the regime where the stationary inversion approximation is good by comparing its predictions with the numerical integration of the time-dependent Maxwell-Bloch equations (with Tandy *et al*; Section 5.1).

- Derived perturbative corrections to the SALT by going beyond the stationary inversion approximation and including the lowest non-zero frequency components of the inversion (Section 5.2).

- Developed multiple techniques to calculate CF states in 1D and 2D (Chapter 3).

- Defined the gain-region constant-flux (GRCF) states which are better representations of the lasing modes in the presence of an spatially inhomogeneous gain medium (Section 2.4 and 3.6).

- Proved that the dual functions of constant-flux states bear a simple relationship to constant-flux states themselves and rewrote the biorthogonality relation as an self-orthogonality relation (Section 2.4).

- Applied the SALT to asymmetric resonant cavity (ARC) lasers and random lasers (Chapter 6 and 7).

Overview of this thesis

In Chapter 2 the Maxwell-Bloch equations are introduced, from which the self-consistent equation of the electric field is derived without the slowly-varying envelope approximation. It is shown that the effect of the gain medium can be treated as adding a nonlinear term to the dielectric function of the passive cavity. The resulting equation of the electric field is the central equation of the SALT, and it is shown to be equivalent to that derived in Ref. [52, 62, 63] where the Helmholtz equation satisfied by the electric field is formally inverted by a Green's function by treating the polarization as the source. Starting from multi-level rate equations and assuming that there is only one lasing transition, we show that the dynamics of a multi-level gain structure can be described by generalized Bloch equations, in which the relaxation rate of the polarization and the equilibrium inversion D_0 in the absence of the electric field are nonlinear functions of the pump strength. Next the last scattering surface and the constant-flux state are introduced independent of the geometry of the cavity, and the orthogonality of constant-flux states is proved with a modified inner product. The self-consistent equation of the electric field is then expanded in the basis consisting of constant-flux states, which displays multiple thresholds when the pump strength is increased. In the case of a spatially inhomogeneous gain medium the gain-region constant-flux states are defined, and their self-orthogonality holds inside the gain region. The relationship between the lasing modes at threshold and the poles of the S-matrix of the passive cavity is shown; the latter define the quasi-bound modes, from which the former evolve as the increasing pump strength modifies the cavity dielectric function. Connections between the constant-flux states and the quasi-bound modes are briefly mentioned, and the linear gain model [64] is shown to be an approximation of the Steady-state Ab-initio laser theory at threshold.

In Chapter 3 the constant-flux states in various geometries and the out-going boundary condition they satisfy are shown and analyzed. In a homogeneous one-dimensional edge-emitting laser the complex frequencies of the constant-flux states are approximated and compared with those of the quasi-bound modes. It is shown that there is always a constant-flux state close to a quasi-bound mode in the complex frequency plane when the (real-valued) lasing frequency is close to the real part of the quasi-bound mode; their difference decreases as the cavity Q or lasing frequency increases. In the multi-layer case two methods are introduced to find the constant-flux states. In the first approach the Laplace operator is approximated by the standard three-point finite difference, and the Helmholtz equation satisfied by the constant-flux states are transformed into a generalized eigenvalue problem. In the second approach the constant-flux states in each layer are decomposed into two amplifying waves traveling in opposite directions, and their coefficients in different layers are related by a transfer matrix, which gives a discrete set of constant-flux frequencies when solved with the out-going boundary condition. In the two-layer case where the gain medium resides only in one of the layers, it is shown that the equation determining the constant-flux frequencies is the same as in the single-layer case but with a modified dielectric function of the environment. The whispering-gallery type constant-flux states in a micro-disk are shown to be almost identical to quasi-bound modes; outside they are very different as the amplitude of the quasi-bound mode grows exponentially when $r \to \infty$. The discretized method in polar coordinates is introduced to solve for the constant-flux states in two-dimensional cavities with an arbitrary boundary, and the accuracy of its solutions is tested in a micro-disk laser against the analytical solutions. The discretized method is also capable of finding the constant-flux states in random lasers, which is modeled as an aggregate of nano-particles embedded in a disk gain regime. We find no one-to-one correspondence between constant-flux states and quasi-bound modes although they have similar distributions in the complex frequency plane. At the end of this chapter we introduce two approaches to solve for the gain-region constant-flux states in laser cavities of arbitrary shape. For presenting a complete view of constant-flux states, some results in Ref. [52] are reproduced in Section 3.2 and 3.3. The two-dimensional discretized constant-flux solver and some results on the random lasers are presented in Ref. [65].

In Chapter 4 we first introduce the threshold matrix, whose eigenvalues at the right frequencies give the inverse threshold in the absence of modal interaction. A special case is analyzed where the cavity dielectric function and the pump strength are both constant. In this case the threshold matrix becomes diagonal, leading to a modified line-pulling formula. The lowest non-interacting threshold is the first threshold, and all the others are pushed to larger values when modal interactions are included. Detailed steps of implementing the algorithm of the SALT above threshold are given, and a useful tool, the modified threshold matrix, is introduced; its functions include visualizing the effect of modal interactions on the modes below their thresholds. Using the example of the two-layer case with an inhomogeneous gain medium introduced in Chapter 3, we confirm that expansions of the lasing modes in the constant-flux state basis and in the gain-region constant-flux state give the same thresholds, lasing frequencies, and modal intensities. The advantage of using the latter is that a smaller basis is needed since the gain-region constant-flux states are better representations of the lasing modes in this case. A flow chart of the SALT algorithm is given at the end of this chapter. Some contents of this chapter are presented in Ref. [63, 65, 66].

In Chapter 5 the predictions of the SALT are compared to the numerical integration of the time-dependent Maxwell-Bloch equations. Excellent agreement is achieved when the slowly-varying envelope approximation is dropped from the fundamental equation derived in Ref. [52, 66]. The stationary inversion approximation is shown to be valid when the ratios $\gamma_{\|}/\gamma_{\perp}$ and $\gamma_{\|}/\Delta k$ are small. $\gamma_{\perp}$ and $\gamma_{\|}$ are the relaxation rate of the polarization and the non-radiative relaxation of the inversion respectively, and Δk is the typical frequency spacing of adjacent lasing modes. Perturbative corrections to the stationary inversion approximation are given in terms of the above mentioned two ratios. The material in this chapter is reported in Ref. [62].

In Chapter 6 the SALT is applied to a series of quadrupole lasers experimentally tested in Ref. [14]. The boundaries of these cavities are captured by $R(\phi) = R_0(1 + \epsilon \cos(2\phi))$ with the deformation ϵ varies from 0 to 0.16. The result of the ray model is reviewed, which shows the evolution of cavity modes as the deformation increases. Factors that affect the lasing threshold and output intensity are analyzed. Under reasonable assumption about the spatial pump profile and the material loss (since detailed information is lacking), we reproduce qualitatively the two main observations of the experiment, namely the quasi-exponential increase of the output power as a function of the deformation and the lasing of the bow-tie modes when $\epsilon \geq 0.16$. The former is found to be insensitive to the parameters we choose as long as the cavity loss prevails against the out-coupling loss, while the latter can only be achieved with particular configurations of the spatial pump profile and the cavity loss.

Chapter 7 is a continuation of the work presented in Ref. [65]. The lasing frequencies in a random laser are shown to have two contributions, one from the complex frequency of the dominant constant-flux states and the other from a collective influence of all the constant-flux states. Two regimes of random lasers are then studied. In the diffusive regime we see signs of strong modal interaction, including mode mixing, strong frequency repulsion and strong mode suppression. In the quasi-ballistic regime we find the modal interaction to be stronger. Threshold lasing modes with close frequencies compete strongly for the gain, and one can drive out another even after the latter is turned on. This suppression is not permanent; The "dead" mode can "reincarnate" itself at a higher pump if the system favors it once again. When subjected to pump noises, random lasers in this regime have large intensity fluctuations but relatively stable frequencies. An explanation is given using the SALT. At the end of this chapter we study the pump induced output directionality, showing that it is possible in the quasi-ballistic regime but not in the diffusive regime.

In Chapter 8 we point out the conventional wisdom, which states that there is a one-to-one correspondence between lasing modes and passive cavity modes, fails in the low-Q limit in the presence of an inhomogeneous gain medium. Using the example of a one-dimensional edge-emitting cavity, we show that two types of lasing modes exist: one corresponds to the passive cavity modes with distorted spatial profiles in the gain region, and the other corresponds to the resonant tunneling in the gain-free region, which doesn't exist in the absence of the inhomogeneous gain medium. As the ratio of the lengths of the gain region and gain-free region varies, a pair of modes, one from each type, can disappear and appear at the same frequency, which is similar to what was found in Ref. [64, 67].

Chapter 2

The steady-state ab-initio laser theory

2.1 Maxwell-Bloch equations

In the semiclassical laser theory light is treated as a classical electro-magnetic field and it satisfies Maxwell's equations. If we assume the electric field is transverse ($\nabla \cdot \boldsymbol{E} = 0$), Maxwell's equations take the form of the fundamental wave equation [53, 68]

$$4\pi \ddot{\boldsymbol{P}}(\boldsymbol{x}, t) = c^2 \nabla^2 \boldsymbol{E}(\boldsymbol{x}, t) - \ddot{\boldsymbol{E}}(\boldsymbol{x}, t), \tag{2.1}$$

where $\boldsymbol{P}(\boldsymbol{x}, t)$ is the polarization, including both the electrical response of the gain medium $\boldsymbol{P}_{NL}(\boldsymbol{x}, t)$ and the hosting material $\boldsymbol{P}_L(\boldsymbol{x}, t)$. When coupled to the matter equations to be introduced below, $\boldsymbol{E}(\boldsymbol{x}, t)$ in Eq. (2.1) should be understood as the electric field corresponding to the stimulated emission, including the radiation field caused by the decay of the population inversion $D(\boldsymbol{x}, t)$ and the external seeding signal if it is present. In this thesis we consider geometries in which the electric field and the polarization can be treated as scalars. For example, the electric field in transverse-magnetic (TM) modes of a microdisk laser is perpendicular to the planar surface ($\boldsymbol{E}(\boldsymbol{x}, t) = E(\boldsymbol{x}, t)\hat{\boldsymbol{z}}$). If the medium is isotropic, the polarization also has only a z-component and we can then drop the vectorial symbols in Eq. (2.1). In the following discussion we will drop the arguments of E, P

and D to make the equations more compact.

The dynamical properties of the gain medium are described by the quantum equations of motion of the density matrix, which in its most simple form are the Bloch equations for a two-level atomic system:

$$\begin{aligned} \dot{P}_{NL}^{+} &= -(i\omega_a + \gamma_\perp)P_{NL}^{+} + \frac{g^2}{i\hbar}ED, & (2.2) \\ \dot{D} &= \gamma_\parallel \left(D_0(\boldsymbol{x}) - D\right) - \frac{2}{i\hbar}E\left((P_{NL}^{+})^* - P_{NL}^{+}\right). & (2.3) \end{aligned}$$

In these equations P_{NL}^{+} is the positive frequency part of the polarization ($P_{NL} = P_{NL}^{+} + P_{NL}^{-} = P_{NL}^{+} + c.c.$), $\omega_a = ck_a$ is the atomic transition frequency, g is the dipole matrix element of the atoms, and $\gamma_\perp$ and $\gamma_\parallel$ are the relaxation rates of the polarization P^+ and the inversion D, respectively. Here $c.c.$ stands for the complex conjugate of the previous term as usual. In the absence of the electric field (below threshold) the inversion decays to its equilibrium value $D_0(\boldsymbol{x})$, which represents the strength of the pump, whether it is an optical pump or an electrical current. In this thesis we take $c = 1$ and do not distinguish between frequency and wavevector. Eq. (2.1-2.3) are the fundamental equations of the semiclassical laser theory, known as the Maxwell-Bloch (MB) equations. They are coupled nonlinear equations of the electric field E, the polarization P, and the inversion D. In the remaining part of this chapter we will derive the steady-state ab-initio laser theory (SALT), which gives a set of self-consistent time-independent equations for the steady state solutions of the MB equations.

2.2 Derivation of the steady state equations

In the following discussion we choose to solve for the positive frequency part of the electric field; once E^+ is found, the total electric field is easily obtained by $E = E^+ + E^- = 2\mathrm{Re}[E^+]$. First we rewrite Eq. (2.1) as

$$4\pi\ddot{P}^{+} = \nabla^2 E^{+} - \ddot{E}^{+}, \qquad (2.4)$$

which is exact in the absence of a D.C. electric field. The linear polarization P_L^+ in Eq. (2.4) can be included in the $\ddot{E}^+$ term by introducing the convolution operator $\hat{n}^2(t) \equiv \int dt' n^2(\boldsymbol{x}, t-t') = 1 + 4\pi \int dt' \chi(\boldsymbol{x}, t-t')$, leading to

$$4\pi \ddot{P}^+ = \nabla^2 E^+ - \partial_t^2 \left(\hat{n}^2 E^+\right). \tag{2.5}$$

P^+ now represents the nonlinear polarization P_{NL}^+ only. The conventional treatment of this equation involves the slowly varying envelope approximation (SVEA) [69, 70, 60, 52], which approximate all the second order time derivatives by $-\omega_a^2 + i\omega_a \partial/\partial t$. This approximation is valid when the lasing frequencies ω^μ are close to ω_a ($|\omega^\mu - \omega_a| \ll \omega_a$) which is not necessarily true in a multi-mode laser. Here we don't invoke the SVEA, and the Laplace transform of Eq. (2.5) results in

$$\left[\nabla^2 + \epsilon_c(\boldsymbol{x}, \omega) k^2\right] \tilde{E}^+(\boldsymbol{x}, \omega) = -4\pi k^2 \tilde{P}^+(\boldsymbol{x}, \omega). \tag{2.6}$$

$\epsilon_c(\boldsymbol{x}, \omega) \equiv n^2(\boldsymbol{x}, \omega)$ is the cavity dielectric function of the system. The Laplace transform we use is

$$\mathcal{L}[f] \equiv \frac{1}{2\pi} \int_0^\infty dt\, e^{i(\omega + i\zeta)t} f(t), \quad (0 < \zeta \ll 1) \tag{2.7}$$

and ζ is taken to be zero *after* the integration.

Eq. (2.6) can be formally inverted with a Green's function (determined by the outgoing wave boundary conditions) by treating $\tilde{P}^+(\boldsymbol{x}, \omega)$ as a source [52]. In this chapter we will introduce a different approach to make connection with the common notion of the effect of the gain medium, which states that the gain medium alters the index of refraction of the passive cavity (cavity without gain) to compensate the loss. At the end of this chapter we will compare the method we will use and the Green's function method and show that they are equivalent.

From Eq. (2.6) we see that if P^+ is a linear function of E^+, it can be moved to the left hand side and absorbed into the $\epsilon_c(\boldsymbol{x}, \omega) k^2$ term, giving rise to a modified dielectric function. If we had used the SVEA in deriving Eq. (2.6), then instead of k^2 we would have had k_a^2 in front of P^+, which introduces a small error in the frequency dependence of the effective dielectric function. This is consistent with the expectation that the SVEA is good when the lasing frequency is close to the atomic frequency. To find an expression for $\tilde{P}^+(\boldsymbol{x},\omega)$ in terms of $\tilde{E}^+(\boldsymbol{x},\omega)$, we follow the derivations given in Ref. [52] when solving the matter equations (2.2) and (2.3). Using the rotating wave approximation (RWA) we can rewrite them such that only the positive (or the negative) parts of E and P appear

$$\dot{P}^+ = -(i\omega_a + \gamma_\perp)P^+ + \frac{g^2}{i\hbar}E^+ D, \tag{2.8}$$

$$\dot{D} = \gamma_\parallel \left(D_0(\boldsymbol{x}) - D\right) - \frac{2}{i\hbar}\left(E^+(P^+)^* - c.c.\right) . \tag{2.9}$$

The terms the RWA drops are at frequencies close to $\pm 2\omega_a$, and it can be shown that they are of the order of $\gamma_\parallel/(2\omega_a)$ following the derivation in Section 5.2. Since in most cases $\gamma_\parallel \ll \gamma_\perp \ll 2\omega_a$, the RWA gives very good results and is widely used in atomic physics and related fields. In the steady state the fields E^+ and P^+ are assumed to be multiperiodic in time

$$E^+ = \sum_\mu \Psi_\mu(\boldsymbol{x})\, e^{-i\omega^\mu t}, \quad P^+ = \sum_\mu p_\mu(\boldsymbol{x})\, e^{-i\omega^\mu t}. \tag{2.10}$$

The functions Ψ_μ are the unknown lasing modes and the real numbers ω^μ are the unknown lasing frequencies. Unlike standard approaches [53, 55, 71, 72, 73, 74], here these functions and frequencies are completely general and bear no *a priori* relationship to the normal modes or linear quasi-modes of the passive cavity.

The steady state solution of the MB equations in the form of Eq. (2.10) is possible only when $\dot{D} \approx 0$ [53, 60]. This approximation is known as the stationary inversion approximation (SIA), which enables one to write the amplitude of the polarization oscillating at ω^μ as

$$p_\mu(\boldsymbol{x}) = \frac{g^2}{\hbar}\frac{D(\boldsymbol{x})}{(\omega^\mu - \omega_a) + i\gamma_\perp}\Psi_\mu(\boldsymbol{x}). \tag{2.11}$$

Since $D(\boldsymbol{x})$ depends on $\Psi_\mu(\boldsymbol{x})$ we don't insert the above equation to Eq. (2.6) yet. When the multiperiodic solutions (2.10) and Eq. (2.11) are inserted into Eq. (2.9), the coupling term between the electric field and the polarization becomes

$$E^+(P^+)^* - c.c. \;=\; i\frac{2g^2 D(\boldsymbol{x})}{\hbar}\left\{\sum_\mu \frac{\Gamma(\omega^\mu)}{\gamma_\perp}|\Psi_\mu(\boldsymbol{x})|^2 + \right.$$
$$\left.\sum_{\mu>\nu}\mathrm{Re}\left[\frac{(2\gamma_\perp + i(\omega^\nu-\omega^\mu))\Psi_\mu(\boldsymbol{x})\Psi_\nu^*(\boldsymbol{x})}{(\gamma_\perp + i(\omega^\nu-\omega_a))(\gamma_\perp - i(\omega^\mu-\omega_a))}\, e^{i(\omega^\nu-\omega^\mu)t}\right]\right\}. \quad (2.12)$$

Here $\Gamma(\omega) \equiv \gamma_\perp^2/(\gamma_\perp^2 + (\omega-\omega_a)^2)$ is the homogeneously broadened gain curve. The second term in Eq. (2.12) only exists in the multi-mode regime, and Eq. (2.12) has no time-dependence when there is only one mode lasing. Thus the inversion is strictly stationary in the single-mode regime when the system reaches the steady state. In the multi-mode regime the beating terms represent the interference of modes oscillating at different frequencies, ruling out a strictly stationary inversion. The other time scale in the dynamics of the inversion is $\gamma_\parallel^{-1}$; if this time scale is long compared to the beat periods of the modes, i. e., if $\gamma_\parallel \ll \Delta\omega_{\mu\nu} = |\omega^\mu - \omega^\nu|$, $\forall \mu,\nu$, then these time-varying interference terms average to zero. In addition it must be assumed that $\gamma_\perp \gg \gamma_\parallel$ as we will see in Chapter 5. In these two limits the SIA is valid with high accuracy, and is often used in multi-mode laser theory and realized in lasers of interest. By dropping the second term in Eq. (2.12) we derive the stationary inversion in terms of the pump $D_0(\boldsymbol{x})$

$$D(\boldsymbol{x}) \approx \frac{D_0(\boldsymbol{x})}{1+\sum_\mu \Gamma(\omega^\mu)|\Psi_\mu(\boldsymbol{x})|^2}\,, \quad (2.13)$$

from which we see clearly the effect of spatial hole burning [3, 53]. The gain medium is less saturated at the points where the sum of the frequency-weighted modal intensities is small. Note that the electric field is now measured in the natural unit of $e_c \equiv \hbar\sqrt{\gamma_\perp\gamma_\parallel}/(2g)$, which sets an absolute scale of the nonlinearity; the spatial hole burning effect is important when the amplitude of the electric field is comparable to e_c, whose square times $n_c/2$ gives the saturation intensity [3]. Eq. (2.13) captures the spatial hole burning effect to all orders, and the near threshold third order theory can be obtained by expanding the denominator to the second order in $\Psi_\mu(\boldsymbol{x})$ (it will become clear why it is not called the second order theory in Section 5.1).

Next we replace $D(\boldsymbol{x})$ in Eq. (2.11) by its value given by Eq. (2.13) and Laplace transform $P^+(\boldsymbol{x}, t)$:

$$\tilde{P}^+(\boldsymbol{x}, \omega) \equiv \sum_\mu \frac{p_\mu(\boldsymbol{x})}{2\pi i(\omega - \omega^\mu)} = \sum_\mu \frac{g^2}{\hbar} \frac{D_0}{(\omega^\mu - \omega_a) + i\gamma_\perp} \frac{\Psi_\mu(\boldsymbol{x})}{1 + \sum_\nu \Gamma_\nu |\Psi_\nu(\boldsymbol{x})|^2} \frac{1}{2\pi i(\omega - \omega^\mu)}, \tag{2.14}$$

in which Γ_ν is short for $\Gamma(\omega^\nu)$. Both $\tilde{P}^+(\boldsymbol{x}, \omega)$ and $\tilde{E}^+(\boldsymbol{x}, \omega) = \sum_\mu \frac{\Psi_\mu(\boldsymbol{x})}{2\pi i(\omega - \omega^\mu)}$ in Eq. (2.6) have poles only on the real axis of the complex frequency space after ζ, the small parameter introduced in the Laplace transform, is taken to be zero. Therefore, we can equate the residues of the real poles on both sides of Eq. (2.6) which gives

$$\left[\nabla^2 + \left(\epsilon_c(\boldsymbol{x}) + \frac{\gamma_\perp}{(\omega^\mu - \omega_a) + i\gamma_\perp} \frac{D_0(\boldsymbol{x})}{1 + \sum_\nu \Gamma_\nu |\Psi_\nu(\boldsymbol{x})|^2}\right) k^{\mu 2}\right] \Psi_\mu(\boldsymbol{x}) = 0. \tag{2.15}$$

Here we have changed the notation and $D_0(x)$ is now dimensionless, measured in the natural unit $D_{0c} = \hbar\gamma_\perp/(4\pi g^2)$. The above equation, which we will refer to as the SALT I equation, has been arranged such that one can immediately see that the effect of the gain medium is to add a term

$$\epsilon_g(\boldsymbol{x}, \omega) = \frac{\gamma_\perp}{(\omega - \omega_a) + i\gamma_\perp} \frac{D_0(\boldsymbol{x})}{1 + \sum_\nu \Gamma_\nu |\Psi_\nu(\boldsymbol{x})|^2} \tag{2.16}$$

to the dielectric function. $\epsilon_g(\boldsymbol{x}, \omega)$ in general is complex; its imaginary part is negative (amplifying) when the gain medium is inverted and its value depends on the pump strength; at threshold it compensates the outcoupling loss as well as any cavity loss from the cavity dielectric function. Notice that in our scaled units, $\gamma_\parallel$ doesn't appears in Eq. (2.15), which means the behavior of lasers with different values of $\gamma_\parallel$ are the same up to a simple rescaling in the regime where the SIA is valid.

The set of nonlinear equations (2.15), or their equivalents Eq. (2.19) obtained from the Green's function method to be introduced below, are the central equations of the SALT laser theory. As one can easily see $\Psi_\mu(\boldsymbol{x}) = 0$ is always a solution of Eq. (2.15), but these equations also exhibit a series of thresholds $D_{th}^{(i)}$ in the pump strength. A new mode appears once D_0 surpasses its threshold, it then interacts with itself through the nonlinear hole-burning term in the denominator in Eq. (2.15). At the same time the lasing modes partially suppress other solutions which would turn on in the absence of mode competition.

Because gain is less depleted where the electric field of the existing lasing modes is small, the new modes that turn on as D_0 further increases tend to overlap less in space with the existing lasing modes. Another factor that determines the order of the lasing modes is their position under the homogenously broadened gain curve $\Gamma(\omega)$, which is a Lorentzian function centered at ω_a. The modes in the vicinity of ω_a utilize the available gain better and are more likely to turn on first.

In the Green's function method introduced in Ref. [52] $\tilde{P}^+(x,\omega)$ in Eq. (2.6) is treated as a source, and Eq. (2.6) can be formally inverted with the following Green's function

$$\left[\nabla^2 + \epsilon_c(\boldsymbol{x})k^2\right] G(\boldsymbol{x},\boldsymbol{x}';\omega) = \delta(\boldsymbol{x}-\boldsymbol{x}'). \quad (\boldsymbol{x},\boldsymbol{x}' \in \text{cavity}) \tag{2.17}$$

The boundary condition satisfied by the Green's function is the out-going boundary condition outside the cavity, which eliminates the surface terms in the Green's theorem (see Section 2.4 for details) and yields

$$\tilde{E}^+(\boldsymbol{x},\omega) = -4\pi k^2 \int_{\text{cavity}} dx' G(\boldsymbol{x},\boldsymbol{x}';\omega)\tilde{P}^+(\boldsymbol{x},\omega). \tag{2.18}$$

The Green's function only correctly calculates the electric field inside the cavity, and the external solutions are given by connecting the internal solutions through the outgoing wave conditions. This Green's function only has complex poles with a negative imaginary part, which can be seen from the spectral representation of the Green's function to be introduce in Section 2.4. Therefore, we can repeat what we did in deriving Eq. (2.15) and equate the residues of the real-valued poles on both sides of Eq. (2.18), which gives a self-consistent equation of $\Psi_\mu(x)$:

$$\Psi_\mu(\boldsymbol{x}) = -\frac{\gamma_\perp k^{\mu 2}}{(\omega^\mu - \omega_a) + i\gamma_\perp} \int_{\text{cavity}} d\boldsymbol{x}' \frac{D_0(\boldsymbol{x}')G(\boldsymbol{x},\boldsymbol{x}';\omega^\mu)\Psi_\mu(\boldsymbol{x}')}{1+\sum_\nu \Gamma_\nu |\Psi_\nu(\boldsymbol{x}')|^2}. \tag{2.19}$$

There are two ways to prove that Eq. (2.19), which will refer to as the SALT II equation, is equivalent to the SALT I equation (2.15). First, the SALT II equation can be obtained by inverting the SALT I equation with the Green's function defined in Eq. (2.17). Second, the two SALT equations lead to the same equation once we expand all the spatial varying quantities in the constant-flux basis to be introduce in Chapter 2.4. The two forms are of course equivalent.

Vectorial generalization of the SALT

Below we outline the steps to generalize the SALT I equation (2.15) to its full vectorial form. First we remove the transverse condition $\nabla \cdot \boldsymbol{E} = 0$ which is valid when the dielectric function varies on a length scale much larger or much smaller than the wavelength. The dielectric function and the Laplacian in the wave equation (2.1) then need to be replaced by the dielectric tensor $\hat{\epsilon}_c(\boldsymbol{x})$ and the operator $(-\nabla \times \nabla \times)$, respectively. Notice the Bloch equations are vectorial in nature [53], and the dipole matrix element $g^2(\boldsymbol{x})$ in Eq. (2.2) should be treated as a position-dependent tensor

$$\hat{g^2}(\boldsymbol{x}) \equiv \boldsymbol{g}(\boldsymbol{x}) \cdot (\boldsymbol{g}^T(\boldsymbol{x})) = (g(\boldsymbol{x})_x, g(\boldsymbol{x})_y, g(\boldsymbol{x})_z)^T \cdot (g(\boldsymbol{x})_x, g(\boldsymbol{x})_y, g(\boldsymbol{x})_z)\,, \tag{2.20}$$

which is symmetric $(\hat{g^2}(\boldsymbol{x}))_{ij} = (\hat{g^2}(\boldsymbol{x}))_{ji} = g_i(\boldsymbol{x})g_j(\boldsymbol{x})$. The scalar product $g^2 E(\boldsymbol{x})$ is then replaced by $\hat{g^2}(\boldsymbol{x}) \cdot \boldsymbol{E}(\boldsymbol{x})$ in which $\boldsymbol{E}(\boldsymbol{x}) = \sum_\mu \boldsymbol{\Psi}_\mu(\boldsymbol{x}) \exp(-i\omega^\mu t) + c.\,c.$ is now a column vector. Similarly, Eq. (2.11) still holds with $g^2\Psi_\mu(\boldsymbol{x})$ replaced by $\hat{g^2}(\boldsymbol{x}) \cdot \boldsymbol{\Psi}_\mu(\boldsymbol{x})$, which leads to a modified expression for the stationary inversion:

$$D(\boldsymbol{x}) \approx \frac{D_0(\boldsymbol{x})}{1 + \sum_\mu \frac{4\Gamma_\mu}{\hbar^2 \gamma_\parallel \gamma_\perp} \boldsymbol{\Psi}_\mu^\dagger(\boldsymbol{x}) \cdot \hat{g^2}(\boldsymbol{x}) \cdot \boldsymbol{\Psi}_\mu(\boldsymbol{x})}\,. \tag{2.21}$$

To emphasize the tensorial nature of $\hat{g^2}(\boldsymbol{x})$ we have restored the physical unit of the electric field in this equation. Here $\boldsymbol{\Psi}_\mu^\dagger$ is the hermitian conjugate of $\boldsymbol{\Psi}_\mu$ and the quantity $\boldsymbol{\Psi}_\mu^\dagger(\boldsymbol{x}) \cdot \hat{g^2}(\boldsymbol{x}) \cdot \boldsymbol{\Psi}_\mu(\boldsymbol{x})$ in the sum is a scalar. This quantity can also be written as $g_\mu^2(\boldsymbol{x})|\boldsymbol{\Psi}_\mu(\boldsymbol{x})|^2$, in which

$$g_\mu(\boldsymbol{x}) \equiv \boldsymbol{g}(\boldsymbol{x})^T \cdot \boldsymbol{\Psi}_\mu(\boldsymbol{x})/|\boldsymbol{\Psi}_\mu(\boldsymbol{x})| \tag{2.22}$$

is the projection of $\boldsymbol{g}(\boldsymbol{x})$ along the direction $\boldsymbol{\Psi}_\mu(\boldsymbol{x})$. $g_\mu(\boldsymbol{x})$ is not always positive, but since it is $g_\mu^2(\boldsymbol{x})$ that appear in the denominator its eigenvalues are positive and it will always suppress lasing. In the case that all $\boldsymbol{\Psi}_\mu(\boldsymbol{x})$ are linearly polarized in the same direction, e. g., $\boldsymbol{\Psi}_\mu(\boldsymbol{x}) = \Psi_\mu(\boldsymbol{x})\hat{\boldsymbol{z}}$, we recover Eq. (2.13) in a homogeneous medium with $g^2 = g_z^2$.

Finally, the vectorial generalization of the SALT I equation (2.15) is

$$\left[\nabla\times\nabla\times-\left(\epsilon_c(\boldsymbol{x})+\frac{\gamma_\perp}{(\omega^\mu-\omega_a)+i\gamma_\perp}\frac{D_0(\boldsymbol{x})}{1+\sum_\nu\frac{4\Gamma_\nu}{\hbar^2\gamma_\parallel\gamma_\perp}g_\nu^2(\boldsymbol{x})|\boldsymbol{\Psi}_\nu(\boldsymbol{x})|^2}\right)k^{\mu 2}\right]\Psi_\mu(\boldsymbol{x})=0, \tag{2.23}$$

and its solution algorithm in 3D is under investigation. The discussion above is the only place in this thesis that we consider the vectorial generalization of the SALT, and we will continue to discuss the properties and applications of the scalar SALT below.

2.3 Multi-level generalization

Before we describe the details of how to solve Eq. (2.19) we want to check whether Eq. (2.19) is applicable to a three-level or four-level laser. In Ref. [3] the author discusses the rate equation in two-level and multi-level systems and how they are related. Here we show that the equation for the population inversion in a four-level system can be put in the form of Eq. (2.3) in the steady state, which is derived for the two-level system. The treatment of the three-level MB equations is very similar and we will comment on the difference at the end of this section.

We label the four energy levels from 0 to 3, with level 0 being the ground level, and assume the lasing transition happens between the two middle levels (Fig. 2.1). The dynamics of the four levels are then captured by the following equations:

$$\dot\rho_{33} = \mathcal{P}(\rho_{00}-\rho_{33})-\gamma_{32}\rho_{33}, \tag{2.24}$$

$$\dot\rho_{22} = \gamma_{32}\rho_{33}-\Gamma_{21}\rho_{22}-\frac{1}{i\hbar}E((P^+)^*-P^+), \tag{2.25}$$

$$\dot\rho_{11} = \Gamma_{21}\rho_{22}-\gamma_{10}\rho_{11}+\frac{1}{i\hbar}E((P^+)^*-P^+), \tag{2.26}$$

$$\dot\rho_{00} = -\mathcal{P}(\rho_{00}-\rho_{33})+\gamma_{10}\rho_{11}. \tag{2.27}$$

ρ_{ii} is the ith diagonal element of the density matrix times the number of atoms per unit volume denoted by n. Γ_{ij} and γ_{ij} are the non-stimulated decay rate and the total decay rate from level i to level j. The electrons are pumped from level 0 to level 3 and the pump strength is given by $\mathcal{P}$ and proportional to the population difference between these two levels. In principle we need to add a stimulated emission term to Eqs. (2.24) and (2.27), but we dropped it since in almost all cases the induced polarization between level 0 and level 3 is weak. The decay processes between non-adjacent levels are also neglected.

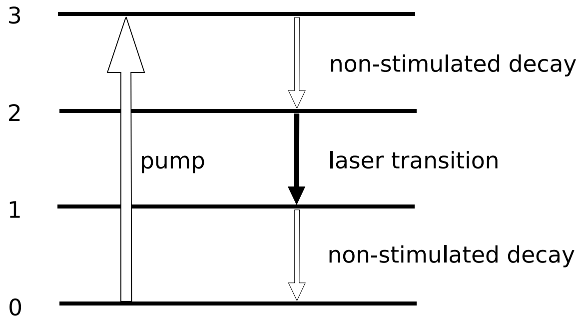

Figure 2.1: Schematic of a four-level laser where the electrons are pumped from the ground level to level 3 and the lasing transition happens between the two middle levels.

By solving Eqs. (2.24) and (2.27) in the steady state, we can express ρ_{00} and ρ_{33} in terms of ρ_{11} and $\mathcal{P}$. Combine the results with the conservation of the total number of atoms per unit volume, we see immediately that both ρ_{11} and ρ_{22} are functions of the inversion $D \equiv \rho_{22} - \rho_{11}$ and $\mathcal{P}$ only. For example,

$$\rho_{11} = \frac{n - D}{2 + \frac{\gamma_{10}}{\mathcal{P}} + 2\frac{\gamma_{10}}{\gamma_{32}}}, \tag{2.28}$$

and $\rho_{22} = D + \rho_{11}$. Next we subtract Eq. (2.25) by Eq. (2.26) and substitute ρ_{11} and ρ_{22} by the values given above. We find the resulting steady state equation

$$0 = \dot{D} = \gamma'_{\parallel}(D'_0 - D) - \frac{2}{i\hbar}E((P^+)^* - P^+) \tag{2.29}$$

has the form of Eq. (2.3) with the modified quantities

$$\gamma'_{\parallel} \equiv 2\Gamma_{21}\left(1 + \frac{S}{2 + \frac{\gamma_{10}}{\mathcal{P}} + 2\frac{\gamma_{10}}{\gamma_{32}}}\right) \tag{2.30}$$

and

$$D'_0 \equiv \frac{Sn\mathcal{P}}{\gamma_{10} + (S + 2 + 2\frac{\gamma_{10}}{\gamma_{32}})\mathcal{P}}. \tag{2.31}$$

Here S is defined as the ratio $\frac{\gamma_{10}-\Gamma_{21}}{\Gamma_{21}}$. To help creating the inversion between Level 2 and Level 1, Level 2 and 1 are chosen to be meta-stable and unstable, respectively. Therefore, the decay rate of Level 1 (γ_{10}) is larger than that of Level 2 (Γ_{21}), which means S is always positive. The expression of D_0' confirms that the parameter D_0, which is used in the two-level equation as the pump strength, does increase monotonically with the true pump strength $\mathcal{P}$. When $\mathcal{P}$ is small ($\mathcal{P} \ll \gamma_{10}$), $D_0' \approx Sn\mathcal{P}/\gamma_{10}$ increases linearly as a function of $\mathcal{P}$. The inversion starts to saturate as $\mathcal{P}$ becomes comparable to γ_{10} and reaches the fully saturated value $D_0' = Sn/(S + 2 + 2\gamma_{10}/\gamma_{32})$ when $\mathcal{P} \gg \gamma_{10}$. These values depend on the two ratios γ_{32}/γ_{10} and γ_{10}/Γ_{21}, and when they are large, i. e., $\gamma_{32} > \gamma_{10} > \Gamma_{21}$, a desirable inversion can be reached at a relatively small pump value.

One difference of Eqs. (2.3) and (2.29) lies in the value of the equilibrium value of D_0 in the absence of pump. In the former D_0 is essentially -1 (following the Boltzmann distribution) times the number of atoms per unit volume, but in the latter we note that D_0' is zero when $\mathcal{P}$ goes to zero (see Eq. (2.31)). This is consistent with the Boltzmann distribution because almost all atoms are in the ground state, and it is a good approximation to take $\rho_{22} = \rho_{11} = 0$. In ultra-low threshold lasers one may consider restoring the difference of ρ_{22} and ρ_{11} given by the Boltzmann distribution $\rho_{22}/\rho_{11} = \exp(-(E_2 - E_1)/k_B T)$.

The other difference of Eqs. (2.29) and (2.3) is that $\gamma_{\parallel}'$ is now a pump-dependent decay rate, which is approximated $2\Gamma_{21}$ at low pump powers and $(\Gamma_{21} + \gamma_{10})$ when the inversion saturates at high pump powers, assuming $\gamma_{10} \ll \gamma_{32}$. Notice the change $\gamma_{\parallel} \to \gamma_{\parallel}'$ only affects the natural unit of the electric field ($e_c \to e_c' \equiv \hbar\sqrt{\gamma_\perp \gamma_{\parallel}'}/(2g)$ which doesn't enter the self-consistent equation (2.15) explicitly. This means that the four-level MB equations can indeed be cast into the two-level form in the steady state. We can then solve them at any given pump strength $\mathcal{P}$ converted to the equilibrium value of the inversion D_0' using Eq. (2.31). The physical scale of the amplitudes of the lasing modes is restored by multiplying the results by e_c'.

In the three-level case if the lasing transition happens between the upper two levels (level 2 and level 1), one can imagine the system is pumped to a "virtual" fourth level slightly above level 2, and decays instantaneously onto the latter. Thus this three-level scheme is identical to the four-level one we just discussed with γ_{32} goes to ∞. Since γ_{32}

only appears in the fraction γ_{10}/γ_{32}, one can drop the fraction everywhere it appears and the behaviors of $\gamma'_{\|}$ and D'_0 as functions of $\mathcal{P}$ are essentially the same.

The other three-level scheme, where the lasing transition happens between the lower two levels (level 2 and level 1, with the latter being the ground level now), is not popular because a much higher pump power is needed to created the inversion between the first excited level and the ground level. Nevertheless, to demonstrate the versatility of the method we use here, we write down the map from the microscopic quantities in this case to those we use in the two-level case:

$$D'_0 \equiv \frac{\left(\frac{\gamma_{32}}{\Gamma_{21}} - 1\right) - \frac{\gamma_{32}}{\mathcal{P}}}{\left(\frac{\gamma_{32}}{\Gamma_{21}} + 2\right) + \frac{\gamma_{32}}{\mathcal{P}}} = -1 + \frac{\left(2\frac{\gamma_{32}}{\Gamma_{21}} + 1\right)\mathcal{P}}{\gamma_{32} + \left(\frac{\gamma_{32}}{\Gamma_{21}} + 2\right)\mathcal{P}}, \quad \gamma'_{\|} \equiv 2\Gamma_{21}\frac{\left(\frac{\gamma_{32}}{\Gamma_{21}} + 2\right) + \frac{\gamma_{32}}{\mathcal{P}}}{3 + 2\frac{\gamma_{32}}{\mathcal{P}}}. \quad (2.32)$$

To check whether the quantities above are reasonable, we first note that D'_0 and $\gamma'_{\|}$ become -1 and Γ_{21} as they should when $\mathcal{P}$ approaches zero. A positive inversion between level 2 and level 1 can be achieved only if $\gamma_{32} > \Gamma_{21}$, and the minimal pump strength required $\mathcal{P} = \gamma_{32}\Gamma_{21}/(\gamma_{32} - \Gamma_{21})$ is much larger than that in the four-level case and the other three-level cases. At a high pump power ($\mathcal{P} \gg \gamma_{32}$) $\gamma'_{\|} \approx 2(2\Gamma_{21} + \gamma_{32})/3$ is greater than $2\Gamma_{21}$, which is the same as in the other two cases discussed above.

The above procedure can be repeated for more complicated gain level structures as long as there is only one lasing transition. The resulting matter equations, though complicated, still have a structure similar to the Bloch equations, which then leads to a rescaled version of the SALT equations (2.15 and 2.19). Therefore, we can apply the SALT presented in this thesis to these lasers and find their lasing properties.

2.4 Constant-flux states

Having shown that multi-level MB equations in the the steady state can be solve for the lasing modes similarly to the two-level case, we will now continue our discussion of solving the self-consistent equations (2.15) and (2.19). Despite the fact that both equations are nonlinear, there is a natural basis set, consisting of the constant-flux states[1], in which to

[1]We found recently that the CF states were introduced before in an isotropic medium to explain the dispersion formula for nuclear reactions[75].

expand the functions $\Psi_\mu(x)$ [66, 52]. This basis is determined by the nature of a laser: there should be only outgoing waves of real frequencies far from the cavity boundary all the way to infinity. Notice the subtle difference between the above requirement and the outgoing boundary condition imposed at the cavity boundary: They differ if the cavity is concave or made up of disjointed structures. For mathematical convenience we introduce the last scattering surface (LSS) which is convex and encloses all the interesting structures of a laser cavity. The requirement of convexity is to guarantee that the scattered light does not re-enter the LSS at some other place and we can impose the outgoing boundary condition at the LSS. The choice of the LSS is not unique; any convex shape can be a candidate as long as it encloses the laser cavity. Outside the LSS the index of refraction $\epsilon_>$ is assumed to be a constant, representing either a dielectric structure whose size is much larger than the cavity or simply air. The other important aspect of the boundary condition is that we require the outgoing waves have real frequencies. This guarantees that the photon flux is conserved outside the cavity and the amplitude of a lasing mode does't increase exponentially when $\boldsymbol{x} \to \infty$.

For pedagogical purpose we choose an isotropic LSS with radius R, which consists two symmetrically placed points about the origin in 1D, a circle in 2D and a sphere in 3D. Two CF states, $\varphi_p(\boldsymbol{x},\omega)$ and $\varphi_q(\boldsymbol{x},\omega)$, are defined as the solutions of the following Helmholtz equations inside the LSS:

$$\left[\nabla^2 + \epsilon_c(\boldsymbol{x})k_p^2\right]\varphi_p(\boldsymbol{x},\omega) = 0, \quad (r < R), \tag{2.33}$$

$$\left[\nabla^2 + \epsilon_c(\boldsymbol{x})k_q^2\right]\varphi_q(\boldsymbol{x},\omega) = 0. \quad (r < R). \tag{2.34}$$

φ_p and φ_q are ω-dependent where ω is the real-valued lasing frequency outside the LSS:

$$\left[\nabla^2 + \epsilon_> k^2\right]\varphi_p(\boldsymbol{x},\omega) = 0, \quad (r > R), \tag{2.35}$$

$$\left[\nabla^2 + \epsilon_> k^2\right]\varphi_q(\boldsymbol{x},\omega) = 0. \quad (r > R). \tag{2.36}$$

The general form of outgoing waves satisfying the above Helmholtz equations outside the LSS is familiar. In 1D along the positive x-axis they are plane waves traveling to the right, and in 2D and 3D their radial behaviors are given by the superpositions of the outgoing

Hankel functions and spherical Hankel functions, respectively. The mathematical descriptions of the outgoing boundary condition in various geometries are given in Chapter 3. For each given ω there are a countably infinite set of CF states. Their eigenfrequencies $\{k_m\}$ can be shown to always have a negative imaginary part [52], which means the CF states are amplified within the LSS. We mentioned in the introduction that the quasi-bound (QB) modes have been used extensively in the study of laser cavities. In fact they are defined similarly to the CF states. In Section 2.5 and Chapter 3 we will compare them in detail, and here we just mention that the QB modes don't conserve the energy flux outside the cavity and they are not orthogonal by standard definitions.

By operating $\int_{r<R} d\boldsymbol{x}\varphi_p(\boldsymbol{x},\omega)$ and $\int_{r<R} d\boldsymbol{x}\varphi_q(\boldsymbol{x},\omega)$ on Eqs. (2.33) and (2.35) from the left and subtracting the resulting equations we derive

$$\begin{aligned} & (k_p^2 - k_q^2) \int_{r<R} d\boldsymbol{x}\, \epsilon_c(\boldsymbol{x})\, \varphi_p(\boldsymbol{x},\omega)\, \varphi_q(\boldsymbol{x},\omega) \\ = & \int_{r<R} d\boldsymbol{x}[\varphi_q(\boldsymbol{x},\omega)\nabla^2\varphi_p(\boldsymbol{x},\omega) - \varphi_p(\boldsymbol{x},\omega)\nabla^2\varphi_q(\boldsymbol{x},\omega)] \\ = & \int_{r=R} d\boldsymbol{x}[\varphi_q(\boldsymbol{x},\omega)\frac{\partial\varphi_p(\boldsymbol{x},\omega)}{\partial r} - \varphi_p(\boldsymbol{x},\omega)\frac{\partial\varphi_q(\boldsymbol{x},\omega)}{\partial r}]. \end{aligned} \tag{2.37}$$

In the last step we used the Green's theorem and $\frac{\partial}{\partial r}$ is the radial derivative. The latter appears as a consequence of the isotropic LSS we chose, and it doesn't imply that the flux of the CF states has only radial component.

By repeating the same procedure for Eqs. (2.35) and (2.36) we have

$$\int_{r=R}[\varphi_q\frac{\partial\varphi_p}{\partial r} - \varphi_p\frac{\partial\varphi_q}{\partial r}] = \int_{r=\infty}[\varphi_q\frac{\partial\varphi_p}{\partial r} - \varphi_p\frac{\partial\varphi_q}{\partial r}]. \tag{2.38}$$

If the right hand side of Eq. (2.38) vanishes for all $k_p \neq k_q$, we derive from Eqs. (2.37) and (2.38) the orthogonality relation for the CF basis

$$\int_{r<R} d\boldsymbol{x}\, \epsilon_c(\boldsymbol{x})\, \varphi_q(\boldsymbol{x},\omega)\, \varphi_p(\boldsymbol{x},\omega) \equiv \langle\varphi_p,\varphi_q\rangle = \delta_{pq}. \tag{2.39}$$

This equation can be interpreted in a different way, as will be discussed later in this section.

A sufficient condition for the right hand side of Eq. (2.38) $(p \neq q)$ to vanish is that the non-vanishing terms in $\frac{\partial \varphi_p}{\partial r}$ become $f(k)\varphi_p$ at infinity for all p's. In the one-dimensional case $\varphi_p(x,\omega)$ is proportional to $e^{\pm i\sqrt{\epsilon_>}kx}$ outside the LSS for positive/negative x, which gives $f(k) = \pm i\sqrt{\epsilon_>}k$ (we remind the reader that we have taken $c = 1$). Therefore, the orthogonality relation (2.39) of the CF states holds in 1D. In the two-dimensional case where $\epsilon_c(\boldsymbol{x}) = \epsilon_<$ is a constant inside the LSS, the label p is the combination of the angular momentum number m and the radial quantum number n, and outside the LSS

$$\varphi_{(m,\,n)}(\boldsymbol{x},\omega) = \mathrm{H}_m^+(\sqrt{\epsilon_>}kr)e^{im\varphi} \to \sqrt{\frac{\pi}{2kr}}e^{i(\sqrt{\epsilon_>}kr - m\frac{\pi}{2} - \frac{\pi}{4} + m\varphi)} \tag{2.40}$$

at $r = \infty$ (H_m^+ is the outgoing Hankel function). $\frac{\partial \varphi_{(m,n)}}{\partial r}$ have two terms, and the one due to the radial derivative of $r^{-\frac{1}{2}}$ decays faster than r^{-1} and has no contribution to the surface integral at $r = \infty$. The other term gives $f(k) = i\sqrt{\epsilon_>}k$ as in the one-dimensional case and the integrand in Eq. (2.38) vanishes uniformly. Now if $\epsilon_c(\boldsymbol{x})$ is not a constant, the CF state $\varphi_q(\boldsymbol{x},\omega)$ can be expanded by $\{\varphi_{(m,\,n)}(\boldsymbol{x},\omega)\}$ in the uniform index case, and $f(k)$ is again ink since the expansion coefficients have no $\boldsymbol{x}$-dependence. Thus we have shown that CF states in 2D are orthogonal in the sense of Eq. (2.39). In the three-dimensional case the discussion is very similar using the asymptotic behavior of the outgoing spherical Hankel functions at infinity, and we find again $f(k) = i\sqrt{\epsilon_>}k$ and the orthogonality (2.39) still holds.

If the LSS is chosen to be a convex surface which is not isotropic, Eqs. (2.37) and (2.38) still hold with $\frac{\partial}{\partial r}|_{\boldsymbol{x}\in LSS}$ replaced by the normal derivative $\frac{\partial}{\partial n}|_{\boldsymbol{x}\in LSS}$. Since the surface integral on the *r.h.s.* of Eq. (2.38) vanishes due to the outgoing boundary condition at infinity, we have shown that the orthogonality (2.39) is independent of the choice of the LSS. In some cases one may find it more convenient to choose the cavity boundary as the LSS if it is convex.

When the CF frequencies are degenerate, sometimes one needs to re-construct the degenerate subspace by linear transformations to make sure the normalization factor $\langle\varphi_p,\varphi_p\rangle$ doesn't vanish. For example, the two CF states with $p = (m,n)$ and $q = (-m,n)$ $(m > 0)$

$$\varphi_p = \mathrm{J}_m(\sqrt{\epsilon_<}\,k_{(|m|,\,n)}r)e^{im\varphi}, \quad \varphi_q = \mathrm{J}_m(\sqrt{\epsilon_<}\,k_{(|m|,\,n)}r)e^{-im\varphi} \tag{2.41}$$

in a two-dimensional micro-disk cavity share the same complex frequency $k_{(|m|,n)}$, and $\langle\varphi_p,\varphi_p\rangle = \langle\varphi_q,\varphi_q\rangle = 0$. But since $\langle\varphi_p,\varphi_q\rangle \neq 0$, one can define

$$\begin{cases} \varphi_a = \frac{\varphi_p+\varphi_q}{2} = \mathrm{J}_m(\sqrt{\epsilon_<}k_{(|m|,n)}r)\cos m\varphi, \\ \varphi_b = \frac{\varphi_p-\varphi_q}{2i} = \mathrm{J}_m(\sqrt{\epsilon_<}k_{(|m|,n)}r)\sin m\varphi \end{cases} \tag{2.42}$$

as the basis functions in the degenerate subspace and the bi-orthogonality is restored with proper normalization.

The orthogonality and the inner product defined in Eq. (2.39) lead to some interesting consequences. First we notice that the orthogonality is not the normal hermitian orthogonality as no complex conjugate is invoked in the inner product; the normal definition of the inner product in a complex function space satisfies $\langle\varphi_p,\varphi_q\rangle = \langle\varphi_q,\varphi_p\rangle^*$, but here we have $\langle\varphi_p,\varphi_q\rangle = \langle\varphi_q,\varphi_p\rangle$. Therefore, the "length" of an arbitrary vector $\Psi(\boldsymbol{x}) = \sum_p a_p\,\varphi_p(\boldsymbol{x},\omega)$ in the CF basis is the square root of $\langle\Psi(\boldsymbol{x}),\Psi(\boldsymbol{x})\rangle = \sum_p(a_p)^2$. Although this quantity is complex in general, it is conserved in basis transformations. But as a consequence we don't have a unit vector in the normal sense: a_p can have a modulus larger than unity even though $\sum_p(a_p)^2 = 1$.

An alternative interpretation of the orthogonality relation

An alternative interpretation of the orthogonality relation (2.39) requires the introduction of a set of dual functions $\{\bar{\varphi}_m(\boldsymbol{x},\omega)\}$. They satisfy the same equations as the CF states (Eqs. (2.33) and (2.35)) but with the incoming boundary condition and with $\epsilon_c(\boldsymbol{x})$ and $\epsilon_>$ replaced by their complex conjugates:

$$\left[\nabla^2 + \epsilon_c(\boldsymbol{x})^*\bar{k}_m^2\right]\bar{\varphi}_m(\boldsymbol{x},\omega) = 0, \quad (r < R), \tag{2.43}$$

$$\left[\nabla^2 + \epsilon_>^* k^2\right]\bar{\varphi}_m(\boldsymbol{x},\omega) = 0, \quad (r > R). \tag{2.44}$$

R here is the radius of the isotropic LSS as before. $\{\bar{\varphi}_m(\boldsymbol{x},\omega)\}$ can be treated as the time-reverse of the CF states, and the equations and the boundary condition they satisfy are the hermitian conjugates of those satisfied by the CF states. One can see that $\bar{k}_m^2 = (k_m^2)^*$ and $\bar{\varphi}_m(\boldsymbol{x},\omega) = (\varphi_m(\boldsymbol{x},\omega))^*$ by taking the complex conjugates of the equations above and comparing them with Eqs. (2.33) and (2.35), and it is easy to check that the flux in $\bar{\varphi}_m(\boldsymbol{x},\omega)$ outside the LSS is incoming. Therefore, the orthogonality relation (2.39) can be rewritten as

$$\int_{r<R} d\boldsymbol{x}\, \epsilon_c(\boldsymbol{x})\ (\bar{\varphi}_m(\boldsymbol{x},\omega))^*\ \varphi_n(\boldsymbol{x},\omega) = \delta_{mn}\,. \tag{2.45}$$

$\epsilon_c(\boldsymbol{x})$ can remove from the integral if it is a constant, which leads to a different normalization of the CF states and their dual functions. The above bi-orthogonality is then defined using the standard definition of an inner product.

With this definition of the dual functions $\bar{\varphi}_m(\boldsymbol{x},\omega)$ are trivially related to $\varphi_m(\boldsymbol{x},\omega)$, but notice that Eq. (2.33) has the form of a generalized eigenvalue problem when $\epsilon_c(\boldsymbol{x})$ varies in space. In this case it may be useful to divide Eqs. (2.33) and (2.35) by $\epsilon_c(\boldsymbol{x})$ and $\epsilon_>$ to obtain a standard eigenvalue problem for the operator $\epsilon_c(\boldsymbol{x})^{-1}\nabla^2$. The CF states and their eigenfrequencies *do not* change but the dual functions are non-trivially changed. The equations defining the time-reversed problem are the hermitian conjugates of these reformulated equations, as in the case discussed above:

$$\begin{aligned} \left[\nabla^2(\epsilon_c(\boldsymbol{x})^{*-1}\bullet) + \bar{k}_m^2\right]\bar{\varphi}_m(\boldsymbol{x},\omega) &= 0, \quad (r<R), && (2.46)\\ \left[\nabla^2(\epsilon_>^{*\,-1}\bullet) + \bar{k}^2\right]\bar{\varphi}_m(\boldsymbol{x},\omega) &= 0, \quad (r>R). && (2.47) \end{aligned}$$

Notice the order of the two operators ϵ^{*-1} and ∇^2 has changed from that in the reformulated equations the CF states satisfy, and the $\bullet$ indicates that ∇^2 acts on the product of ϵ^{*-1} and $\bar{\varphi}_m(\boldsymbol{x},\omega)$. Evidently, $\bar{k}_m^2$ still equals $(k_m^2)^*$ but $\bar{\varphi}_m(\boldsymbol{x},\omega)$ is now $(\epsilon_c(\boldsymbol{x})\varphi_m(\boldsymbol{x},\omega))^*$ inside the LSS. Therefore, the orthogonality relation (2.39) can be interpreted as the bi-orthogonality relation between the CF states and their dual functions $\{\bar{\varphi}_m(\boldsymbol{x},\omega)\}$, with the standard definition of an inner product

$$\int_{r<R} d\boldsymbol{x}\ (\bar{\varphi}_m(\boldsymbol{x},\omega))^*\ \varphi_n(\boldsymbol{x},\omega) = \delta_{mn}\,. \tag{2.48}$$

$\{k_m, \bar{k}_m^*\}$ are known as the right and left eigenvalues of the operator $\epsilon_c(\boldsymbol{x})^{-1}\nabla^2$ inside the LSS, and $\{\varphi_m(\boldsymbol{x},\omega), \bar{\varphi}_m^\dagger(\boldsymbol{x},\omega)\}$ are the corresponding right and left eigenvectors. These conventions were used in reference [65] as the numerical CF solver used was based on the form of the CF equation with the operator $\epsilon^{-1}\nabla^2 + k_m^2$. We use the form with $\nabla^2 + \epsilon_c k_m^2$ primarily throughout this thesis. It is important to note that with these conventions the SALT equation (2.19) appears differently from that in Ref. [65]. The integral kernel there contains $\epsilon_c(\boldsymbol{x})^{-1}$ and the Green's function is defined with respect to $\epsilon(\boldsymbol{x})_c^{-1}\nabla^2$. Exactly the same equation for the lasing modes (2.50) is still obtained, as must be the case.

Expansion of the SALT equations in the CF basis

Having shown that the orthogonality of the CF states holds within the LSS, we expand the SALT I equation (2.15) in the CF basis using $\Psi_\mu(\boldsymbol{x},\omega^\mu) = \sum_p a_p^\mu\, \varphi_p(\boldsymbol{x},\omega^\mu)$:

$$\sum_p a_p^\mu \left[(k^{\mu 2} - k_p^2)\epsilon_c(\boldsymbol{x}) + \frac{\gamma_\perp}{(\omega^\mu - \omega_a) + i\gamma_\perp} \frac{D_0(\boldsymbol{x})}{1 + \sum_\nu \Gamma_\nu |\Psi_\nu(\boldsymbol{x})|^2} k^{\mu 2}\right] \varphi_p(\boldsymbol{x},\omega^\mu) = 0. \tag{2.49}$$

We will refer to the region inside the LSS as Domain $\mathcal{D}$ in the following discussion unless otherwise stated. By operating $\int_{r\in\mathcal{D}} d\boldsymbol{x}\varphi_m(\boldsymbol{x},\omega^\mu)$ on the equation from the left and use the orthogonality (2.39), we derive a set of integral equations for $\{a_m^\mu\}$:

$$a_m^\mu = -\frac{\gamma_\perp}{(\omega^\mu - \omega_a) + i\gamma_\perp} \frac{k^{\mu 2}}{k^{\mu 2} - k_m^2} \int_{\mathcal{D}} d\boldsymbol{x}' \frac{D_0(1 + d_0(\boldsymbol{x}'))\varphi_m(\boldsymbol{x}',\omega^\mu) \sum_p a_p^\mu\, \varphi_p(\boldsymbol{x}',\omega^\mu)}{1 + \sum_\nu \Gamma_\nu \left|\sum_p a_p^\nu\, \varphi_p(\boldsymbol{x}',\omega^\nu)\right|^2}. \tag{2.50}$$

$D_0(\boldsymbol{x})$ is rewritten as an overall pump strength D_0 times the spatial variation $(1 + d_0(\boldsymbol{x}))$. In general Eq. (2.50) gives a nonlinear map for the vectors of coefficients in the CF basis and the actual nonzero lasing solution is a fixed point of this map. Above the lasing threshold for each mode, D_{th}^μ, we find that the nonzero solutions are stable fixed points and trial vectors flow to them under iteration of the map while the trivial zero solutions, which below D_{th}^μ are stable, become unstable. Note that the map is proportional to $[k^{\mu 2} - k_m^2]^{-1}$, favoring CF states with a complex frequency close to the real lasing frequency.

To show that the two SALT equations (2.15) and (2.19) are indeed equivalent, we first introduce the spectral representation of the Green's function defined by Eq. (2.17) in the CF basis:

$$G(\boldsymbol{x},\boldsymbol{x}';\omega) = \sum_p \frac{\varphi_p(\boldsymbol{x},\omega)\varphi_p(\boldsymbol{x}',\omega)}{k^2 - k_p^2(\omega)}. \tag{2.51}$$

It is straightforward to check that the above expression satisfies Eq. (2.17). This expression indicates that the Green's function only has poles in the lower half of the complex plane for $\mathrm{Re}[k] > 0$ since the CF eigenfrequencies k_p all have a positive real part and a negative imaginary part. This justifies the procedure of equating the real poles when we derive Eq. (2.19). By inserting the expansions above into the SALT II equation (2.19) with ω evaluated at ω^μ, multiplying both sides of the resulting equation by $\epsilon_c(\boldsymbol{x}')\varphi_m(\boldsymbol{x}', \omega^\mu)$ and integrating over $\mathcal{D}$, we end up with exactly the same equation (2.50).

Gain region CF states

In the case that the LSS doesn't coincide with the boundary of the gain region(s), the CF states defined by Eqs. (2.33) and (2.35) still form a complete and orthogonal basis even though they amplify outside the gain region(s) (but not outside the LSS). In some scenarios this causes us some inconvenience by requiring a rather large CF basis. One way to overcome this problem is to introduce the gain region CF states (GRCF), which have a complex wave vector only within the gain region and a real wave vector everywhere else:

$$\left[\nabla^2 + \epsilon_i k_p^2\right] \varphi_p(\boldsymbol{x}, \omega) = 0, \quad (\boldsymbol{x} \in \cup_{i=1}^{N} \mathcal{G}_i)\,, \tag{2.52}$$

$$\left[\nabla^2 + \epsilon_< k^2\right] \varphi_p(\boldsymbol{x}, \omega) = 0, \quad (\boldsymbol{x} \in \mathcal{D} \cap (\cup_{i=1}^{N} \overline{\mathcal{G}_i}))\,, \tag{2.53}$$

$$\left[\nabla^2 + \epsilon_> k^2\right] \varphi_p(\boldsymbol{x}, \omega) = 0, \quad (\boldsymbol{x} \in \overline{\mathcal{D}})\,. \tag{2.54}$$

Here we assume that there are N gain regions $\mathcal{G}_i$'s of index $n_i = \sqrt{\epsilon_i}$ inside the LSS for generality (see Fig. 2.2) and $\overline{\mathcal{G}_i}$ denotes the complement of $\mathcal{G}_i$. In the rest of the Domain $\mathcal{D}$ the index is assumed to be a constant $\epsilon_<$, and the outgoing boundary condition as usual is imposed on the LSS. The GRCF states can be shown to be orthogonal *within* the gain region in a similar manner to how we showed the orthogonality of the original CF states (2.39):

$$\int_{\cup_{i=1}^{N} \mathcal{G}_i} \epsilon_c(\boldsymbol{x})\, \varphi_\mu(\boldsymbol{x}, \omega)\, \varphi_\nu(\boldsymbol{x}, \omega) = \delta_{\mu\nu}\,. \tag{2.55}$$

In Appendix B we will derive the above orthogonality in detail using the example of a one-dimensional laser cavity with alternate layers of gain and gain-free regions.

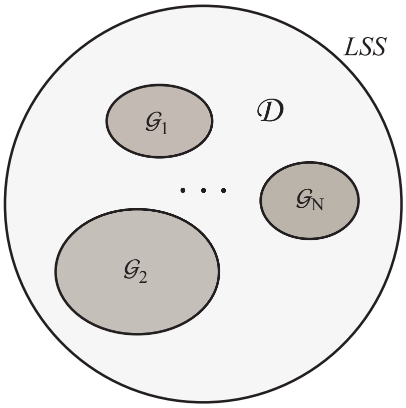

Figure 2.2: Schematic of a laser containing multiple gain regions inside the last scattering surface.

The Green's function in this case is defined only inside the gain regions

$$\left[\nabla^2 + \epsilon_i k^2\right] G(\boldsymbol{x}, \boldsymbol{x}'|\omega) = \delta(\boldsymbol{x} - \boldsymbol{x}') \quad (x, x' \in \cup_{i=1}^{N} \mathcal{G}_i), \tag{2.56}$$

and its spectral representation has the same form in Eq. (2.51). By expanding the lasing modes in the GRCF basis and repeating the derivation leading to Eq. (2.50), we recover the self-consistent equation Eq. (2.50)

$$a_m^\mu = -\frac{\gamma_\perp}{(\omega^\mu - \omega_a) + i\gamma_\perp} \frac{k^{\mu 2}}{k^{\mu 2} - k_m^2} \int_{\cup_{i=1}^{N}\mathcal{G}_i} d\boldsymbol{x}' \frac{D_0(1 + d_0(\boldsymbol{x}'))\varphi_m(\boldsymbol{x}', \omega^\mu) \sum_p a_p^\mu \varphi_p(\boldsymbol{x}', \omega^\mu)}{1 + \sum_\nu \Gamma_\nu \left|\sum_p a_p^\nu \varphi_p(\boldsymbol{x}', \omega^\nu)\right|^2} \tag{2.57}$$

with the only difference being that the integral is now over the gain regions. We will discuss how we can benefit from the GRCF basis in Section 4.1 and 4.3.

2.5 Threshold lasing modes

As mentioned in the introduction the quasi-bound (QB) modes are used extensively in the standard semiclassical laser treatment. Because the outgoing boundary condition they satisfy is incompatible with current conservation, the associated eigenvectors of the S-matrix have complex wavevector, $\tilde{k}_m$. These complex frequencies are the poles of the S-matrix and their imaginary parts must always be negative to satisfy causality conditions. In this section we assume that $\epsilon_c(\boldsymbol{x})$ is real for simplicity. From this point of view, QB modes are defined similar to CF states with the outgoing boundary condition and the equations they satisfy (Eqs. (2.33) and (2.35)). However, they differ because the wavevector of a QB mode is complex both inside and outside the cavity, while the wavevector of a CF state is only complex in the cavity. There are normally a countably infinite set of such QB modes. Due to their complex wavevector, asymptotically the QB modes vary as $r^{-(d-1)/2}\exp(-\mathrm{Im}[\tilde{k}_m]r)$ and diverge at infinity, so they are not normalizable solutions of the time-independent wave equation. Therefore we see that QB modes cannot represent the lasing modes of the cavity, even at threshold, as the lasing modes have real frequency and wavevector outside the cavity with conserved photon flux.

For an active cavity however, the effective index $\epsilon(\boldsymbol{x}) = \epsilon_c(\boldsymbol{x}) + \epsilon_g(\boldsymbol{x})$ in Eq. (2.15) becomes complex and its imaginary/amplifying part increases continuously when we turn on the pump. The S-matrix is no longer unitary, and its poles move continuously "upward" towards the real axis until one of them crosses the axis at a particular pump value, $D_{th}^{(1)}$ (see Fig. 2.3), which gives the first threshold. Suppose $\epsilon_c(\boldsymbol{x})$ is a constant and we pump the cavity uniformly, the first lasing mode is then a CF state with

$$k_m(\omega = \omega^{(1)}) = \sqrt{1 + \frac{D_{th}^{(1)}}{\epsilon_c} \frac{\gamma_\perp}{(\omega^{(1)} - \omega_a) + i\gamma_\perp}}\, k^{(1)}. \tag{2.58}$$

Which pole reaches the real axis first depends not only on the Q-value of the passive cavity resonance before gain is added, but also on the parameters of $\epsilon_g(\boldsymbol{x})$ which include the atomic transition frequency, the gain linewidth $\gamma_\perp$ and the spatial pump profile $D_0(\boldsymbol{x})$. If we keep increasing D_0, $\Psi_1(\boldsymbol{x})$ in the denominator of $\epsilon_g(\boldsymbol{x})$ is no longer zero, which affects the behavior of the other poles. The S-matrix is now non-linear. Above threshold the pole of the first lasing mode can only move along the real axis since the corresponding frequency is the lasing frequency.

If we neglect the modal interaction and gain saturation, Eq. (2.15) reduces to a linear equation for the amplitude of each lasing mode

$$\left[\nabla^2 + \left(\epsilon_c(\boldsymbol{x}) + \frac{D_0(\boldsymbol{x})\gamma_\perp}{(\omega^\mu - \omega_a) + i\gamma_\perp}\right) k^{\mu 2}\right] \Psi_\mu(\boldsymbol{x}) = 0. \tag{2.59}$$

This is similar to the linear gain model in which the effect of the gain is treated as adding an imaginary part to the index of refraction inside the gain region. In this model the real part of the index is normally considered to be unchanged in the presence of gain, but Eq. (2.59) tells us that this assumption is not true in general. If the detuning $(\omega^\mu - \omega_a) \ll \gamma_\perp$, the effective index can be written as

$$n(x) = \sqrt{\epsilon_c(x) + \epsilon_g(x)} \approx \sqrt{\epsilon_c(x)}\left(1 + \frac{\delta(x)^2}{8} + o(\delta(x)^2)\right) - i\frac{\sqrt{\epsilon_c(x)}}{2}\left(\delta(x) + o(\delta(x))\right) \tag{2.60}$$

where $\delta(x) \equiv D_0(x)/\epsilon_c(x)$. The first order correction to the cavity index $n_c(\boldsymbol{x}) = \sqrt{\epsilon_c(\boldsymbol{x})}$ only affects its imaginary part (we have assumed $\epsilon_c(x)$ is real); hence the linear gain model can be justified if the $D_0(x) \ll \epsilon_c(x)$ as all the higher order corrections, including those to the real part of $n(\boldsymbol{x})$, can be dropped. In Chapter 8 we will use the linear gain model to study the emergence of new modes in a one-dimensional uniform edge-emitting laser cavity with a spatial inhomogeneous gain medium.

We will refer to the solution $\Psi_\mu(\boldsymbol{x})$ of Eq. (2.59) as the threshold lasing modes (TLMs). Since we dropped the modal interaction and gain saturation, the behavior of the poles of the S-matrix corresponding to the higher order lasing modes are similar to that of the first mode when we turn on the pump. The place where each pole crosses the real axis is the real lasing frequency ω^μ for that particular TLM (see Fig. 2.3), and the corresponding eigenvector of the S-matrix gives the spatial profile $\Psi_\mu(\boldsymbol{x})$. Note that the poles do not move vertically to reach the real axis but always have some shift of the lasing frequency from the passive cavity frequency, mainly due to line-pulling effect [55] towards the atomic transition frequency. As the Q-value of the cavity increases, the distance the poles need to move to reach the real axis decreases so that the frequency shift from the corresponding $\mathrm{Re}[\tilde{\omega}_m]$ can become very small and the conventional picture becomes more correct. From this argument one sees that the TLMs are in one to one correspondence with the QB modes and thus are countably infinite. But here we emphasize that for any cavity only the lowest threshold TLM describes an observable lasing mode for fixed pumping conditions, the *first lasing mode* at threshold.

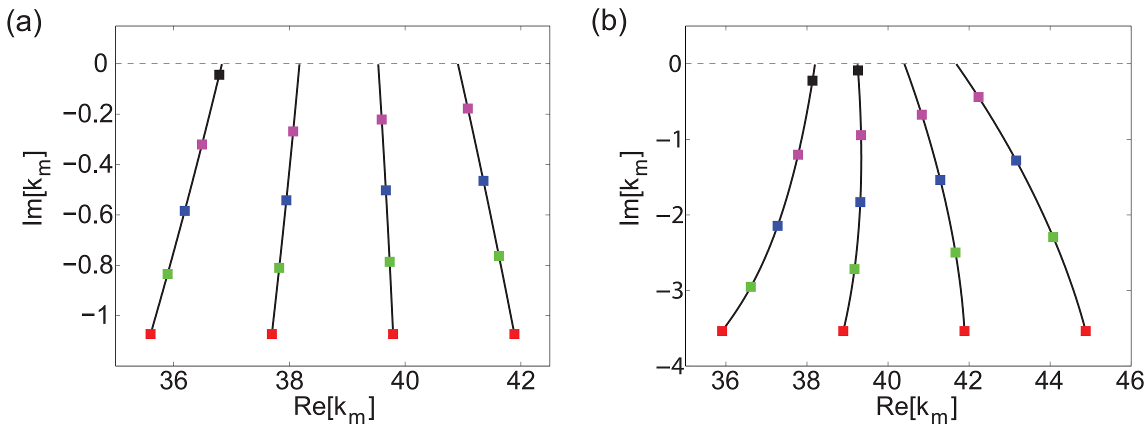

Figure 2.3: Shift of the poles of the S-matrix in the complex plane onto the real axis to form threshold lasing modes when the imaginary part of the dielectric function $\epsilon \equiv \epsilon_c + \epsilon_g$ varies for a simple one-dimensional edge-emitting laser of length L. The cavity index is $n_c = 1.5$ in (a) and 1.05 in (b). The squares of different colors represent $\mathrm{Im}[\epsilon_g] = 0, -0.032, -0.064, -0.096, -0.128$ in (a) and $\mathrm{Im}[\epsilon_g] = 0, -0.04, -0.08, -0.12, -0.16$ in (b). Note the increase in the frequency shift in the complex plane for the leakier cavity. The center of the gain curve is at $kL = 39$ which determines the visible line-pulling effect.

If the uniform index cavity is pumped uniformly, not only the first lasing mode but all the TLMs are single CF states, associated with different real frequencies ω^μ, (again neglecting non-linear interactions). As we will discuss in Chapter 4, this is true in general if $D_0(\boldsymbol{x})$ is proportional to $\epsilon_c(\boldsymbol{x})$. We find that the TLMs are still nearly diagonal in the CF basis even if this criterion is not met. Thus it is useful to study the CF states more closely as we do in the next chapter.

Chapter 3

CF states in various geometries

We introduced the concept of the constant-flux states in Section. 2.4. Our algorithm for solving the nonlinear SALT equations (2.15) and (2.19) relies on the CF basis; hence calculating these states in many geometries is central to the theory. In this chapter we will discuss various aspects of the CF states in different geometries.

3.1 Homogeneous one-dimensional edge-emitting laser cavities

We first discuss the properties of the CF states in a one-dimensional edge-emitting laser cavity of index n_1 with a uniform gain medium showing in Fig. 3.1. The left side of the cavity ($x = 0$) is terminated by a perfect mirror, and the right side ($x = a$) is an interface with a medium of index n_2 which partially reflects the light. Here we don't assume n_1 is real, i. e., the cavity can be absorbing in the absence of gain. The CF states of such a laser cavity are then given by

$$\begin{cases} (\nabla^2 + n_1^2\, k_m^2)\, \varphi_m(x,\omega) = 0, & 0 < x \leq a, \\ (\nabla^2 + \; n_2^2\, k^2\,)\, \varphi_m(x,\omega) = 0, & x > a. \end{cases} \tag{3.1}$$

The last scattering surface in this case is the right side of the cavity. The CF boundary condition requires there is only an out-going wave outside the cavity ($x > a$), which

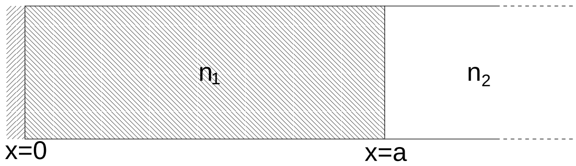

Figure 3.1: Schematic of a one-dimensional edge-emitting laser cavity of index n_1 and length a in a medium of index n_2.

translates into

$$\left.\frac{\partial\varphi_m}{\partial x}\right|_{x=a} = i\, n_2 k\, \varphi_m\, |_{x=a}\ . \tag{3.2}$$

This defines a countably infinite set of CF states which depend on the external real frequency k, and the complex CF frequencies are determined by

$$\tan(n_1 k_m a) = -i\frac{n_1 k_m}{n_2 k}. \tag{3.3}$$

The orthogonality of the CF states

$$\varphi_m(x,\omega) = \begin{cases} A_m \sin(n_1 k_m x), & 0 < x, \leq a \\ e^{in_2kx}, & x > a \end{cases} \tag{3.4}$$

can then be checked explicitly

$$\begin{aligned}
& \int_{cavity} dx\, \epsilon_c(x)\varphi_m(x,\omega)\varphi_{m'}(x,\omega) \\
= \;& n_1^2 \int_0^a dx\, \sin(n_1 k_m x)\sin(n_1 k_{m'} x) \\
= \;& \frac{an_1^2}{2}\left[\frac{\sin(n_1(k_m - k_{m'})a)}{n_1(k_m - k_{m'})a} - \frac{\sin(n_1(k_m + k_{m'})a)}{n_1(k_m + k_{m'})a}\right] \\
= \;& \frac{an_1^2}{2}\cos^2(n_1 k_m a)\cos^2(n_1 k_{m'} a) \times \left[\frac{\tan(n_1 k_m a) - \tan(n_1 k_{m'} a)}{n_1 a(k_m - k_{m'})} - \frac{\tan(n_1 k_m a) + \tan(n_1 k_{m'} a)}{n_1 a(k_m + k_{m'})}\right] \\
= \;& \frac{an_1^2}{2}\left[1 - \frac{\sin(2n_1 k_m a)}{2n_1 k_m a}\right]\delta_{mm'}.
\end{aligned} \tag{3.5}$$

In the last step we used the eigenvalue relation for complex CF frequencies given by Eq. (3.3), finding that the two terms in the brackets cancel each other if $m \neq m'$.

In Section 2.5 we mentioned that QB modes in a passive cavity are defined similarly to CF states; they satisfy the same Helmholtz equations and an outgoing boundary condition. In the one-dimensional case discussed here the QB modes satisfy the same equations (3.1) and (3.2), but the external frequency k is taken to be the same as the internal frequency k_m. To avoid confusion, we will denote these QB frequencies by $\tilde{k}_m$. Since the Fresnel reflection coefficient does not depend on $\text{Re}[\tilde{k}_m]$, if we neglect the frequency-dependence of the refractive index, the $\tilde{k}_m$'s are equally spaced in the complex plane and have a fixed imaginary part

$$\tilde{k}_m = \frac{1}{n_1 a}\left[(m+\frac{1}{2})\pi - \frac{i}{2}\log(\frac{n_1-n_2}{n_1+n_2})\right],\ (m=0,1,2,...). \tag{3.6}$$

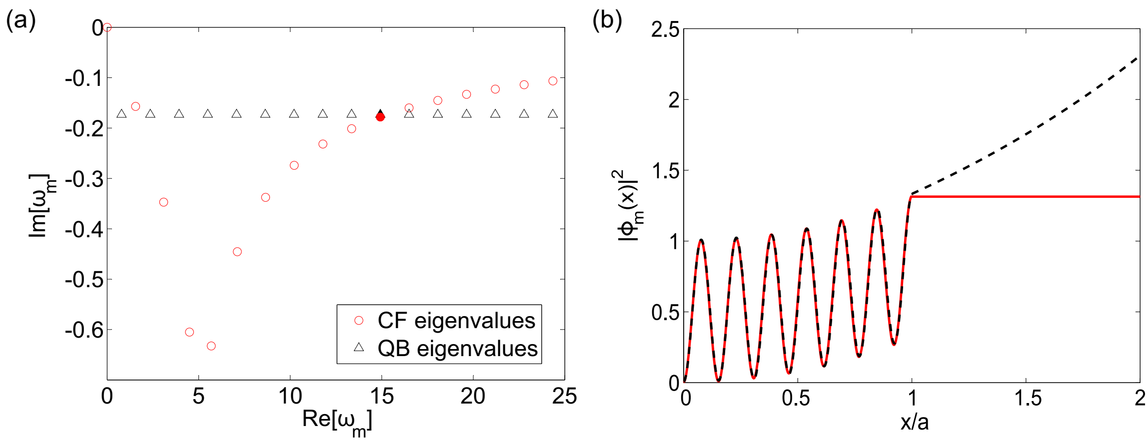

Figure 3.2: (a) Complex frequencies of the CF and QB states in a one-dimensional edge-emitting laser with refractive index $n_1 = 2$ and length $a = 1$. The refractive index n_2 outside the cavity is taken to be 1. The CF frequencies are calculated using $k = \text{Re}[\tilde{k}_m]$ of the QB mode $\tilde{k}_m = 10.2102 - 0.2747i$ (filled black triangle), and one of them with $k_m = 10.2191 - 0.2740i$ (filled red circle) is very close to this QB mode. (b) Spatial profiles of the pair of CF state (red solid curve) and the QB mode (black dashed curve) marked by filled symbols in (a). They are very similar in the cavity but the QB mode grows exponentially outside.

.

If the cavity has a relatively high quality factor and the external frequency k is chosen to be close to the real part of one of the QB frequencies $\tilde{k}_m$, there is one CF frequency which is essentially the same as this $\tilde{k}_m$ and their spatial profiles look identical in the cavity (Fig. 3.2). The difference of these two frequencies reduces as we increase k or the index contrast (see Appendix. A). But since the QB mode has a complex frequency outside the cavity, its spatial profile grows exponentially as $x \to \infty$ while the amplitude of the CF state is a constant and conserves the photon flux. The other k_m's, while they have $\mathrm{Re}[k_m] \approx \mathrm{Re}[\tilde{k}_m]$ (hence their free spectral ranges are similar), have quite different imaginary parts, emphasizing that CF states are *not* QB modes.

The shape of the CF spectrum shown in Fig. 3.2(a) can be understood analytically. To simplify the notation, we define $Z_m = n_1 k_m a \equiv q_m - i\kappa_m$ and $Z = n_2 k a$ and call their ratio $Z_m/Z \equiv \epsilon_m$. Eq. (3.3) can then be rewritten in terms of Z_m and ϵ_m:

$$e^{2iZ_m} = -\frac{2}{\epsilon_m - 1} - 1. \tag{3.7}$$

By taking the logarithm of the modulus on both sides, we have

$$\kappa_m = \frac{1}{2} \ln \left| \frac{2}{\epsilon_m - 1} + 1 \right|. \tag{3.8}$$

From the equation above we know κ_m approaches zero when $\epsilon_m \sim 0$ or $|\epsilon_m| \gg 1$. This explains why the complex CF frequencies become closer to the real axis in the limits $0 \leq q_m \ll |Z|$ and $q_m \gg |Z|$. In these two limits the *r.h.s* of Eq. (3.2) becomes close to either zero or infinity, and we know from the properties of the tangent function that $q_m \approx \pi\, m$ $(m = 0, 1, 2, ...)$ and $q_m \approx (\pi + 1/2)\, m$ in the two limits, respectively. Therefore we see that there is a "phase shift" in the real part of the complex CF frequencies when it increases, which is different from the behavior of the QB modes whose real parts are always proportional to half integer times π.

The *r.h.s* of Eq. (3.8) is maximized when $\epsilon_m \sim 1$, which means the CF spectrum has a minimum in the imaginary part near $Z_m \sim Z$ (see Fig. 3.2(a)). One interesting question is whether the minimum tends to infinity as one frequently encounters when dealing with complex tangent functions. To answer this question, we first write $\epsilon_m \equiv \epsilon_0 - i\epsilon_1$ and emphasize that both ϵ_0 and ϵ_1 are positive[1]. For simplicity, we take $n_2 = 1$ and n_1 to be

[1]Eq. (3.3) is even in k_m, and by default we take the complex CF frequencies with a positive real part.

real, and drop the subscript of the latter. The modulus of Eq. (3.7) can be rewritten as

$$\begin{aligned} e^{2Z\epsilon_1} &= \left|\frac{1+\epsilon_0 - i\epsilon_1}{1-\epsilon_0-i\epsilon_1}\right| \\ &= \left[1+\frac{4\epsilon_0}{(1-\epsilon_0)^2+\epsilon_1^2}\right]^{\frac{1}{2}}. \end{aligned} \tag{3.9}$$

For any given ϵ_0, the $l.h.s$ of Eq. (3.9) increases monotonically with ϵ_1 while the $r.h.s$ decreases monotonically with ϵ_1, which means ϵ_1, and hence $\mathrm{Im}\,[k_m]$, is bounded. To give an estimate of the maximum of ϵ_1, we use the fact that $\epsilon_0 \sim 1$ near the bottom of the valley and Eq. (3.9) is simplified to

$$Z\epsilon_1 = \frac{1}{4}\ln\left[1+\frac{4}{\epsilon_1^2}\right]. \tag{3.10}$$

Since $Z = ka$ is normally chosen to be larger than $\frac{\ln 5}{4} \sim 0.4$, we know immediately that ϵ_1 has to be smaller than unity. In the case shown in Fig. 3.2 the above expression gives $\epsilon_1 = 0.1329$, or $\min(\mathrm{Im}[k_m]) = -0.6784$, which is just below the imaginary part of the CF state near the bottom of the valley ($k_m = 5.6894 - 0.6326i$). If we vary k so that there is one CF frequency which sits right at the bottom of the valley, the estimated lower limit of $\mathrm{Im}[k_m]$ is even closer to the numerical value. For example, the two values are -0.7080 and -0.7050 when $k = 12.0$ in this one-dimensional case.

3.2 Multi-layer one-dimensional edge-emitting laser cavities

If the cavity index $\epsilon_c(x)$ is not a constant, for examples, in a multi-layer system such as a Distributed Feedback (DFB) laser (see Fig. 3.3), the analytical form of the equation that the complex CF frequencies satisfy is rather complicated. In practice we mainly use two numerical approaches to find the complex CF frequencies and the corresponding $\Psi_\mu(x)$: (1) discretizing space and turning ∇^2 into a matrix (2) using the transfer matrix approach. The implementation of the outgoing boundary condition in the first approach was pointed out to me by our colleague, Stefan Rotter, and the second approach is adapted from the description in Ref. [76]. We will assume the cavity emits in both the forward and the backward directions for generality.

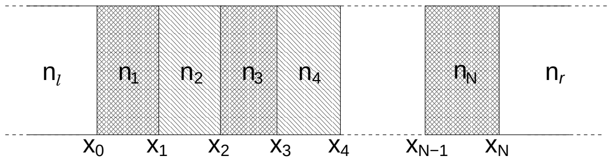

Figure 3.3: Schematic of a multi-layer one-dimensional edge-emitting cavity. This setup can be applied to Distributed Feedback lasers and one-dimensional aperiodic and random lasers.

3.2.1 Discretization method

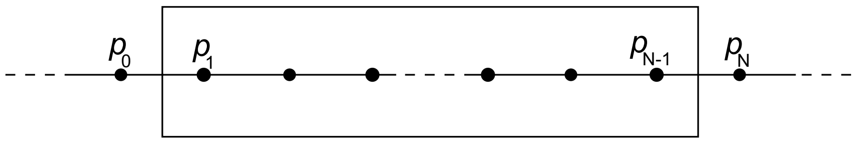

Figure 3.4: The discretization scheme of a one-dimensional laser cavity.

In the discretization method N equally spaced grid points are placed in the cavity. The refractive indices outside the two sidewalls are denoted by n_l and n_r, respectively. The first point p_1 is placed $\Delta/2$ from the left boundary of the cavity, where Δ is the spacing between two nearby grid points. Two facilitative points p_0 and p_{N+1} are placed outside the cavity (one on each side), each $\Delta/2$ away from the boundary on its side. The Helmholtz equation at the nth point p_n is

$$\frac{\phi_{n+1} + \phi_{n-1} - 2\phi_n}{\Delta^2} = -\epsilon_n k_m^2 \phi_n, \tag{3.11}$$

where ϕ_n and ϵ_n are the values of the CF state and the dielectric function at p_n. At p_1 the out-going boundary condition $(\phi_1 - \phi_0)/\Delta = -in_l k(\phi_1 + \phi_0)/2$ gives

$$\phi_0 = \frac{2 + in_l k\Delta}{2 - in_l k\Delta}\phi_1 \equiv \beta_l \phi_1, \tag{3.12}$$

with which we to eliminate ϕ_0 in Eq. (3.11) at p_0

$$\frac{(\beta_l - 2)}{\Delta^2}\phi_1 + \frac{1}{\Delta^2}\phi_2 = -\epsilon_1 k_m^2 \phi_1. \tag{3.13}$$

The Helmholtz equation at p_N can be derived similarly using $\beta_r \equiv (2+in_r k\Delta)/(2-in_r k\Delta)$. These N discretized Helmholtz equations constitute an generalized eigenvalue problem

$$\begin{pmatrix} \frac{2-\beta_l}{\Delta^2} & \frac{-1}{\Delta^2} & & & \\ \frac{-1}{\Delta^2} & \frac{2}{\Delta^2} & \frac{-1}{\Delta^2} & & \\ & \cdots & \cdots & \cdots & \\ & & \frac{-1}{\Delta^2} & \frac{2}{\Delta^2} & \frac{-1}{\Delta^2} \\ & & & \frac{-1}{\Delta^2} & \frac{2-\beta_r}{\Delta^2} \end{pmatrix} \begin{pmatrix} \phi_1 \\ \phi_2 \\ \cdots \\ \phi_{N-1} \\ \phi_N \end{pmatrix} = k_m^2 \begin{pmatrix} \epsilon_1 & & & & \\ & \epsilon_2 & & & \\ & & \cdots & & \\ & & & \epsilon_{N-1} & \\ & & & & \epsilon_N \end{pmatrix} \begin{pmatrix} \phi_1 \\ \phi_2 \\ \cdots \\ \phi_{N-1} \\ \phi_N \end{pmatrix} \tag{3.14}$$

with the eigenvalue $\lambda_m = k_m^2$ and the eigenvector $\Phi_m = \{\phi_1, ..., \phi_N\}^T$. Since the matrix operator H on the left hand side of Eq. (3.14) is symmetric, the transpose of each of its right eigenvectors is its left eigenvector with the same eigenvalue. Therefore, we recover the orthogonality relation

$$\{\Phi_m\}^T B \Phi_{m'} = \delta_{mm'} \tag{3.15}$$

where B is the diagonal matrix containing all the ϵ_n in Eq. (3.14).

If the dielectric function $\epsilon(x)$ has a certain parity, the problem above can be reduced to half of its size by imposing either a Dirichlet (odd parity) or Neumann (even partiy) at the symmetry center. The CF solutions of the one-sided case are exactly the solutions in the first scenario.

3.2.2 Transfer matrix method

Consider a monochromatic wave traveling through the dielectric laser cavity shown in Fig. 3.3. To avoid losing any generality, we write the wavefunction as

$$\varphi(x) = \begin{cases} \alpha_0 \, e^{-i\, n_l \, k_0 \, (x-x_0)} + \beta_0 e^{i\, n_l \, k_0 \, (x-x_0)}, & x < x_0 \\ \alpha_\nu \, e^{-i\, n_\nu \, k_\nu \, (x-x_\nu)} + \beta_2 e^{i\, n_\nu \, k_\nu \, (x-x_\nu)}, & x_{\nu-1} < x < x_\nu \\ \alpha_{N+1} \, e^{-i\, n_r \, k_{N+1} \, (x-x_N)} + \beta_{N+1} e^{i\, n_r \, k_{N+1} \, (x-x_0)}, & x > x_N \end{cases} \tag{3.16}$$

and ν runs from 0 to N. The amplitudes of the left and right traveling waves in the νth layer (α_ν, β_ν) and in the $(\nu+1)th$ layer $(\alpha_{\nu+1}, \beta_{\nu+1})$ can be connected using the continuity condition of $\varphi(x)$ and its derivative at x_ν:

$$\begin{pmatrix} \alpha_\nu \\ \beta_\nu \end{pmatrix} = D_\nu^{-1} D_{\nu+1} P_{\nu+1} \begin{pmatrix} \alpha_{\nu+1} \\ \beta_{\nu+1} \end{pmatrix}. \tag{3.17}$$

The matrices in the equation above are defined by

$$D_\nu \equiv \begin{pmatrix} 1 & 1 \\ n_\nu k_\nu & -n_\nu k_\nu \end{pmatrix}, \quad P_\nu \equiv \begin{pmatrix} e^{i n_\nu k_\nu (x_\nu - x_{\nu-1})} & 0 \\ 0 & e^{-i n_\nu k_\nu (x_\nu - x_{\nu-1})} \end{pmatrix}. \tag{3.18}$$

Due to the phase convention we use in Eq. (3.16), the transfer matrix connecting the amplitudes across the Nth interface $(x = x_N)$ is slightly different from Eq. (3.17):

$$\begin{pmatrix} \alpha_N \\ \beta_N \end{pmatrix} = D_N^{-1} D_{N+1} \begin{pmatrix} \alpha_{N+1} \\ \beta_{N+1} \end{pmatrix}, \tag{3.19}$$

and n_{N+1} should be taken as n_r. The total transfer matrix M connecting (α_0, β_0) and $(\alpha_{N+1}, \beta_{N+1})$ is then obtained by applying the operator in Eq. (3.17) repeatedly at each interface from x_0 to x_{N-1} and multiplying the matrices in Eq. (3.19):

$$\begin{aligned}
\begin{pmatrix} \alpha_0 \\ \beta_0 \end{pmatrix} &= D_0^{-1} D_1 P_1 \begin{pmatrix} \alpha_1 \\ \beta_1 \end{pmatrix} \\
&= D_0^{-1} D_1 P_1 D_1^{-1} D_2 P_2 \begin{pmatrix} \alpha_2 \\ \beta_2 \end{pmatrix} \\
&= D_0^{-1} D_1 P_1 D_1^{-1} D_2 P_2 ... D_N^{-1} D_{N+1} \begin{pmatrix} \alpha_{N+1} \\ \beta_{N+1} \end{pmatrix} \\
&= \left\{ D_0^{-1} \left[\Pi_{\nu=1}^{N} D_\nu P_\nu D_\nu^{-1} \right] D_{N+1} \right\} \begin{pmatrix} \alpha_{N+1} \\ \beta_{N+1} \end{pmatrix} \\
&\equiv M(k_0, k_1, ..., k_{N+1}) \begin{pmatrix} \alpha_{N+1} \\ \beta_{N+1} \end{pmatrix}.
\end{aligned} \tag{3.20}$$

To find the mth CF frequency k_m, we first take the two external frequencies to be the same $k_0 = k_{N+1} \equiv k$ and replace all k_ν's ($\nu = 1, 2, ..., N$) by k_m. The transfer matrix M is then a function of the two frequencies k and k_m. The outgoing boundary condition requires $\beta_0 = \alpha_{N+1} = 0$, which means the matrix element

$$M_{22}(k, k_m) = 0. \tag{3.21}$$

k_m is then obtained by solving this equation at the given external frequency k. Once k_m is known, we choose a normalization (e. g., $\beta_{N+1} = 1$) and calculate (α_ν, β_ν) sequentially from the right to the left using Eq. (3.19) and (3.17).

In the one-sided case where there is a perfect mirror at x_0, we derive the transfer matrix connecting (α_1, β_1) and $(\alpha_{N+1}, \beta_{N+1})$ by repeating the procedure leading to Eq. (3.20). The Dirichlet boundary condition at x_0 requires $\alpha_1 = -\beta_1$, which means the equation that determines k_m is

$$M_{22}(k, k_m) + M_{12}(k, k_m) = 0. \tag{3.22}$$

3.2.3 Inhomogeneous gain medium

As we will see in Section 4.1, threshold lasing modes are not CF states in general if $\epsilon_c(\boldsymbol{x})$ is not a constant. This is to be expected for example in a cavity with uniform index but with a inhomogeneous gain medium or pump profile. The amplification rate of each CF state is homogeneous inside the last scattering surface, but this is not the case for TLMs when either the gain medium or the pump profile is inhomogeneous. In the extreme case where $D_0(\boldsymbol{x})$ has abrupt discontinuities similar to the one shown in Fig. 2.2, we are better off using the gain region CF states instead. The GRCF approach is most suitable if the index of refraction within each gain/pump region is a constant, for example, in a DFB laser where the gain medium resides in only the odd or even layers. For now we neglect the possibility of reabsorption of emitted photos by the uninverted gain medium in the umpumped gain regions, thus treating inhomogeneous pump and inhomogeneous gain as equivalents.

As a simple illustration, we consider a two-layer edge-emitting laser cavity shown in Fig. 3.5. Layer I and II are separated by an dielectric interface at $x = x_0$, and only Layer I is filled with the gain medium and externally pumped. We will refer to the outside region on the right as Region III.

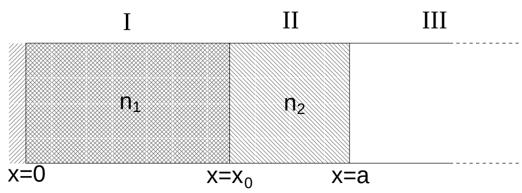

Figure 3.5: Schematic of a one-dimensional edge-emitting laser cavity with gain medium only in Layer I ($0 < x < x_0$).

The GRCF states of this cavity are determined by the following equations

$$\begin{cases} (\nabla^2 + n_1^2\, k_m^2)\varphi_m(x,\omega) = 0, & 0 < x < x_0, \\ (\nabla^2 + n_2^2\, k^2)\varphi_m(x,\omega) = 0, & x_0 < x < a, \\ (\nabla^2 + \quad k^2 \quad)\varphi_m(x,\omega) = 0, & x > a. \end{cases} \tag{3.23}$$

By imposing the Dirichlet boundary condition at $x=0$ and the outgoing boundary condition at $x=a$, we write the formal solution of a GRCF state as

$$\varphi_m(x,\omega)=\begin{cases}\sin\left(n_1k_mx\right), & 0<x<x_0\\ \alpha_m\,e^{in_2kx}+\beta_m\,e^{-in_2kx}, & x_0<x<a\\ c_m\,e^{ikx}, & x>a\end{cases}\cdot \tag{3.24}$$

Notice that the wavevector in Layer II is the same as the external k, which is a real quantity. This choice is quite natural since, due to lack of the gain medium, the lasing states are not amplified in Layer II. The GRCF frequencies k_m are the solutions of the following equation

$$\tan\left(n_1k_mx_0\right)=\frac{n_1k_m}{i\,n_2\,k}\frac{1+\frac{n_2-1}{n_2+1}\,e^{2\,i\,n_2k(a-x_0)}}{1-\frac{n_2-1}{n_2+1}\,e^{2\,i\,n_2k(a-x_0)}}, \tag{3.25}$$

which is obtained by requiring that $\varphi_m(x,\omega)$ and its derivative at $x=x_0$ and $x=a$ are continuous.

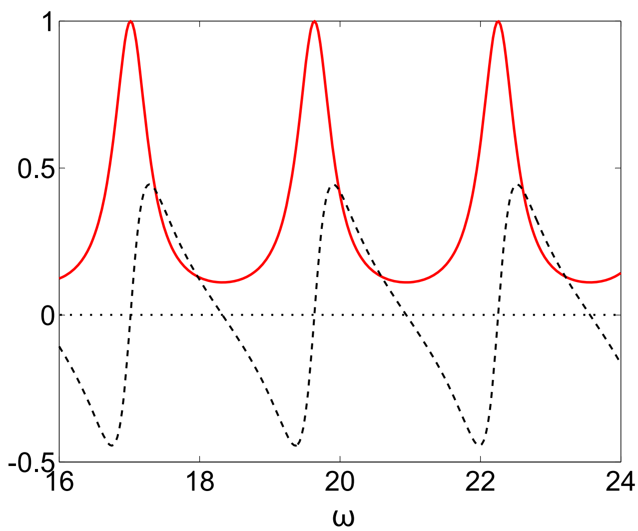

Figure 3.6: The real (red solid curve) and imaginary part (black dashed curve) of the effective index n_2'. We use $n_2=3$ and $x_0/a=0.5$. The dotted line indicates the position of zeros.

If we define

$$n_2' = n_2 \frac{1 - \frac{n_2-1}{n_2+1}\, e^{2\,i\,n_2 k(a-x_0)}}{1 + \frac{n_2-1}{n_2+1}\, e^{2\,i\,n_2 k(a-x_0)}}, \tag{3.26}$$

and substitute it into Eq. (3.25), we end up with an equation which has the same form as Eq. (3.3). This implies that the system under discussion is equivalent to a uniformly pumped cavity of length x_0 placed in an environment with the index n_2'. For a given x_0, the dispersion curve of the effective environment shows multiple resonances and is a periodic function of k (see Fig. 3.6). $\mathrm{Re}\,[n_2']$ varies between n_2^{-2} and 1, and it reaches its extremes where k satisfies $\sin[2\,n_2 k(a-x_0)] = 0$. There are also the frequencies where $\mathrm{Im}\,[n_2']$ varnishes.

Fig. 3.7 shows the quantized GRCF frequencies calculated with $k = 20$ and different values of x_0. All these series have similar shapes as the original CF states, which is not surprising after the analogy introduced above. The bottom of the valley varies with x_0 ($\mathrm{Re}\,[k_m] \approx \mathrm{Re}\,[n_2']\,k/n_1$), and the spacing between adjacent GRCF frequencies increases as we decrease x_0. Notice that the inhomogeneous gain profile changes the density of the the GRCF spectrum and shifts it downwards in the complex plane, which means that it effectively reduces the size of the cavity.

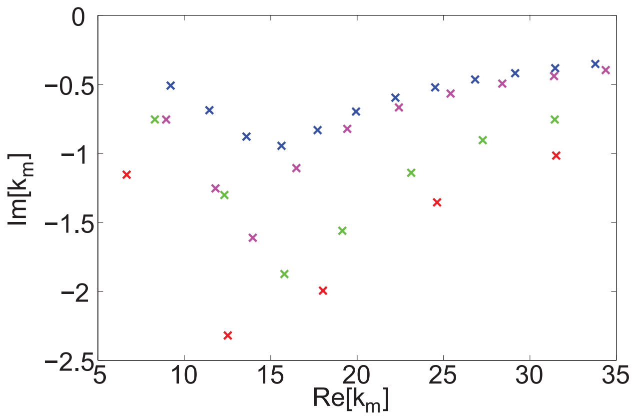

Figure 3.7: Series of gain region CF frequencies in the edge-emitting cavity shown in Fig. 3.5. The color scheme used are: blue ($x_0 = 0.9$), purple ($x_0 = 0.7$), green ($x_0 = 0.5$), red ($x_0 = 0.3$). The parameters used are $k = 20$, $a = 1$, $n_1 = 1.5$ and $n_2 = 1.1$.

The coefficients determining the spatial profile of the GRCF states in Eq. (3.24) depend strong on x_0:

$$\begin{cases} \alpha_m = \frac{1}{2}\left[\sin\left(n_1 k_m x_0\right) + \frac{n_1 k_m}{i n_2 k}\cos\left(n_1 k_m x_0\right)\right]\, e^{-i\, n_2 k x_0}, \\ \beta_m = \frac{1}{2}\left[\sin\left(n_1 k_m x_0\right) - \frac{n_1 k_m}{i n_2 k}\cos\left(n_1 k_m x_0\right)\right]\, e^{i\, n_2 k x_0}, \\ c_m = \frac{2\, n_2}{n_2+1}\, e^{i\,(1-n_2)k}\, \alpha_m. \end{cases} \tag{3.27}$$

For comparison we plot the GRCF states with different values of x_0 in Fig. 3.8. They are normalized to have the same intensity at the right boundary, and they look quite different from the uniformly amplified CF state. We note that the amplification rate of the GRCF states in Layer I becomes larger when the length of the gain region is reduced, indicating a higher pump is need to compensate for the increasing cavity loss. Therefore, we expect that the lowest threshold $D_{th}^{(1)}$ will increase as a result of a shortened gain region. A reasonable guess is that $D_{th}^{(1)}$ is inversely proportional to x_0, and the numerical calculation agrees with this prediction (see inset of Fig. 3.8). The fluctuation of the threshold around the fitting curve reflects the fluctuation of the distance between the atomic transition frequency and the closest GRCF eigenvalue when x_0 is varied. The method we use to calculate the threshold will be introduced in Section 4.1.

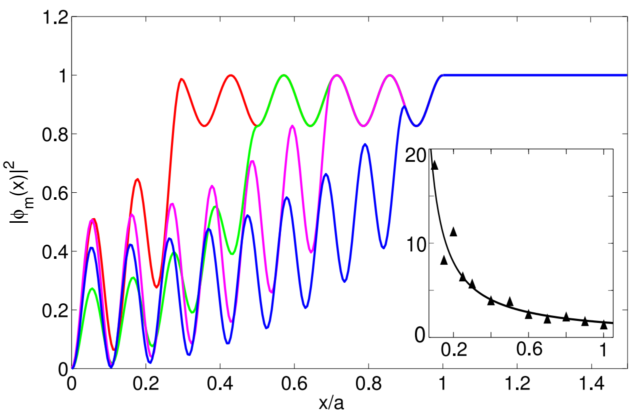

Figure 3.8: GRCF states calculated in the edge-emitting cavity shown in Fig. 3.5. The amplification rate of the wavefunction in Region I becomes larger when we decrease x_0. The parameters and color scheme used are the same as in Fig. 3.7. Inset: The lowest threshold $D_{th}^{(1)}$ increases as $1/x_0$ as x_0 is reduced. The fitting curve is given by $D_0 = 1.6 \cdot x_0^{-1}$

.

The frequencies of the GRCF states have a complex dependence on the external frequency k even when the passive cavity has no index mismatch between the layers. They can shift a distance a few times the average spacing along the real axis and the absolute values of their imaginary parts can be very large (see Fig. 3.9(b)). Thus the spacing of the real parts of the GRCF states may not be a good measure of the free spectral range, and the spatial profiles of the GRCF states can be dramatically different at different values of k. For example, the GRCF frequency $k_m(k = 20) = 29.82 - 1.609i$ shifts to $18.72 - 7.459i$ when k is reduced to 18, and its amplitude becomes exponentially increasing inside the gain region towards the gain boundary inside the cavity (see inset, Fig. 3.9(b)). As a comparison, we plot in Fig. 3.9(a) the shifts of the CF frequencies when varying the external frequency assuming a homogeneous gain; their real parts change slowly with k while their imaginary parts are bounded by the value given by Eq. (3.10). It should be noted, however, a GRCF state becomes a threshold lasing mode only when the external frequency is tuned to the corresponding lasing frequency. The frequency and spatial profile of the threshold lasing modes in this case is studied more closely in Chapter 8.

The general methods of finding the GRCF states will be discussed in Section 3.6, but the transfer matrix approach introduced in Section 3.2.2 is probably the best way to obtain them in multi-layer one-dimensional systems. The modification is straightforward: we replace the CF frequency k_m in the gain-free region inside the LSS by the real frequency k and solve the two-component equation (3.20) for k_m.

3.3 Uniform micro-disk lasers

When introducing the CF states in Section 2.4, we used the two-dimensional micro-disk cavity as an example to show how to reconstruct the degenerate CF subspace to preserve the orthogonality (2.39). In fact, we can also introduce a set of dual functions $\{\bar{\varphi}_m(\boldsymbol{x})\}$ and use the biorthogonality relation (2.48) when decomposing the lasing modes and the

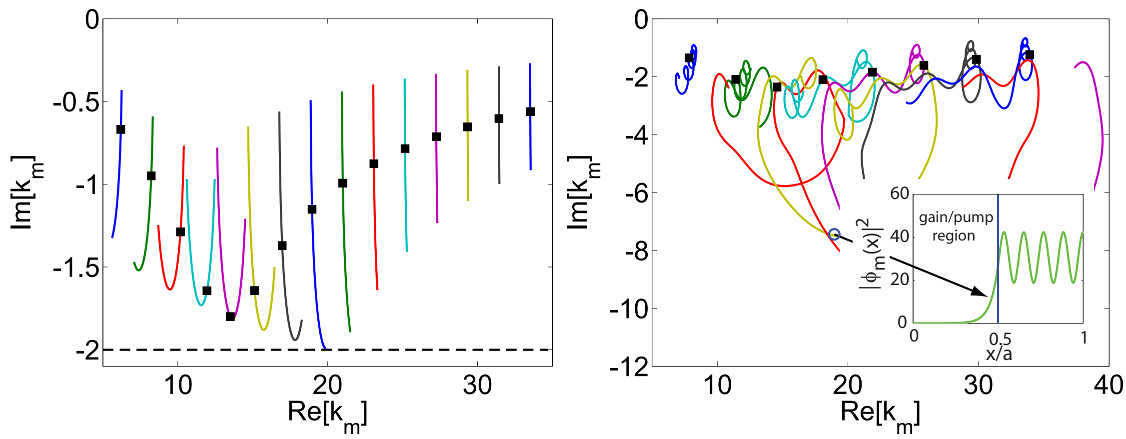

Figure 3.9: (a) Shift of CF frequencies when the external frequency k is tuned from 10 to 30. The cavity is a uniform one-dimensional slab of index $n = 1.5$ with a constant $D_0(x)$. The ones calculated at $k = 20$ are highlighted by black squares. The dashed line shows the lower bound $\text{Im}[k_m] = 2.0$ of the imaginary part of the CF states given by Eq. (3.10) using $k = 30$. (b) Shift of GRCF frequencies when the external frequency changes from k =10 to 30. The cavity is the same as in (a) but with the gain medium fills only the left half of the cavity. The GRCF states calculated at $k = 20$ are highlighted by black squares. The spatial profile of the circled state $k_m(k = 18) = 18.7192 - 7.4593i$ is shown in the inset.

Green's function in the CF basis. In this approach the CF states can be written as

$$\varphi_{(m,\,n)}(r,\phi,\omega) = \begin{cases} \mathrm{J}_m(n_1 k_{(m,\,n)} r)\, e^{im\phi}, & r < R, \\ \dfrac{\mathrm{J}_m(n_1 k_{(m,\,n)} R)}{\mathrm{H}^+_m(n_2 k R)}\, \mathrm{H}^+_m(n_2 k r)\, e^{im\phi}, & r > R, \end{cases} \tag{3.28}$$

where $(m,\, n)$ are the angular and radius quantum numbers and n_1 and n_2 are the refractive indices inside and outside the cavity. Notice we have included the continuity condition of the CF state at $r = R$ explicitly in the equation above. The outgoing boundary condition is incorporated by using the Hankel function of the first kind outside the cavity, and $k_{(m,\,n)}$ is determined by the continuity of the radius derivative of $\varphi_{(m,\,n)}$:

$$\frac{n_1 k_{(m,\,n)}\, \mathrm{J}'_m(n_1 k_{(m,\,n)} R)}{\mathrm{J}_m(n_1 k_{(m,\,n)} R)} = \frac{n_2 k\, \mathrm{H}^{+'}_m(n_2 k R)}{\mathrm{H}^+_m(n_2 k R)} \tag{3.29}$$

We will refer to the CF states within the cavity as CF Bessel functions.

The dual states $\{\bar{\varphi}_m(\boldsymbol{x})\}$ are the solutions of the wave function (2.33) and (2.35) with the incoming boundary condition:

$$\bar{\varphi}_{(m,\,n)}(r,\phi,\omega)=\begin{cases}\mathrm{J}_m(n_1k_{(m,\,n)}r)\,e^{im\phi}, & r<R,\\ \frac{\mathrm{J}_m(n_1k_{(m,\,n)}R)}{\mathrm{H}^-_m(n_2kR)}\,\mathrm{H}^-_m(n_2kr)\,e^{im\phi}, & r>R.\end{cases} \tag{3.30}$$

It is easy to check that when $m\neq m'$ the biorthogonality holds due to the vanishing integral in the azimuthal direction. For the CF states with the same angular momentum number m but different radial quantum number, the integral in Eq. (2.48) can be rewritten as

$$\begin{aligned}
&\int_{r<R} d\boldsymbol{x}\,\bar{\varphi}^*_{m,\,n}(\boldsymbol{x},\omega)\,\varphi_{m,\,n'}(\boldsymbol{x},\omega)\\
=\;&\frac{1}{k^2_{m,\,n}-k^2_{m,\,n'}}\int_{r<R} d\boldsymbol{x}\;\left[\bar{\varphi}^*_{m,\,n'}(\boldsymbol{x},\omega)\nabla^2\varphi_{m,\,n}(\boldsymbol{x},\omega)-\varphi_{m,\,n}(\boldsymbol{x},\omega)\nabla^2\bar{\varphi}^*_{m,\,n'}\nu(\boldsymbol{x},\omega)\right]\\
=\;&\frac{1}{k^2_{m,\,n}-k^2_{m,\,n'}}\int Rd\theta\left[\bar{\varphi}^*_{m,\,n'}(\boldsymbol{x},\omega)\frac{\partial\varphi_{m,\,n}(\boldsymbol{x},\omega)}{\partial r}-\varphi_{m,\,n}(\boldsymbol{x},\omega)\frac{\partial\bar{\varphi}^*_{m,\,n'}(\boldsymbol{x},\omega)}{\partial r}\right]\\
=\;&\frac{2\pi n_1R}{k^2_{m,\,n}-k^2_{m,\,n'}}\left[k_{(m,\,n)}\mathrm{J}_m(n_1k_{(m,\,n')}R)\mathrm{J}'_m(n_1k_{(m,\,n)}R)-k_{(m,\,n')}\mathrm{J}_m(n_1k_{(m,\,n)}R)\mathrm{J}'_m(n_1k_{(m,\,n')}R)\right].
\end{aligned}$$

By substituting the derivatives of the Bessel's functions by their values given in Eq. (3.29), we see that indeed the biorthogonality holds.

In Fig. 3.10 we compare the spatial profiles of two CF states and the nearby QB modes. The quality factor of the extreme whispering-gallery (WG) modes in an ideal micro-disk laser cavity without defects can easily reach 10^{11}, and Fig. 3.10(a) shows one of them. In this high-Q limit, the difference between the CF and QB frequencies is extremely small, and their spatial profiles look identical both in the cavity and within a few radii from the boundary. Eventually the amplitude of the QB mode grows exponentially when $r\to\infty$ as given by the asymptotic form of the outgoing Hankel function. The ray correspondence of the extreme WG mode is a bundle of light rays undergoing total internal reflection in the cavity, but in the wave picture the mode still couples to the outside by evanescent tunneling due to the finite curvature of the cavity boundary [23]. This holds true for both the QB modes and the CF states. For lossy WG modes like the one shown in Fig. 3.10(b), we see the spatial profile of the QB mode differs from that of the CF state immediately

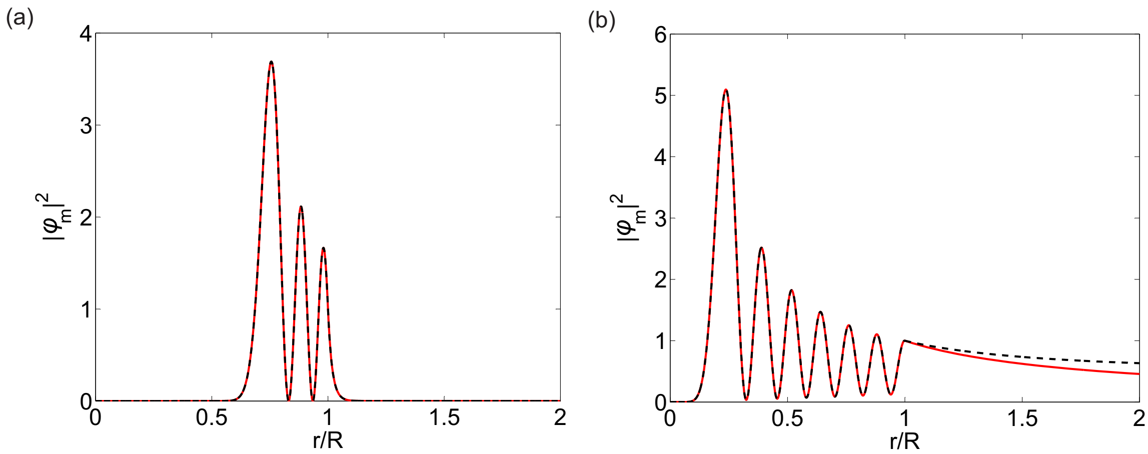

Figure 3.10: Radial spatial profiles of two pairs of QB (black dashed line) and CF (red solid line) states inside a micro-disk cavity of refractive index $n = 2.5$. (a) An extreme WG mode with $m = 35$. The QB frequency is $\tilde{k}_p = 19.9268 - 1.153 \times 10^{-11}i$, and the CF frequency is $k_p(k = 19.9268) = 19.9268 - 1.161 \times 10^{-11}i$. (b) A lossy WG mode with $m = 5$. The QB frequency is $\tilde{k}_q = 10.8135 - 0.1543i$, and the CF frequency is $k_q(k = 10.8135) = 10.8165 - 0.1543i$.

outside the cavity. From the position of the caustic (i. e., the position of the first maxima of the spatial profile which is at $r \approx 0.24R$ in Fig. 3.10(b)) we can tell that the incident angle of the rays in the cavity is smaller than the critical angle ($\chi_c = \arcsin(1/n) = 0.41$).

Due to the isotropic symmetry of the micro-disk, the angular momentum is a conserved quantity in all physical states associated with it as long as the pump is homogeneous in the azimuthal direction. Therefore, each lasing mode, even above threshold, is made up of the CF states of the same angular momentum number m. Although the CF spectrum is much denser than that in the one-dimensional case, this implies that we only need to consider the few WG CF states with the lowest threshold and the ones nearby in frequency with the same m's in our calculation.

In the above discussion we assumed the light field in the cavity is TM polarized perpendicular to the plane of the disk, and the scalar Helmholtz equations (2.33) and (2.35) are satisfied by the electric field which is normal to the disk. The CF states can also be defined for TE polarized light with the same Helmhotlz equation of the magnetic field H_z. The outgoing boundary condition is similar to that in Eq. (3.29) by using the continuity of the quantity $\epsilon(\boldsymbol{x})^{-1}\frac{\partial H_z}{\partial r}$ at the boundary.

3.4 Two-dimensional asymmetric resonant cavity lasers

The lasers we have discussed in this chapter so far are essentially all one-dimensional (the Helmholtz equation in the micro-disk geometry is separable). In order to probe more interesting lasers, e. .g., the ARC lasers and random lasers introduced in Chapter 1, we need a general CF state solver in 2D and 3D. In this chapter we will focus on the 2D case, and the methods we will introduce can be easily generalized to 3D. One challenge of finding the CF states in these lasers is implementing the outgoing boundary condition since the boundaries of these cavities can be quite complicated.

One solution is to use a Generalized Fourier Series expansion, the CF Bessel functions (defined in the preceding section) expansion. In this approach we choose a circular LSS that encloses the laser cavity, representing a nominal gain region, and assume the index $n_{\mathcal{D}}$ inside the LSS is a constant. Depending on the properties of the cavity, $n_{\mathcal{D}}$ can either be chosen as the cavity index n_c (e. g., in a quadrupole cavity; see Fig. 1.2(b)) or the average index within the LSS (e. g., in a random laser with nano-particles in a dye solution). The CF Bessel function inside the LSS form a complete and orthogonal basis, and the lasing modes are obtained by solving the SALT equations 2.50 by treating the region inside the LSS as our cavity. This approach is mostly pursued by Y. D. Chong in Prof. A. Douglas Stone's group. In this approach we sacrifice the resemblance of the CF states to the lasing modes, which means a very large basis set is needed when the true cavity boundary is very different from a circle or the index inhomogeneities inside the LSS is strong.

In this thesis we use a different method: the discretization method in polar coordinates. We choose to work in polar coordinates because the outgoing boundary condition in two dimensions can be conveniently expressed in them. This method was initially developed by Stefan Rotter and Prof. A. Douglas Stone (see the online supplemental material of Ref. [65]), which is the two-dimensional generalization of the method introduced in Section 3.2.1. Similar to the method outlined above, we assume a disk-shaped gain region and choose its boundary as the LSS. We *do not* assume the index inside the LSS is a constant when constructing the CF basis. Cavities of any shape (e. g., the solid curve in

Fig. 3.11) can be centered and placed inside the LSS. The cavity does not necessarily have to be convex or single-connected as the out-going boundary condition is imposed on the circular LSS. Although the actual gain region may differ from the disk region we choose, we take into account the index inhomogeneity inside the cavity in this approach, which is a significant improvement compared with the CF Bessel functions expansion. The results given by the discretization method can be refined following the approaches introduced in Section 3.6 to take into account the spatial variation of the gain medium.

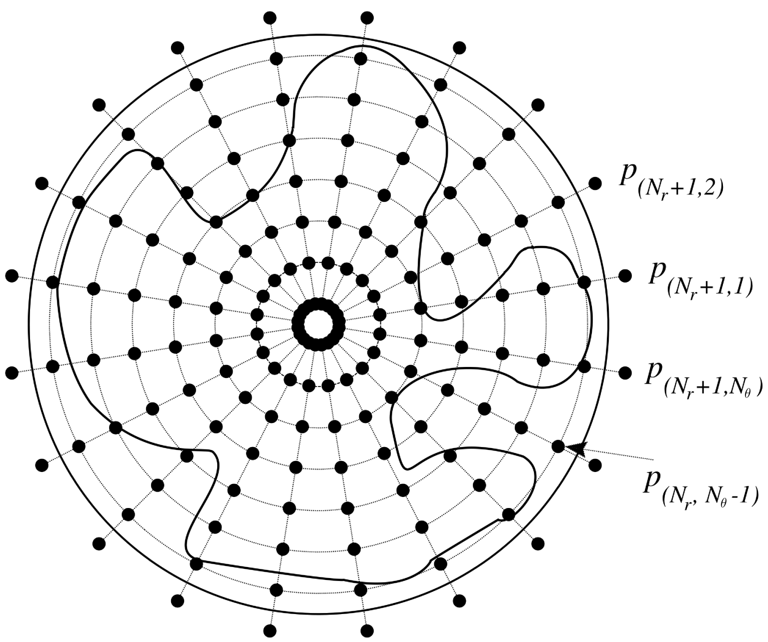

Figure 3.11: Discretization scheme of the two-dimensional geometry in polar coordinates.

As illustrated in Fig. 3.11, N_θ equally spaced grid points are laid on each ring, with the first one placed in the $\theta = \pi/N_\theta$ direction. The discretization in the radial direction [77] is similar to the scheme used in the preceding section: The first radial grid point is placed $\Delta_r/2$ from the origin, where Δ_r is the distance between two nearby radial grid points. It is pointed out in Ref. [78] that the direct replacement of the Laplacian by finite differences in the polar coordinates can lead to serious discretization errors, and a variational method [79] needs to be used to derive a better discretization scheme. This variational method is best suitable for problems with a non-Cartesian grid, and it is guaranteed to produce a symmetric discretization [80]. We will briefly discuss how it works in the following paragraphs.

The Helmholtz equation in an arbitrary domain (we will call it D) can be viewed as the result of extremizing the functional

$$E[\phi_m] \equiv \int_D d^2x \left[-\frac{(\nabla\phi_m)^2}{2} + \frac{k_m^2}{2}\epsilon\phi_m^2 \right] \tag{3.31}$$

with the constraint $\delta\phi_m|_{\partial D} = 0$:

$$\begin{aligned} \delta E[\phi_m] &= \int_D d^2x \left[-\nabla\phi_m \cdot \nabla\delta\phi_m + \epsilon k_m^2 \phi_m \delta\phi_m \right] \\ &= -\nabla\phi_m \cdot \delta\phi_m|_{\partial D} + \int_D d^2x \left[\nabla^2\phi_m + \epsilon k_m^2 \phi_m \right] \delta\phi_m \\ &= \int_D d^2x \left[\nabla^2\phi_m + \epsilon k_m^2 \phi_m \right] \delta\phi_m. \end{aligned} \tag{3.32}$$

∂D indicates the boundary of Domain D. The first step towards the proper discretization is to replace the integral in Eq. (3.31) by the sum over all the grid points $p_{(\mu,\,\nu)}$ in Domain D:

$$\begin{aligned} &E(\phi^m_{1,1}, ..., \phi^m_{\mu_0,\,\nu_0}, ..., \phi^m_{N_r,N_\theta}) \\ &\equiv \tfrac{1}{2}\textstyle\sum_{\mu=1}^{N_\theta} \Delta_\theta \sum_{\nu=1}^{N_r} \Delta_r \left[-r_{\mu+\frac{1}{2}} \left(\frac{\phi^m_{\mu+1,\,\nu} - \phi^m_{\mu,\,\nu}}{\Delta_r} \right)^2 - \frac{1}{r_\mu} \left(\frac{\phi^m_{\mu,\,\nu+1} - \phi^m_{\mu,\,\nu}}{\Delta_\theta} \right)^2 + r_\mu \left(\epsilon_{\mu,\,\nu} k_m^2 \phi^m_{\mu,\,\nu} \right)^2 \right]. \end{aligned} \tag{3.33}$$

Δ_θ is the angular distance between two nearby azimuthal grid points, and the notation $r_{\mu\pm\frac{1}{2}}$ stands for the center point between r_μ and $r_{\mu\pm1}$. Note that the first place $\nabla^2\phi_m$ is evaluated in the radial direction in Eq. (3.33) is at $r = r_{3/2}$ as $r_{1/2}$ in this notation is the origin.

The next step is to extremize E with respect to the amplitude of the wave function at all the grid points in side the domain:

$$\frac{\partial E}{\partial \phi^m_{\mu,\,\nu}} = 0. \tag{3.34}$$

The calculation is straightforward, which gives

$$\frac{r_{\mu-\frac{1}{2}}\,\phi^m_{\mu-1,\,\nu}+r_{\mu+\frac{1}{2}}\,\phi^m_{\mu+1,\,\nu}-2\,r_\mu\,\phi^m_{\mu,\,\nu}}{r_\mu(\Delta_r)^2}+\frac{\phi^m_{\mu,\,\nu-1}+\phi^m_{\mu,\,\nu+1}-2\,\phi^m_{\mu,\,\nu}}{(r_\mu\Delta_\theta)^2}+\epsilon_{\mu,\,\nu}k_m^2\,\phi^m_{\mu,\,\nu}=0. \tag{3.35}$$

Since the integrand in Eq. (2.50) is proportional to $r_\mu\phi^m_{\mu,\,\nu}\phi^n_{\mu,\,\nu}$ in the absence of modal interaction, we use a more convenient form of Eq. (3.35) in terms of $\rho^m_{\mu,\,\nu}\equiv\sqrt{r_\mu}\phi^m_{\mu,\,\nu}$:

$$\frac{\frac{r_{\mu-\frac{1}{2}}}{\sqrt{r_\mu r_{\mu-1}}}\rho^m_{\mu-1,\,\nu}+\frac{r_{\mu+\frac{1}{2}}}{\sqrt{r_\mu r_{\mu+1}}}\rho^m_{\mu+1,\,\nu}-2\rho^m_{\mu,\,\nu}}{(\Delta_r)^2}+\frac{\rho^m_{\mu,\,\nu-1}+\rho^m_{\mu,\,\nu+1}-2\,\rho^m_{\mu,\,\nu}}{(r_\mu\Delta_\theta)^2}+\epsilon_{\mu,\,\nu}k_m^2\,\rho^m_{\mu,\,\nu}=0. \tag{3.36}$$

Note that if we had directly discretized the continuous differential equation ρ^m satisfies

$$\left(\frac{\partial^2}{\partial r^2}+\frac{\partial^2}{r^2\partial\phi^2}+\frac{1}{4r^2}+\epsilon k_m^2\right)\rho^m=0, \tag{3.37}$$

we would had ended up with an equation different from Eq. (3.36):

$$\frac{\rho^m_{\mu-1,\,\nu}+\rho^m_{\mu+1,\,\nu}-(2-\frac{\delta_\mu^2}{4})\,\rho^m_{\mu,\,\nu}}{(\Delta_r)^2}+\frac{\rho^m_{\mu,\,\nu-1}+\rho^m_{\mu,\,\nu+1}-2\,\rho^m_{\mu,\,\nu}}{(r_\mu\Delta_\theta)^2}+\epsilon_{\mu,\,\nu}k_m^2\,\rho^m_{\mu,\,\nu}=0, \tag{3.38}$$

where $\delta_\mu\equiv\frac{\Delta_r}{r_\mu}$. Close to the origin δ_μ is of order unity, and the equation above differs dramatically from Eq. (3.36) which can be rewritten as

$$\frac{\rho^m_{\mu-1,\,\nu}+\rho^m_{\mu+1,\,\nu}-(2+\frac{\delta_\mu^2}{2})\rho^m_{\mu,\,\nu}}{(\Delta_r)^2}+\frac{\rho^m_{\mu,\,\nu-1}+\rho^m_{\mu,\,\nu+1}-2\,\rho^m_{\mu,\,\nu}}{(r_\mu\Delta_\theta)^2}+\epsilon_{\mu,\,\nu}k_m^2\,\rho^m_{\mu,\,\nu}=O(\delta_\mu^3). \tag{3.39}$$

The outgoing boundary condition in the two-dimensional case is considerably harder than that in the one-dimensional cavities: There is no local relation between $\phi^m_{N_r,\,\nu}$ and $\phi^m_{N_{r+1},\,\nu}$ for a given angle because the angular momenta of the wave functions are not known in advance. In the continuous form the CF states and their radial derivatives outside the disk have the following formal solutions:

$$
\begin{aligned}
\phi_> &= \sum_m a_m \frac{H_m^+(kr)}{H_m^+(kR)}\, e^{im\theta}, \\
\frac{\partial \phi_>}{\partial r} &= \sum_m a_m \frac{H_m^{+'}(kr)}{H_m^+(kR)}\, e^{im\theta} k.
\end{aligned} \tag{3.40}
$$

k is again the external lasing frequency. Now suppose the wave function on the $N_r th$ and $(N_r+1)th$ rings can be written as

$$
\begin{aligned}
\phi_{N_r,\,\nu} &= \textstyle\sum_m b_m\, e^{im\theta_\nu}, \\
\phi_{N_r+1,\,\nu} &= \textstyle\sum_m b_m(1+c_m\Delta_r)\, e^{im\theta_\nu},
\end{aligned} \tag{3.41}
$$

the radial derivative at $r=R$ and $\theta=\theta_\nu$ can then be approximated by

$$
\frac{\phi_{N_r+1,\,\nu}-\phi_{N_r,\,\nu}}{\Delta r} = \sum_m b_m\, c_m\, e^{im\theta_\nu}. \tag{3.42}
$$

Combine it with Eq. (3.40) and we have

$$
c_m = k\,\frac{a_m}{b_m}\frac{H_m^{+'}(kR)}{H_m^+(kR)}. \tag{3.43}
$$

The other equation involving the three expansion coefficients a_m, b_m and c_m is obtained by equating the discretized and continuous expressions for the mth Fourier coefficient of the CF state on the $(N_r+1)th$ ring

$$
b_m(1+c_m\Delta_r) = a_m \frac{H_m^+(k\, r_{N_r+1})}{H_m^+(kR)}, \tag{3.44}
$$

which when combined Eq. (3.43) gives

$$
c_m = \frac{kH_m^{+'}(kR)}{H_m^+(k\, r_{N_r+1}) - k\Delta_r H_m^{+'}(kR)}. \tag{3.45}
$$

In the end we have

$$\begin{aligned}
\phi_{N_r+1,\,\nu} &= \sum_m b_m(1+c_m\Delta_r)\, e^{im\theta_\nu} \\
&= \sum_{\nu'}\left[\frac{\Delta_\theta}{2\pi}\sum_m e^{im(\theta_\nu-\theta_{\nu'})}\left(1+\frac{k\Delta_r H_m^{+'}(kR)}{H_m^{+}(k\,r_{N_r+1})-k\Delta_r H_m^{+'}(kR)}\right)\right]\phi_{N_r,\,\nu'} \\
&\equiv \sum_{\nu'} V_{\nu,\,\nu'}\phi_{N_r,\,\nu'}, \qquad (3.46)
\end{aligned}$$

or

$$\rho_{N_r+1,\,\nu} = \sum_{\nu'} V_{\nu,\,\nu'}\sqrt{\frac{r_{N_r+1}}{r_{N_r}}}\rho_{N_r,\,\nu'}. \qquad (3.47)$$

By combining the set of $(N_r \times N_\theta)$ equations given by (3.36) and eliminating $\rho_{N_r+1,\,\nu}$ using Eq. (3.47), we once again derive a general eigenvalue problem

$$H\,\Phi_m = k_m^2 B\Phi_m \qquad (3.48)$$

which is similar to Eq. (3.14). The eigenvector Φ_m is a column vector containing all the $\rho_{\mu,\,\nu}$

$$\Phi_m = \{\rho_{1,1}, \rho_{1,2}, ..., \rho_{1,N_\theta}, \rho_{2,1}, \rho_{2,2}, ..., \rho_{2,N_\theta}, ..., \rho_{N_r,1}, ..., \rho_{N_r,N_\theta}\}^T, \qquad (3.49)$$

and B is a $(N_r\times N_\theta)$ by $(N_r\times N_\theta)$ diagonal matrix with $B_{(\mu-1)N_\theta+\nu,(\mu'-1)N_\theta+\nu'} = \epsilon_{\mu,\,\nu}\delta_{\mu,\mu'}\delta_{\nu,\,\nu'}$. The operator H is made up of a banded matrix H_0 and a $(N_\theta \times N_\theta)$ block H' in the lower right corner. H_0 is symmetric with nonzero elements on the 0, ± 1, and $\pm N_\theta$ diagonals

$$\left\{\begin{array}{lcl}
H_{(\mu-1)N_\theta+\nu,\,(\mu-1)N_\theta+\nu} &=& \frac{2}{(\Delta_r)^2}+\frac{2}{(r_\mu\Delta_\theta)^2}, \\
H_{(\mu-1)N_\theta+\nu,\,(\mu-1)N_\theta+\nu+1} &=& -\frac{1}{(r_\mu\Delta_\theta)^2}, \\
H_{(\mu-1)N_\theta+\nu,\,\mu N_\theta+\nu} &=& -\frac{r_{\mu+\frac{1}{2}}}{(\Delta_r)^2\sqrt{r_\mu r_{\mu+1}}},
\end{array}\right. \qquad (3.50)$$

and H' comes from the boundary condition when eliminating $\rho_{N_r+1,\,\nu}$, which is also symmetric:

$$H'_{\nu,\,\nu'} = -\frac{1}{(\Delta_r)^2}\frac{r_{\mu+\frac{1}{2}}}{r_\mu}V_{\nu,\,\nu'} = -\frac{1}{(\Delta_r)^2}\frac{r_{\mu+\frac{1}{2}}}{r_\mu}V_{\nu',\,\nu} = H'_{\nu',\,\nu}. \qquad (3.51)$$

Here we used the relation $H_{-m}^{+}(z) = (-1)^m H_m^{+}(z)$ and the definition of $V_{\nu,\,\nu'}$ in Eq. (3.46). Therefore, the matrix operator H is symmetric and $\{\Phi_m\}$ satisfy the orthogonality relation

Eq. (3.15) as in the one-dimensional case.

If the cavity has n_s symmetry axes, one can reduce the number of grid points in the azimuthal direction to N_r/n_s by imposing either Dirichlet or Neumann boundary condition on the symmetry axes. This procedure does not only help to reduce the execution time of the CF state solver, but more importantly, enables one to calculate the CF states in the deep semiclassical limit ($nkR \gg 1$) which is otherwise impossible due to the limitation of computer memory. To check this method we calculate the CF frequencies in a micro-disk laser by discretizing the cavity in the first quadrant and imposing symmetry boundary conditions along the $\theta = 0$ and $180°$ directions. The CF states with an odd angular momentum number m are given by the $\{+,-\}$ (or $\{+,-\}$) symmetry, and the ones with an even m are obtained using the $\{+,+\}$ (or $\{-,-\}$) symmetry. The results agree well with the solutions of the analytical expression (3.29) (see Fig. 3.12).

If the dielectric function within the LSS varies smoothly in the azimuthal direction, we can also solve for the coefficients of the Fourier transform of the wave functions on each ring instead (see Appendix C).

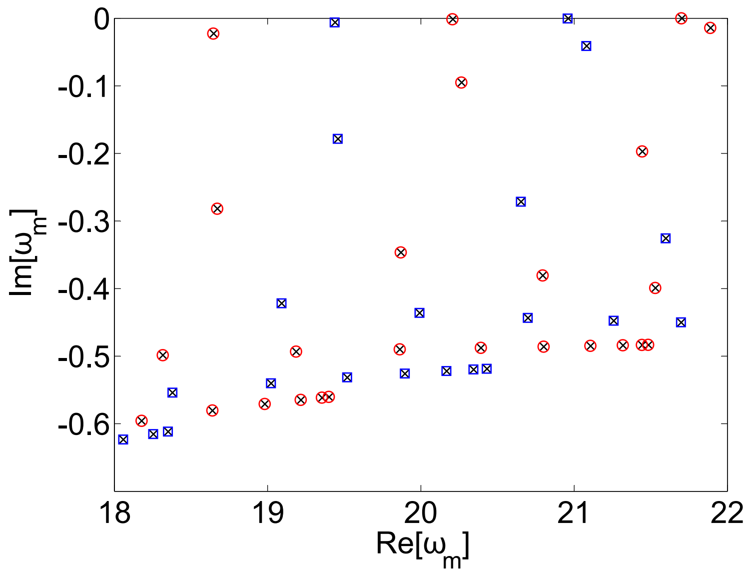

Figure 3.12: CF frequencies in a micro-disk cavity of index $n = 1.5$ and radius $R = 1$. The Red circles and blue squares represents the CF frequencies with even and odd angular momentum numbers, respectively. They are calculated using the discretization method with $N_r = N_\phi = 600$ and symmetry boundary conditions along the $\theta = 0$ and $180°$ directions. The black crosses are the result of solving the analytical expression (3.29).

Standard methods of finding the QB modes in micro-cavities such as the S-matrix method [81, 82, 83, 84] and the boundary integral method [85] can also be applied to the ARC lasers when modified to include the CF outgoing boundary condition. But in practice they are not as convenient as the discretization method which outputs the CF frequencies in the given frequency window all at once.

3.5 Random lasers

Random lasers (RLs), as discussed in the introduction, are extremely open and the photons generated by stimulated emission escape rapidly from the gain region. The linear resonances in a RL are strongly overlapping, which means the distribution of the QB eigenvalues is peaked far from the real axis and the distance is large compared with the spacing of nearby QB eigenvalues. In our model we treat the two-dimensional RL as an aggregate of sub-wavelength particles embedded in a disk-shaped gain medium of radius R (see Fig. 3.13(a)). To find the CF states we use the discretization method which was introduced in the preceding section to treat ARC lasers. Notice that the S-matrix method, as introduced in Ref. [83], cannot be applied to RLs because it requires that the boundary of the cavity is smooth and convex and that the refractive index in the cavity is a constant[2]. The boundary integral method in principle can be used to find CF frequencies in RLs, but it requires a boundary integral for each of scatterers in the system and the numerics become hard to track once we have hundreds or even thousands of scatterers.

Fig. 3.13(b) shows that the CF and QB frequencies in this case are significantly different but statistically similar. Although we can find some instances where a CF frequency and a QB frequency are close to each, there is no one-to-one correspondence between them in general, which is different from the what we have shown in high-Q cavities. Fig. 3.14 shows the comparison of the intensity of a CF state and the QB mode whose complex frequency is closest to that of the CF state. They have similar features, including the bright speckles near the edge of the cavity and the mixture of semi-straight and distorted wavefronts, but the overall intensity of the QB mode is much higher. In Chapter 7 we will show that the large amplification towards the cavity boundary is also a noticeable feature of the lasing

[2] Efforts of removing these limitations have been reported [84].

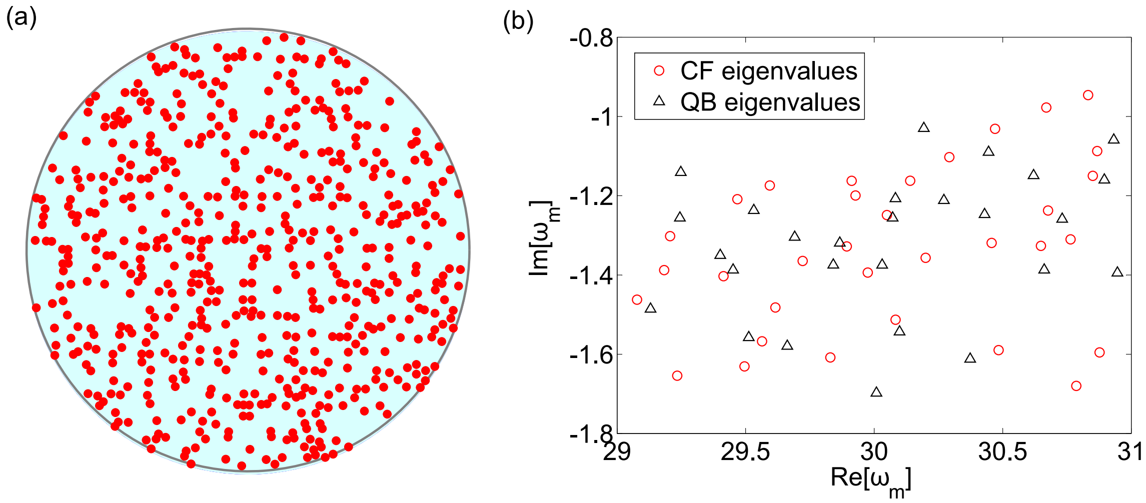

Figure 3.13: (a) Schematic of the configuration of nanoparticle scatterers in the disk-shaped gain region of a RL. (a) Comparison of CF and QB frequencies in a RL. The red circles and the black triangles represent the CF and QB frequencies, respectively. They have similar lifetimes and are statistically similar, but there is no one-to-one correspondence between them in general.

modes, which is due to the leaky nature of the RL.

3.6 General methods of finding the gain region constant-flux states in all dimensions

There are two general approaches to find the GRCF states in arbitrary dimensions. The first approach is treating GRCF states as TLMs and find them using the CF expansion. Although we still need a relatively large CF basis to obtain the GRCF states, once they are obtained we will use them in the nonlinear (above threshold) calculation. The size of the basis and the number of equations we need to solve simultaneously are then greatly reduced. To distinguish the GRCF states from the original CF states $\{\phi_m\}$, we will refer to them and their frequencies as $\{\phi_m^{(g)}\}$ and $\{k_m^{(g)}\}$ in the following discussion.

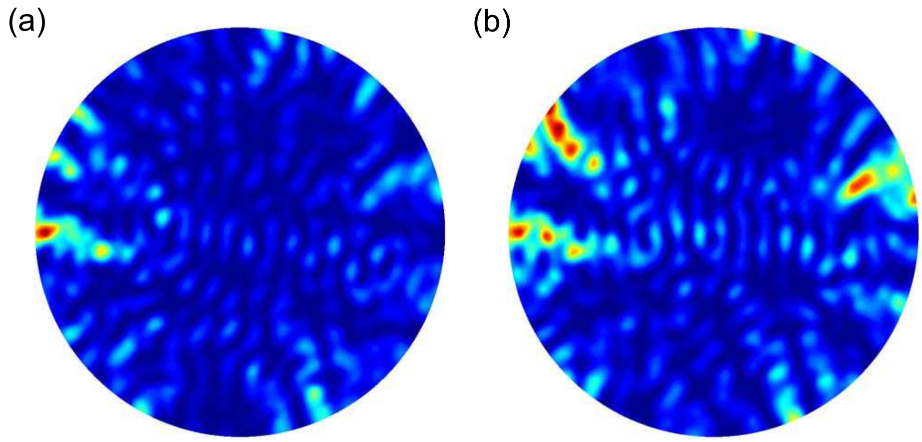

Figure 3.14: False color plots of (a) a CF state and (b) the QB mode whose complex frequency ($\tilde{k}_m = 29.8813 - 1.3790i$) is closest to that of the CF state ($k_m(k = 30) = 30.0058 - 1.3219i$). The wave functions are normalized by the orthogonality relation (2.39).

By expanding the GRCF state in the CF basis $\phi_m^{(g)}(\boldsymbol{x}) = \sum_{m'} a_{m'} \phi_{m'}(\boldsymbol{x})$ and substituting it into the Helmholtz equation $\phi_m^{(g)}(\boldsymbol{x})$ satisfies, we derive

$$\begin{cases} \sum_{m'} a_{m'}((k_m^{(g)})^2 - k_{m'}^2)\, \epsilon(\boldsymbol{x})\, \phi_{m'}(\boldsymbol{x}) = 0, & x \in \text{gain regions} \\ \sum_{m'} a_{m'}(k^2 - k_{m'}^2)\, \epsilon(\boldsymbol{x})\, \phi_{m'}(\boldsymbol{x}) = 0, & x \in \mathcal{D} \end{cases}. \tag{3.52}$$

$\mathcal{D}$ is the gain-free region inside the LSS. Now we apply the operator $\int_{\text{gain}} d\boldsymbol{x}\, \phi_{n'}(\boldsymbol{x})$ to the first equation and the operator $\int_{\mathcal{D}} d\boldsymbol{x}\, \phi_{n'}(\boldsymbol{x})$ to the second equation. By adding the results and using the orthogonality relation, we have

$$(k_m^{(g)})^2 \sum_{m'} I^{(1)}_{n',m'}\, a_{m'} \;+\; k^2 \sum_{m'} I^{(2)}_{n',m'}\, a_{m'} = k_{n'}^2 a_{n'}, \tag{3.53}$$

where

$$\begin{cases} I^{(1)}_{n',m'} \equiv \int_{\text{gain}} d\boldsymbol{x}\, \phi_{n'}(\boldsymbol{x})\, \epsilon(\boldsymbol{x})\, \phi_{m'}(\boldsymbol{x}) \\ I^{(2)}_{n',m'} \equiv \int_{\mathcal{D}} d\boldsymbol{x}\, \phi_{n'}(\boldsymbol{x})\, \epsilon(\boldsymbol{x})\, \phi_{m'}(\boldsymbol{x}) = \delta_{n'm'} - I^{(1)}_{n',m'} \end{cases}. \tag{3.54}$$

Eq. (3.53) can be rewritten as an generalized eigenvalue problem with the introduction of a diagonal matrix $Q = \delta_{nn'} k_{n'}$:

$$\left(Q - k^2 I^{(2)}\right) \mathbf{a} = (k_m^{(g)})^2\, I^{(1)}\, \mathbf{a}. \tag{3.55}$$

The advantage of this approach is that one can obtain N GRCF states and their eigenvalues simultaneously, where N is the number of the original CF states used. If N is not sufficiently large, the eigenvalues near the edges of the frequency window may be not as accurate as the ones in the center. For example, if the gain medium covers 70% of the disk area in a 2D random laser similar to the one studied in Fig. 3.14 and we use 50 CF states as the basis, the absolute values of the off-diagonal elements $L_{i,\,j\neq i}$ in the orthogonality relation (B.5) are in the range $\left[10^{-15}, 10^{-8}\right]$ with an average of 1.6×10^{-10}. This problem can be solved using the second approach below as a complement. It should be noted that if N is too large the calculated GRCF frequencies will scatter all over the complex plane, and some of them may even have a positive imaginary part. A rule of thumb for clearing up the calculated GRCF frequencies is to discard those with a positive imaginary part and whose real part are outside the frequency window containing the original CF states.

The second approach to find the GRCF states is based on the observation that the dielectric function $\epsilon_c(\boldsymbol{x})$ always appears as the pre-factor of the wavevector in the Helmholtz equation. Therefore, we can vary the dielectric constant in $\mathcal{D}$ from its physical value $\epsilon_<$ to ϵ_m such that

$$\epsilon_m = \frac{k^2}{k_m^{(g)2}}\,\epsilon_<. \tag{3.56}$$

What we are doing physically is adding a certain amount of absorption to the index in $\mathcal{D}$ to counteract the unphysical amplification caused by each Im$[k_m]$. Therefore, ϵ_m differs from one GRCF state to another, which can be an inconvenience if we want to obtain many GRCF states at the same time. The implementation of this method involves an iterative process: one first calculate N CF frequencies k_m for a given k, replace $\epsilon_<$ in $\mathcal{D}$ by ϵ_m given by Eq. (3.56), then solve for one CF eigenvalue near the original k_m using ϵ_m (now there are N of them). By repeating this process we find that k_m converge to the desired GRCF frequencies within a few iterations. This method is very efficient if $\mathcal{D}$ covers a small fraction of the disk. For a quadrupole cavity (see Chapter 6) with a deformation of 0.16 and a disk gain region whose radius is 70% the length of the minor axis, it only takes ten iterations for the difference of k_m in two consecutive iterations to fall below 10^{-8}, and the modulus of the off-diagonal elements of the orthogonality relation (B.5) are smaller than 10^{-12}.

In practice it is best to combine these two methods together if we want a relatively large GRCF basis or the gain regions cover only a small part of the whole cavity. In this way we don't need to use as large a CF basis as we do when using the first approach alone, and we can refine each GRCF frequency as much as required using the second approach.

Chapter 4

Solution algorithm of the SALT

Equipped with the methods we introduced in the preceding chapter for calculating CF and GRCF states in various geometries, we now proceed to solve the SALT equations in the CF and GRCF basis (Eq. (2.50) and (2.57)). First we discuss the calculation of the threshold lasing modes defined in Section 2.5.

4.1 Threshold analysis

We introduced the threshold lasing equation (2.59) in Section 2.5, and we mentioned that the threshold lasing mode with the lowest threshold is by definition the first lasing mode when we turn on the pump. The others are not true lasing modes when modal interaction is considered. To find the threshold of each TLM, we can gradually increase D_0 and monitor the distance of each pole of the S-matrix from the real axis as shown in Fig. 2.3. Eq. (2.59) can also be solved in a way similarly to how we solve for the CF states (see Chapter 3). Besides the fact that we are using the gain modified dielectric function $\epsilon(\boldsymbol{x})$ instead of the passive cavity index $\epsilon_c(\boldsymbol{x})$, the only difference is that we are now looking for real eigenvalues k^μ. We first choose an initial guess for each k^μ and solve the linear equation (2.59) which returns a set of complex eigenvalues. We then update each k^μ by the closest one in the complex plane from the previous result and repeat this process until it converges to a real value. A more efficient method to find all the TLMs is solving the expansion of Eq. (2.15) in the CF basis (2.50) without the modal interaction denominator

$(1+\sum_\mu \Gamma_\mu |\Psi_\mu(x)|^2)$:

$$a_m^\mu = -\frac{\gamma_\perp}{(\omega^\mu - \omega_a) + i\gamma_\perp} \frac{k^{\mu 2}}{k^{\mu 2} - k_m^2} \int_{\mathrm{D}} d\boldsymbol{x}' D_0(1 + d_0(\boldsymbol{x}'))\varphi_m(\boldsymbol{x}', \omega^\mu) \sum_p a_p^\mu \, \varphi_p(\boldsymbol{x}', \omega^\mu), \tag{4.1}$$

which determines not only the spatial profiles but also the lasing frequencies of each TLM.

4.1.1 A special case: uniform index cavities with spatially homogeneous gain

The task of finding the thresholds and the corresponding lasing frequencies is particularly simple for the first lasing mode if both $D_0(\boldsymbol{x})$ and $\epsilon_c(\boldsymbol{x})$ are constants inside the cavity. Using the orthogonality relation (2.39) we find all the off-diagonal terms in the integrand vanish, and Eq. (4.1) reduces to the following simple form:

$$a_m^\mu = -\frac{\Xi\gamma_\perp}{(\omega^\mu - \omega_a) + i\gamma_\perp} \frac{k^{\mu 2}}{k^{\mu 2} - k_m^2} a_m^\mu, \tag{4.2}$$

where Ξ is defined as the ratio D_0/ϵ_c. For the mode $\Psi_\mu(\boldsymbol{x})$ this equation must hold for all m's with the same k^μ, which means either all a_m^μ's are zero (the trivial solution) or only one a_m^μ is nonzero, which makes the "single-pole approximation" exact for this nontrivial solution. The latter reiterates the observation that the TLMs are CF states with k_m given by Eq. (2.58) when both $D_0(\boldsymbol{x})$ and $\epsilon_c(\boldsymbol{x})$ are constants. Above threshold however, the "single-pole" picture is only approximate as we will see in later sections. For the nontrivial solution of a_m^μ the coefficient on the *r.h.s.* of Eq. (4.2) must be real and equal to unity. The reality condition determines that the possible lasing frequencies at threshold are

$$\omega_{th}^{(m)} = \omega_a + \frac{\gamma_\perp q_m(\omega_{th}^{(m)})}{\gamma_\perp + \kappa_m(\omega_{th}^{(m)})} \tag{4.3}$$

where $\omega_m - \omega_a \equiv q_m(\omega) - i\kappa_m(\omega)$ (we suppress the index μ here). In deriving Eq. (4.3) we made the approximation $k^{\mu 2} - k_m^2 \sim 2k^\mu(k^\mu - k_m)$ to make the resulting equation more compact, which is not necessary in the actual calculation. Furthermore, the modulus unity condition determines the threshold value of the pump strength:

$$\Xi_{th}^{(m)} = \frac{2\kappa_m}{k^\mu}\left[1 + \frac{q_m^2}{(\gamma_\perp + \kappa_m)^2}\right]. \tag{4.4}$$

The TLM with the lowest threshold will be the first lasing mode. Note that in contrast to the traditional line-pulling formula [55] where the cavity mode frequency is a fixed value, here the single-mode laser frequency is determined by the solution of a self-consistent equation. Nonetheless for high finesse cavities this condition agrees with standard results: the lasing frequency is very close to the cavity resonance nearest to the gain center, pulled towards the gain center by an amount which depends on the relative magnitude of $\gamma_\perp$ vs. κ_m (which is approximately the resonance linewidth).

In fact the discussions in this section doesn't only apply to a cavity with uniform index and gain; Eq. (4.2-4.4) hold as long as $D_0(\boldsymbol{x})/\epsilon_c(\boldsymbol{x})$ is a constant within the cavity. One of such cases is given in the following subsection.

4.1.2 The general case

In the general case where $D_0(\boldsymbol{x})$ and $\epsilon_c(\boldsymbol{x})$ are uncorrelated, the amplitude equation (4.1) is still linear and it can be solved as an eigenvalue problem:

$$\boldsymbol{\mathcal{T}}\boldsymbol{a}^\mu = \lambda^\mu \boldsymbol{a}^\mu. \tag{4.5}$$

$\mathcal{T}_{mn}$ is a linear operator acting on the properly truncated N-dimensional vector space of complex amplitudes $\boldsymbol{a}^\mu = (a_1^\mu, a_2^\mu, \ldots, a_N^\mu)$:

$$\mathcal{T}_{mn}(k) = \Lambda_m(k)\int_{\mathrm{D}} d\boldsymbol{x}'(1 + d_0(\boldsymbol{x}'))\varphi_m(\boldsymbol{x}',\omega)\varphi_n(\boldsymbol{x}',\omega), \tag{4.6}$$

where the pre-factor $\Lambda_m(k)$ is defined as $i\gamma_\perp k^2/[(\gamma_\perp - i(\omega-\omega_a))(k^2 - k_m^2(k))]$. The eigenvalue λ^μ is the inverse threshold D_{th}^μ which is by definition a real quantity. The reality condition cannot in general be satisfied except at discrete values of k. If $D_0(\boldsymbol{x})/\epsilon(\boldsymbol{x})$ is a constant in space, $\mathcal{T}_{mn}$ is diagonal and we recover Eq. (4.2). In general $\mathcal{T}_{mn}$ is non-diagonal and non-hermitian, which has N complex eigenvalues $\lambda_\mu(k)$ for an arbitrary value of k. As

k is varied, the eigenvalues $\lambda_\mu(k)$ flow in the complex plane, each one crossing the positive real axis at a specific k^μ, determined by $\mathrm{Im}[\lambda_\mu(k = k^\mu)] = 0$ (see Fig. 4.1). The modulus of the eigenvalue defines the "non-interacting" lasing threshold corresponding to that eigenvalue, $D^\mu_{th} = 1/\lambda_\mu(k^\mu)$ (these real eigenvalues will be denoted by $\lambda^\mu = \lambda_\mu(k = k^\mu)$), the real wavevector k^μ is the non-interacting lasing frequency, and the eigenvector $\boldsymbol{a}^\mu$ gives the "direction" of the lasing solution in the space of CF states. Among these solutions, the smallest $D^{(1)}_{th}$ (i.e., the largest of the real eigenvalues λ^μ) gives the actual threshold for the first lasing mode; the frequency $k^{(1)}$ is the lasing frequency at threshold and the eigenvector $\boldsymbol{a}^{(1)}$ defines the "direction" of the lasing solution at threshold. The "length" of $\boldsymbol{a}^{(1)}$ cannot be determined from the linear equation (4.5) but rises continuously from zero at threshold and is determined by the non-linear equation (2.50) infinitesimally above threshold. The remaining real eigenvalues of $\boldsymbol{\mathcal{T}}(k)$ define the *non-interacting thresholds* for other modes, and the actual thresholds of all higher modes will differ, often substantially, from their non-interacting values due to the non-linear term in Eq. (2.50).

The condition for having a diagonal threshold matrix is relaxed if we use the GRCF basis, which only requires $D(\boldsymbol{x})/\epsilon(\boldsymbol{x})$ to be a constant inside each gain region. One simple example is given in Section 2.4, and the orthogonality relation (B.5) and the resulting self-consistent equation (2.57) are given in the specific forms assuming constant $D(\boldsymbol{x})$ and $\epsilon(\boldsymbol{x})$ in all the gain regions. From them it is clear that the threshold matrix is indeed diagonal, and the TLMs are the GRCF states themselves. Therefore, we can use Eq. (4.4) and (4.3) to obtain the thresholds and the lasing frequencies for each TLM easily. As a test we calculate the threshold lasing mode with the lowest threshold for the cavity shown in Fig. 3.5 using the CF basis and compare it to the GRCF state whose complex frequency is closest to the gain center. As we can see from Fig. 4.2 the spatial profiles of the GRCF state and that of the superposition of 16 CF states are almost identical . The lasing mode is amplified in the left half of the cavity (where there is gain) and the flux is conserved in the right half. We will also show in Section 4.3 that in this case the sideband ratios in the GRCF basis are much smaller than those in the CF basis in the multi-mode regime. Thus we can truncate the GRCF basis to have just a few states, which makes it a more desirable basis.

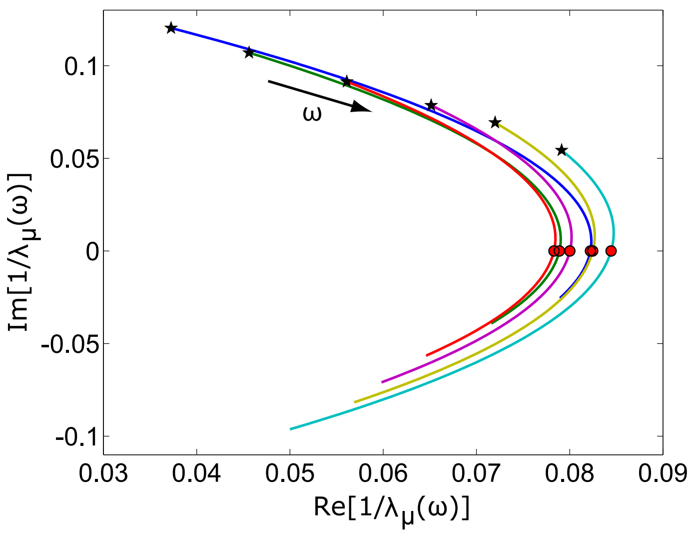

Figure 4.1: Eigenvalue flow for the non-interacting threshold matrix $\boldsymbol{\mathcal{T}}(k)$ in a one-dimensional edge-emitting laser of length $a = 1$ and refractive index $n = 1.5$. Colored lines represent the trajectories in the complex plane of $1/\lambda_\mu(k)$ for a scan $\omega = (\omega_a - \gamma_\perp/2, \omega_a + \gamma_\perp/2)$ $(\omega_a = 30, \gamma_\perp = 1)$. Only a few eigenvalues out of $N = 16$ CF states are shown. The direction of flow as k is increased is indicated by the arrow. Star-shapes mark the initial values of $1/\lambda_\mu(k)$ at $\omega = \omega_a - \gamma_\perp/2$. The full red circles mark the values at which the trajectories intersect the real axis, each at a different value of $k = k^\mu$, defining the non-interacting thresholds D_{th}^μ.

4.2 Interacting threshold matrix

We will discussion the algorithm for solving the full nonlinear equation (2.50) in Section 4.3. An indispensable tool we will need is the interacting threshold matrix to be described below. Suppose that we have solved Eq. (2.50) for a given pump value D_0 above the first threshold and obtained the non-trivial solution $\Psi^1(\boldsymbol{x})$, we need a tool that indicates whether there are new lasing modes at a slightly increased pump $D_0 + \Delta D$. For this purpose we introduce the *interacting threshold matrix*, which is constructed by restoring the modal interaction term in the denominator of Eq. (4.5):

$$\mathcal{T}_{mn}(k) = \Lambda_m(k) \int_{\mathrm{D}} d\boldsymbol{x}' \frac{(1 + d_0(\boldsymbol{x}'))\bar{\varphi}_m^*(\boldsymbol{x}', \omega)\varphi_n(\boldsymbol{x}', \omega)}{\epsilon(\boldsymbol{x}')(1 + \Gamma(k_1)|\Psi_1(\boldsymbol{x}')|^2)} . \tag{4.7}$$

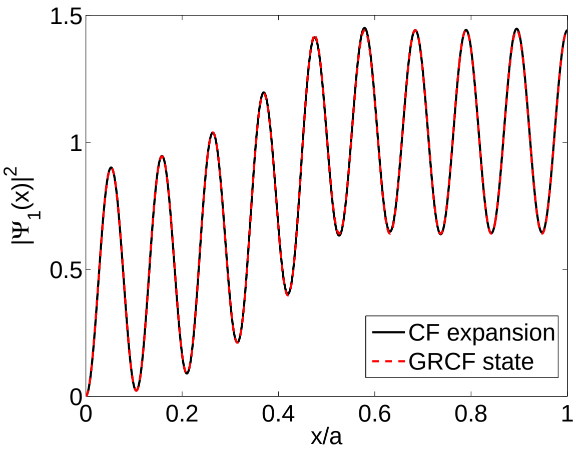

Figure 4.2: Threshold lasing mode with the lowest threshold in a cavity of $n = 1.5$ and $\omega_a = 20$. The left half of the cavity is filled with the gain medium. We include 16 states in the CF basis, and the predicted threshold value $D_{th}^{(1)} = 0.224$ and the corresponding frequency $k^1 = 19.886$ are the same as those of the single GRCF state.

Its largest real eigenvalue at $k^{(1)}$ is the inverse of D_0 at which $\Psi_1(\boldsymbol{x})$ is obtained. Its second largest real eigenvalue at $k^{(2)}$ determines the second interacting threshold, $D_{th}^{(2)}$. This procedure can be generalized as additional modes turn on to define the second, third, etc. interacting threshold matrices. For example, the *pth* interacting threshold matrix has the following form:

$$\mathcal{T}_{mn}(k) = \Lambda_m(k) \int_{\mathrm{D}} d\boldsymbol{x}' \frac{(1 + d_0(\boldsymbol{x}'))\bar{\varphi}_m^*(\boldsymbol{x}', \omega)\varphi_n(\boldsymbol{x}', \omega)}{\epsilon(\boldsymbol{x}')(1 + \Sigma_\nu^p \Gamma(k^\nu)|\Psi_\nu(\boldsymbol{x}')|^2)} \,. \tag{4.8}$$

This procedure gives us a way to monitor when (2.50) has a second, third, etc. non-trivial solution. We diagonalize the matrix (4.7) and plot $D_0\lambda^\mu(D_0)$ as we increase D_0 in small increments solving the non-linear equation (2.50). An example in a simple one-dimensional edge-emitting cavity (see Fig. 3.1) is shown in Fig. 4.3. When $D_0\lambda^\mu(D_0)$ reaches unity, a new mode has reached threshold. One can confirm that the n^{th} threshold matrix has n eigenvalues equal to unity until threshold, when the $(n+1)^{th}$ appears. Such a diagram is appealing because it shows the strong effects of mode competition. The eigenvalues of the non-interacting threshold matrix are fixed numbers $\lambda^\mu = (D_{th}^\mu)^{-1}$, independent of pump, D_0, so that a plot D_0/D^{μ}_{th} vs. D_0 just gives straight lines intersecting unity at the non-interacting thresholds. The interacting threshold matrix depends strongly on D_0, so that the interacting eigenvalues will be sub-linear, leading to much higher thresholds, and some will even be decreasing with increasing D_0, indicating modes which are completely suppressed by mode competition and will never turn on. Thus the interacting threshold matrices give us access to the mode competition *below* threshold, as well as the lasing frequencies below threshold, even though the modal amplitudes are strictly zero below threshold in the semiclassical theory. This is extremely useful when we discuss the properties of random lasers in Chapter 7. Note this information is not obtainable from brute-force simulations and is a major advantage of the SALT.

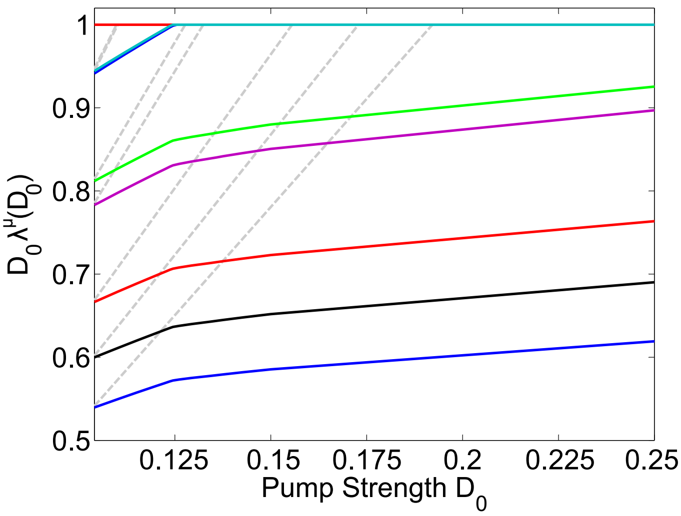

Figure 4.3: Evolution of the thresholds as a function of D_0 for a uniform slab cavity of index $n = 3$. The lasing threshold corresponds to the line $D_0\lambda^{\mu}(D_0) = 1$, so values below that are below threshold at that pump. Once a mode starts to lase its corresponding value $D_0\lambda^{\mu}(D_0)$ is clamped at $D_0\lambda^{\mu} = 1$. The dashed lines represent the linear variation $D_0\lambda^{\mu}(D^{\mu}_{th})$ of the non-interacting thresholds. In this case three modes turn on before D_0 reaches 0.125, and they suppress the higher order modes from lasing even at $D_0 = 0.75$ (not shown).

The information obtained by these successive linearizations of the lasing map (4.8) also facilitate our iteration process of the non-linear problem with a very accurate approximation to the lasing frequencies and the vectors $\boldsymbol{a}^{\mu}$ defining each lasing mode. This allows the iterative solution to converge in a reasonable time.

4.3 Nonlinear solution

The approaches to solve for the non-trivial solutions of the nonlinear equation (2.50) can be roughly put into two categories. Here we first discuss the first one in which we use the existing form of Eq. (2.50) and solve it iteratively.

4.3.1 Iterative method

For a pump strength slightly larger than the first threshold, we choose the lasing wavevector, $k = k_{th}^{(m)}$, calculate the CF basis $\{\varphi_m\}$ corresponding to that choice and then iterate Eq. (2.50) starting from the trial vector $\boldsymbol{a}^\mu(0)$ to yield output $\boldsymbol{a}^\mu(1)$. A natural choice for the initial vector is that of the corresponding threshold lasing mode times a small quantity. As noted, the "lasing map" has the property that below the lasing threshold, D_{th}, the iterated vector, $\mathbf{a}^\mu \to \mathbf{0}$, and above this threshold it converges to a finite value which defines the spatial structure of the lasing mode in terms of the CF states. There is one crucial addition necessary to complete the algorithm. Note that Eq. (2.50) is invariant under multiplication of each $\boldsymbol{a}^\mu$ by a global phase $e^{i\theta}$, so iteration of (2.50) can never determine a unique non-zero solution. Therefore it is necessary to fix the "gauge" of the solution by demanding that we solve (2.50) with the constraint of a certain global phase (typically we take the dominant a_m^μ to be real). Thus after each iteration of (2.50) we must adjust the lasing frequency to restore the phase of a_m; it is just this gauge fixing requirement which causes the lasing frequency to flow from our initial guess to the correct value above threshold. The invariance of (2.50) under global phase changes guarantees that the frequency thus found is independent of the particular gauge choice. Details of how to implement the "gauge condition" can be found in Appendix D. For multi-mode lasing we repeat this procedure for each vector $\boldsymbol{a}^\mu$. In the single-mode regime only one of these vectors will flow to a non-zero fixed point.

This behavior of the multi-mode lasing map is illustrated in Fig. 4.4 for the simple uniform one-dimensional laser illustrated in Fig. 3.1. Below the first threshold, determined from Eq. (4.4) (or (4.5) in general), the entire set of vectors $\boldsymbol{a}^\mu$ flow to zero; above that

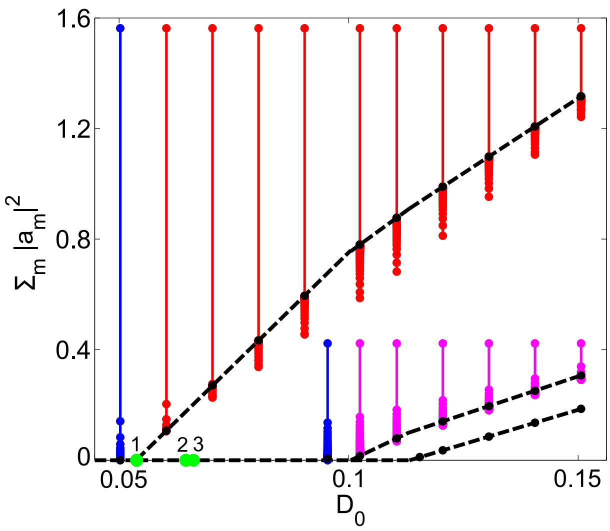

Figure 4.4: Convergence and solution of the multimode lasing map for a one-dimensional edge-emitting laser with $n_1 = 1.5, \omega_a = 19.89$ and $\gamma_\perp = 4.0$ vs. pump D_0. Three modes lase in this range. At threshold they correspond to CF states $m = 8, 9, 10$ with the threshold lasing frequencies $\omega_{th}^{(8)} = 18.08, \omega_{th}^{(9)} = 19.91$, and $\omega_{th}^{(10)} = 21.76$, and the non-interacting thresholds $D_0^{(9)} = 0.054, D_0^{(10)} = 0.065, D_0^{(8)} = 0.066$ (green dots). $\omega_{th}^{(9)} \approx \omega_a$ and $m = 9$ has the lowest threshold. Due to mode competition, modes 2,3 do not lase until much higher values ($D_0 = 0.101, 0.113$). Each mode is represented by an 11 component vector of CF states; we plot the sum of $|a_m|^2$ vs. pump D_0. Below threshold the vectors flows to zero (blue dots). For $D_0 \geq 0.054$ the sum flows (red dots) to a non-zero value (black dashed line), and above $D_0 = 0.101, 0.113$, two additional non-zero vector fixed points (modes) are found (convergence only shown for modes 1,2).

threshold the first lasing mode turns on and its intensity grows linearly with pump strength. Due to its non-linear interaction with other modes, the turn-on of the second and third lasing modes is dramatically suppressed ($\boldsymbol{a}^{\mu>1}$ still flows to zero beyond its non-interacting threshold), leading to a factor of four increase in the interval of single-mode operation. The actual lasing frequencies of higher modes have a relatively weak dependence on D_0 and differ little from their values given by Eq. (4.3) in the absence of modal interaction. The modal intensity shows slope discontinuities at higher thresholds as seen in normal laser operation.

We expect the lasing mode to involve several CF states and differ most from a single cavity resonance for a low finesse cavity; thus we consider relatively small index, $n_0 = 1.5$.

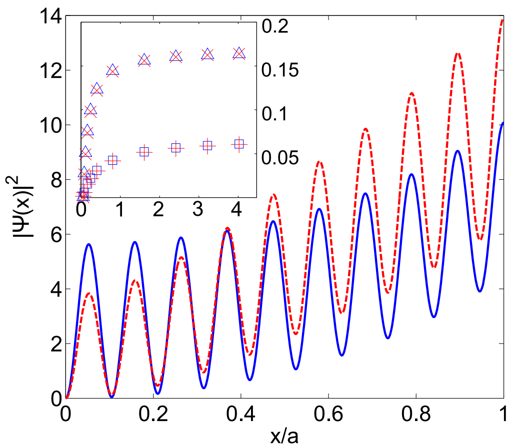

Figure 4.5: Non-linear electric field intensity for a single-mode edge-emitting laser with $n = 1.5, \omega_a = 19.89, \gamma_\perp = 0.5, D_0 = 0.4$. The full field (red line) has an appreciably larger amplitude at the output $x = a$ than the "single-pole" approximation (blue) which neglects the sideband CF components. Inset: The ratio of the two largest CF sideband components to that of the central pole for $n_0 = 1.5$ ($\triangle$, $\times$) and $n_0 = 3$ ($\square$,+) vs. pump strength D_0.

The actual lasing mode will be the sum of several of these CF modes with different spatial frequencies and amplification rates. In Fig. 4.5 we plot such a mode. Standard modal expansions in laser theory are equivalent to choosing only the central CF state and missing the contribution of these spatial "side-bands". The inset to Fig. 4.5 shows that near threshold only one CF state dominates (one can show that the other components are of order the cube of the dominant component). But well above threshold the two nearest neighbor CF states are each 15% of the main component and since one of these has higher amplification rate, the final effect is to increase the output power by more than 43% (see Fig. 4.5). The sidebands are still 6% of the dominant component when the index is increased to $n_0 = 3$, leading to an increase in output power by 26% (see inset, Fig. 4.5).

The iterative algorithm of solving Eq. (2.50) using the GRCF states is essentially the same. For the case shown in Fig. 4.2, we increase the pump strength to reach the two-mode regime ($D_0 = 250$) and excellent agreement is found between the results given by using the CF basis and the GRCF basis. In the CF basis the largest normalized expansion coefficients ξ^μ ($\xi^\mu \equiv |a^\mu|_{max}/\sum_i |a_i^\mu|$) for these two modes are 0.68 and 0.66, while in the

GRCF basis they both are 0.91. A larger ξ^μ means the μth mode can be characterized better by a single basis function and a smaller basis is needed to meet the convergence criterion. In more complex geometries where the density of CF states is larger or the gain structure is more complex, the lasing modes are well spread out in the CF basis and we benefit from using the GRCF basis.

There are two important things to keep in mind when a higher order mode $\Psi^\nu(\boldsymbol{x})$ is expected to turn on at a given pump $D_0+\Delta D$. First, we need to know in advance which CF state is the largest component for the new mode. This information can be obtained from the eigenvector of the interacting threshold matrix associating with the smallest inverse eigenvalue $(\lambda^\mu)^{-1}$ above D_0. Suppose ϕ_{m_ν} is the most important CF state of $\Psi^\nu(\boldsymbol{x})$, but somehow we choose the wrong one $\phi_{m'}$ to impose the gauge condition. The vector $\boldsymbol{a}^\nu$ will flow to that of another mode in which $\phi_{m'}$ has the largest weight. If the other mode is not already lasing, then it is mostly likely that the iteration will give us a trivial zero solution for the higher order mode unless ΔD is large, which should be avoided in the first place. In fact, this could also happen if we chose the right CF state but an inappropriate overall scale for the initial guess of $\boldsymbol{a}^\nu$. It then brings us to the second important point: checking the eigenvalues of the interacting threshold matrix to see whether a trivial zero solution is what one should get for that mode. If indeed the mode is below threshold, all $D_0\lambda^\mu(D_0)$ should be equal to or less than 1; If there is one or more $\lambda^\mu(D_0) > 1/D_0$, we know that there is at least one nontrivial solution that we fail to find. We then need to check whether we have a wrong implementation of the gauge condition or an inappropriate initial guess for $|\boldsymbol{a}^\nu|$.

4.3.2 Using standard nonlinear system solvers

For lasers with strong modal interactions, the iterative approach described above sometimes fails to converge and we need a more robust numerical method. Instead of writing it ourselves, we decide to utilize numerical packages that are readily available. To implement the nonlinear SALT solver in MatLab, we adopt the sophisticated function *fsolve* which solves systems of nonlinear equations. We first formulate Eq. (2.50) into a square system and tell *fsolve* which quantities it needs to solve for. Suppose for a given pump value D_0

we expect there are Q lasing modes and the CF basis is truncated to have N states, then there are $(2N+1)Q$ unknown real quantities we need to solve for: Q lasing frequencies, and the real and imaginary parts of $N \times Q$ CF expansion coefficients. Eq. (2.50) gives us a total of $(2N \times Q)$ real equations, and the missing Q equations are the Q "gauge" conditions. To implement the "gauge" condition explicitly, we demand that the dominant a_m^μ in each of the Q modes is real. Therefore, the $(2N \times Q)$ equations from Eq. (2.50) are sufficient and necessary to solve for the $(2N \times Q)$ unknowns. When ordering the argument list, we put the lasing frequency k^μ in the position of the eliminated imaginary part of the dominant a_m^μ for convenience.

When solving the self-consistent equation (2.50) using the second approach we frequently find that some modes are more likely to converge to the trivial zero solutions instead of the non-trivial ones. To solve this problem, we divide each $\boldsymbol{a}^\mu$ by its dominant component $a_{m_\mu}^\mu$ (which we choose to be real) and rewrite Eq. (2.50) in the following way:

$$b_m^\mu = -\frac{\gamma_\perp}{(\omega^\mu - \omega_a) + i\gamma_\perp} \frac{k^{\mu 2}}{k^{\mu 2} - k_m^2} \int_{\mathrm{D}} d\boldsymbol{x}' \frac{D_0(1 + d_0(\boldsymbol{x}'))\varphi_m(\boldsymbol{x}', \omega^\mu) \sum_p b_p^\mu \varphi_p(\boldsymbol{x}', \omega^\mu)}{1 + \sum_\nu (a_{m_\nu}^\nu)^2 \Gamma_\nu \left| \sum_p b_p^\nu \varphi_p(\boldsymbol{x}', \omega^\nu) \right|^2}. \tag{4.9}$$

b_m^μ is the complex quantity $a_m^\mu / a_{m_\mu}^\mu$ with the exception $b_{m_\mu}^\mu = 1$, and the new $2N$ unknown real quantities for each mode are the real and imaginary parts of $b_{m \neq m_\mu}^\mu$ ($2(N-1)$ in total), the real dominant CF coefficient $a_{m_\mu}^\mu$ and the lasing frequency k^μ. It is easy to check that $b_{m \neq m_\mu}^\mu = a_{m_\mu}^\mu = 0$ is not a solution of the equation above, and we eliminate the trivial zero solutions of the original self-consistent equation (2.50). When using this method we need to be completely sure that all the modes included in the nonlinear calculation should give non-trivial $\boldsymbol{a}^\mu$. Otherwise the nonlinear solver won't be able to find any solution. Thanks to the interacting threshold matrix, we only need to consider this problem when D_0 is close to the threshold of a higher order mode. In this case we linearize the curve $D_0 \lambda^\mu(D_0)$ and find the value D_0^{th} where it becomes unity. We then increase D_0 by small amounts in the vicinity of D_0^{th} while keeping the number of lasing modes included in the nonlinear calculation the same. The D_0 value at which $D_0 \lambda^\mu(D_0)$ first becomes greater than unity is slightly larger the true threshold of the higher order mode, and we can safely include the new mode in the multi-mode calculation beyond that pump value.

4.4 Summary of algorithm

To summarize our solution procedure for (2.50) in the general case where $D(\boldsymbol{x})$ the inhomogeneous: the inputs are the dielectric function of the resonator, $\epsilon(\boldsymbol{x})$, the atomic frequency, ω_a and gain width $\gamma_\perp$.

- The CF states φ_m and wavevectors k_m are found for a range of k values near ω_a by solving the linear non-hermitian differential equation (2.33).
- The non-interacting threshold matrix $\boldsymbol{\mathcal{T}}(k)$ is constructed from the CF states (and their adjoint partners) and frequencies following (4.5). k is varied and the largest real eigenvalue of $\boldsymbol{\mathcal{T}}(k)$ is found at $k = k_1$; this defines the first threshold and k_1 is the corresponding lasing frequency; the corresponding eigenvector gives the trial solution just above threshold, the overall amplitude of which is to be determined by the non-linear equation (2.50).
- The pump D_0 is increased in small steps and the solution from the previous step is used as the trial solution for the next step to solve the non-linear equation (2.50) efficiently by iteration. The lasing frequencies are allowed to flow to maintain the gauge condition as discussed above.
- The solution for the non-linear equation with n lasing modes is used to construct the interacting threshold matrix, $\boldsymbol{\mathcal{T}}(k)$, which is continuously monitored for the appearance of an additional eigenvalue $D_0\lambda^\mu(D_0) = 1$, signaling the threshold for mode $(n+1)$, and the need to increase the number of solutions to the non-linear equation (2.50).

The flow chart of the above steps is illustrated in Fig. 4.6. Codes based on this algorithmic structure have been developed successfully for arbitrary 1D cavities, for 2D uniform dielectric cavities of general shape (see Chapter 6), and for 2D disordered cavities embedded in a disk-shaped gain medium (see Chapter 7).

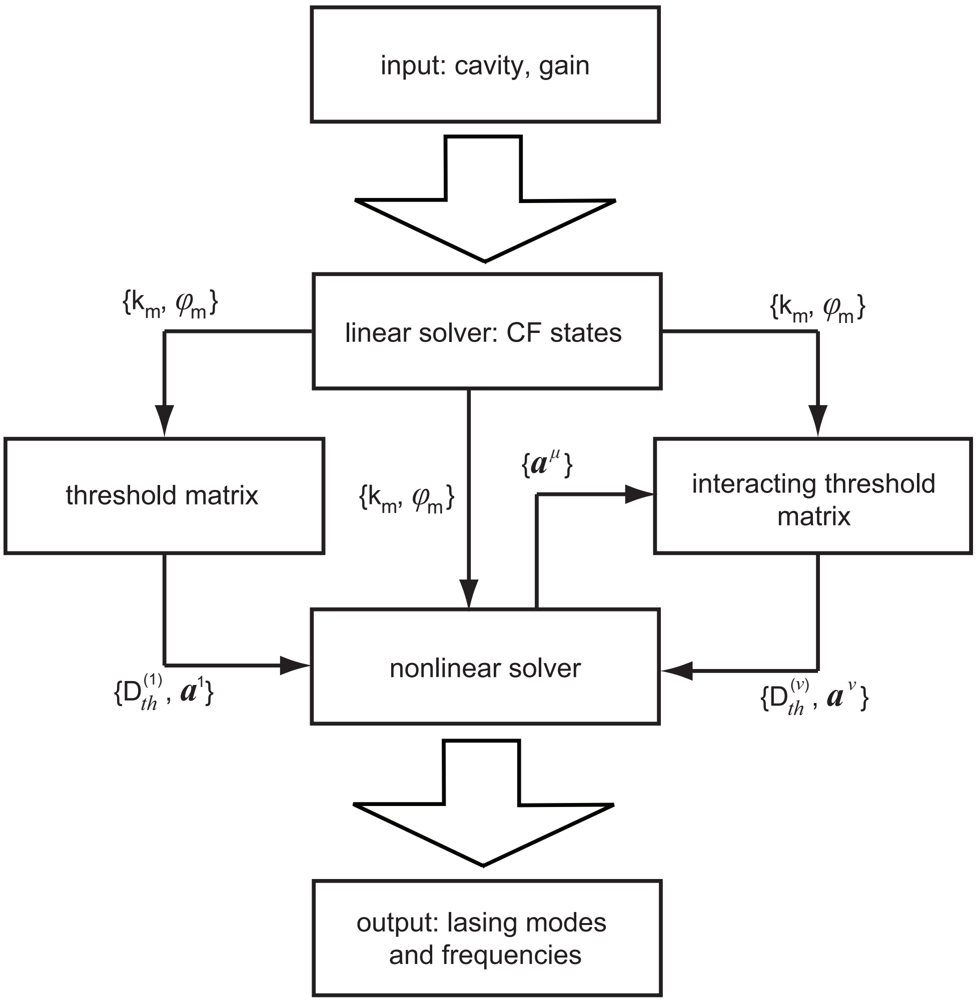

Figure 4.6: Algorithmic structure of the implementation of the SALT.

Chapter 5

Quantitative verification of the SALT

In this chapter we compare the numerical simulations of the Maxwell-Bloch (MB) equations (with no approximation) with the SALT presented in this thesis. We found the agreement to be very good in the regime where the stationary inversion approximation is valid. As discussed in Section 2.1 the stationary inversion approximation is good when the two criteria $\gamma_{\|}/\Delta\omega_{\mu\nu} \ll 1$ and $\gamma_{\perp}/\gamma_{\|} \ll 1$ are meet. In Section 5.2 we derive the perturbation corrections to the SALT in terms of the these two small quantities.

5.1 Comparison with numerical simulations

To perform a well-controlled comparison of MB simulation and SALT results we chose to study the simple one-dimensional edge-emitting laser shown in Fig. 3.1. The MB equations are simulated in time and space using a finite-difference-time-domain (FDTD) approach for the Maxwell equations, while the Bloch equations are discretized using a Crank-Nicholson scheme. To avoid solving a nonlinear system of equations at each spatial location and time step, we adopt the method proposed by Bidégaray [86], in which the polarization and inversion are spatially aligned with the electric field, but are computed at staggered times, along with the magnetic field. Modal intensities are computed by a Fourier transform of the electric field at the boundary after the simulation has reached the steady state. The numerical integration of the MB equation was done by another graduate student Robert J. Tandy in Prof. A. Douglas Stone's group.

When comparing the modal intensities given by the numerical simulation to the results calculated from the theory presented in Refs. [52, 66] (the SALT with the slowly-varying envelope approximation), we find systematic deviations, as one can see in Fig. 5.1. Besides numerical errors that might be introduced in the simulation, two possible factors could have led to these differences: the stationary inversion approximation and the slowly-varying envelope approximation used in the steady-state theory. We have ruled out the rotating-wave approximation since all the lasing frequencies in our current investigation are in the vicinity of ω_a, and the second-order harmonic terms can be safely dropped. When analyze the Fourier spectrum of the inversion in steady state, we find a sharp peak at the zero frequency in the spectrum with minute sidebands. This indicates that the SIA is almost exact in the case under study. Therefore, we conclude that the discrepancy of these two approaches is most likely due to the SVEA. This prompts us to remove the SVEA in the steady-state theory, which leads to the formulation of SALT introduced in Chapter 2.

In Figs. 5.1a, 5.1b we show modal intensities and frequencies in two cavities with $n = 1.5$ and 3, finding remarkable agreement between MB and SALT approaches with no fitting parameters for the case of three mode and four mode lasing respectively. Both thresholds, modal intensities and frequencies are found correctly by the SALT approach. Note that all of these quantities are direct outputs of the SALT, whereas they must be found by numerical Fourier analysis of the MB outputs, which can introduce some additional numerical error. If the SALT approach is used *with* the SVEA then significant discrepancies are found, for example for $n_0 = 3$ the threshold of the third mode is found to be higher than from MB while the fourth threshold is too low. Note however that the theory with the SVEA does get the right number of modes and the correct linear behavior for large pump values, and we believe that it *does* solve very accurately the SVEA-based Schrödinger-Bloch equations [87].

Almost all studies of the MB equations in the multimode regime have used the approximation of treating the non-linear modal interactions to third-order (near threshold approximation) and in fact this approximation is used quite generally and uncritically

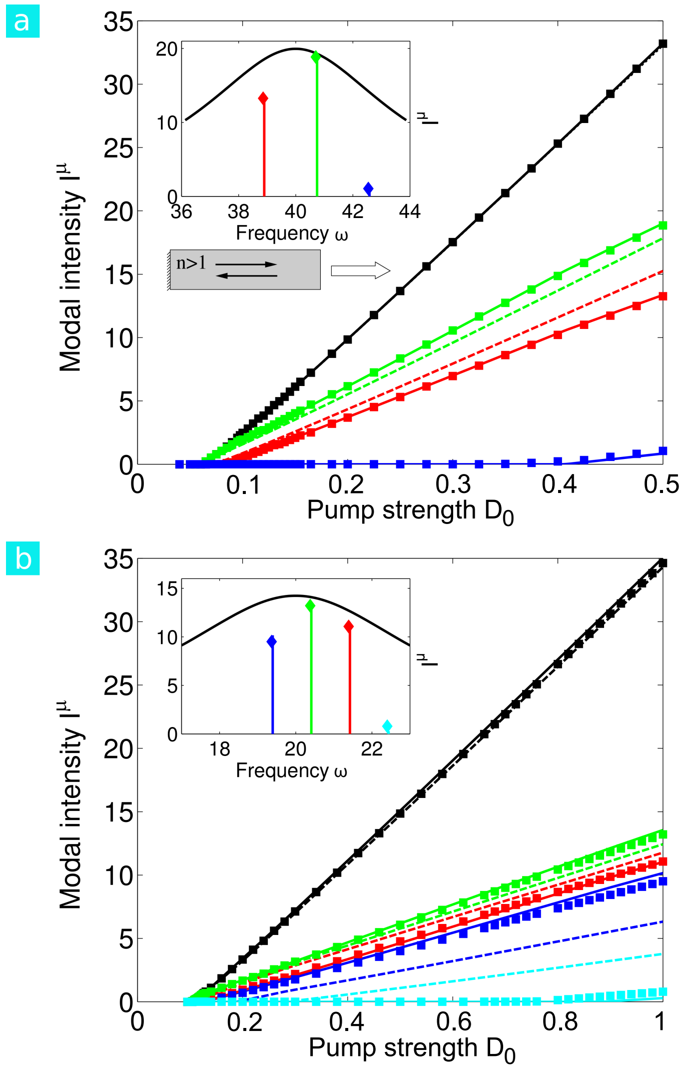

Figure 5.1: Modal intensities as functions of the pump strength D_0 in a one-dimensional microcavity edge emitting laser of $\gamma_\perp = 4.0$ and $\gamma_\| = 0.001$. (a) $n = 1.5$, $k_a L = 40$. (b) $n = 3$, $k_a L = 20$. Square data points are the result of MB time-dependent simulations; solid lines are the result of steady-state ab-initio calculations (SALT) of Eq. (2.19). Excellent agreement is found with no fitting parameter. Colored lines represent individual modal output intensities; the black lines the total output intensity. Dashed lines are results of SALT calculations when the slowly-varying envelope approximation is made as in Ref. [66] showing significant quantitative discrepancies. For example, in the $n = 3$ case the differences of the third/fourth thresholds between the MB and SALT approaches are 46% / 63%, respectively, but are reduced to 3% and 15% once the SVEA is removed. The spectra at the peak intensity and the gain curve are shown as insets in (a) and (b) with the solid lines representing the predictions of the SALT (Eq. (2.19)) and with the diamonds illustrating the height and frequency of each lasing peak. The schematic in (a) shows a uniform dielectric cavity with a perfect mirror on the left and a dielectric-air interface on the right.

throughout laser theory. From examination of the form of the SALT equations (2.15) and (2.19) it is clear that the non-linear interactions are treated to all orders, while the third order treatment would arise from expanding the denominator to the leading order in $|\Psi_\nu|^2$. This third-order version of the SALT then becomes similar to standard treatments of Haken [61, 60], with the improvement of correctly treating the openness of the cavity and the self-consistency of the lasing modes in space [66, 52]. An early version of this improved third order theory was found to have major deficiencies: it predicted too many lasing modes and the intensities did not scale linearly at large pump, but exhibited a spurious saturation [52, 88]. In Fig. 5.2 we present comparisons of the third order approximation to Eq. (2.19), which is improved over Ref. [52] because it drops the SVEA and the "single-pole approximation" used there. We find that this improved third order theory still does a very poor job of reproducing the multimode MB results: it still predicts too many modes (in this case seven, when there should only be four at $D_0 = 1$ in Fig. 5.2), and shows the same spurious saturation as found earlier [52] because the third-order approximation cannot give the correct linear behavior for large pump values. The infinite order treatment of Eq. (2.19) is both qualitatively and quantitatively essential.

5.2 Perturbative correction to the stationary inversion approximation

The central approximation required for Eq. (2.19) is that of stationary inversion. Previous work by Fu and Haken [60] argued that SIA holds for the MB equations when $\gamma_\parallel \ll \gamma_\perp, \Delta$, where $\gamma_\parallel$ is the relaxation rate of the inversion and Δ is the frequency difference of lasing modes. For a typical semiconductor laser $\gamma_\perp \simeq 10^{12} - 10^{13} s^{-1}$ and $\gamma_\parallel \simeq 10^8 - 10^9 s^{-1}$, or equivalently $\gamma_\parallel/\gamma_\perp \simeq 10^{-3} - 10^{-5}$. For the microcavity edge-emitting laser we are modeling we took $\gamma_\perp, \Delta \sim 1$ and $\gamma_\parallel = 10^{-3}$, and we found the excellent agreement shown in Figs. 1a, 1b. In addition, direct analyses of the inversion vs. time obtained from the MB simulations confirm very weak time-dependence in the steady state, justifying the use of SIA. The previous work did not develop a systematic theory in which $\gamma_\parallel/\gamma_\perp, \gamma_\parallel/\Delta$ appear as small parameters in the lasing equations, allowing perturbative treatment of corrections

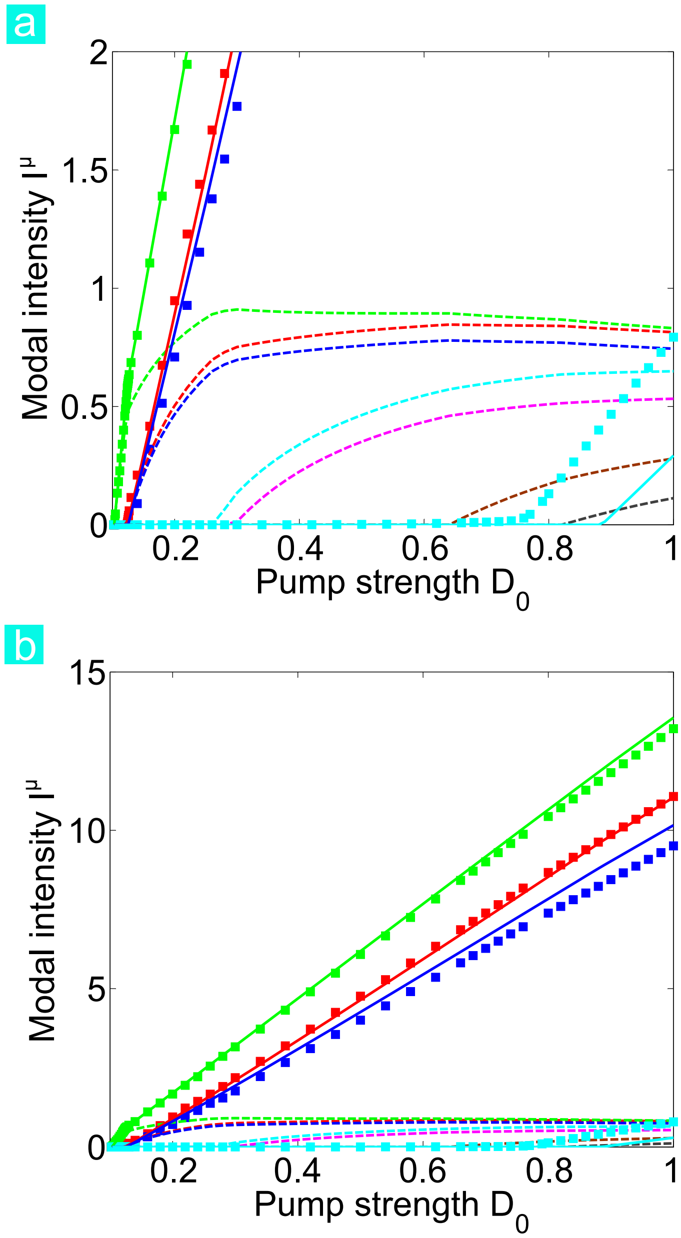

Figure 5.2: (a) Modal intensities as functions of the pump strength D_0 in a one-dimensional edge-emitting laser of $n = 3$,$k_a L = 20$, $\gamma_\perp = 4.0$ and $\gamma_\| = 0.001$; the solid lines and data points are the same as in Fig. 1b. The dashed lines are the results of the third order approximation to Eq. (2.19). The frequently used third order approximation is seen to fail badly at a pump level roughly twice the first threshold value, exhibiting a spurious saturation not present in the actual MB solutions or the SALT. In addition, the third order approximation predicts too many lasing modes at larger pump strength. For example, it predicts seven lasing modes at $D_0 = 1$, while both the MB and SALT show only four. (b) The same data as in (a) but on a larger vertical scale.

to the SIA; we are now able to do this within the SALT formalism.

Note first that in Eq. (2.19) the electric field is measured in units $e_c \sim \sqrt{\gamma_\parallel}$ but, unlike $\gamma_\perp$, $\gamma_\parallel$ does not appear explicitly. Hence the solutions of Eq. (2.19) depend on $\gamma_\parallel$ only through this scale factor, and Eq. (2.19) makes the strong prediction of a universal overall scaling of the field intensities: $|E(x)|^2 \sim \gamma_\parallel$ when dimensions are restored. The perturbative corrections to Eq. (2.19) are obtained by including the leading effects of the beating terms between the different lasing modes which lead to time-dependence of the inversion at multiples of the beat frequencies. These population oscillations non-linearly mix with the electric field and polarization to generate all harmonics of the beat frequencies in principle, but the multimode approximation assumes all the newly generated Fourier components of the fields are negligible. The leading correction to this approximation is to evaluate the effect of the lowest sidebands of population oscillation on the polarization at the lasing frequencies and on the static part of the inversion, both of which will enter Eq. (2.19). For simplicity we present a sketch of the correction to Eq. (2.19) in the two-mode regime where there is a lasing mode on each side of the lasing transition frequency ω_a, and the result in multi-mode cases can be obtained similarly. We assume the electric field and the polarization can still be written in the multi-periodic forms (Eq. (2.10)), and keep the lowest non-zero frequencies ($\pm(\omega_1 - \omega_2)$) terms in the coupling term in Eq. (2.3). The resulting equation can be separated into two equations, the first of which is the one we used to derived the stationary inversion Eq. (2.13):

$$0 = \gamma_\parallel(D_0(\boldsymbol{x}) - D_s(\boldsymbol{x})) - \frac{2}{i\hbar}(\Psi_1(\boldsymbol{x})p_1^*(\boldsymbol{x}) + \Psi_2(\boldsymbol{x})p_2^*(\boldsymbol{x}) - c.c.) \tag{5.1}$$

We put the subscript, s, on the inversion $D_s(\boldsymbol{x})$ to distinguish it from the total inversion $D(\boldsymbol{x}, t)$. The second equation can be written as

$$\dot{D}_\Delta(\boldsymbol{x}, t) = -\gamma_\parallel D_\Delta(\boldsymbol{x}, t) - \frac{2}{i\hbar}\left\{[\Psi_1(\boldsymbol{x})p_2^*(\boldsymbol{x}) - \Psi_2^*(\boldsymbol{x})p_1(\boldsymbol{x})]e^{-i(\omega_1-\omega_2)t}\right\}, \tag{5.2}$$

and $D_\Delta(\boldsymbol{x}, t)$ oscillates at the frequency equal to the difference of the two lasing frequency. The total inversion is given by $D(\boldsymbol{x}, t) = D_s(\boldsymbol{x}) + (D_\Delta(\boldsymbol{x}, t) + c.c.)$. Although we start by assuming that E and P only have two frequencies, the coupling of E and the two time-dependent inversion terms in Eq. (2.8) will lead to components of frequency $\pm(2\omega_1 - \omega_2)$ and $\pm(2\omega_2 - \omega_1)$ in P. Here we drop these terms since they are further away from the transition frequency. The polarization oscillating at ω_1 has two sources. One is the driving electric field at frequency ω_1, and the other is the coupling of the electric field oscillating at ω_2 and the inversion beating at $(\omega_1 - \omega_2)$:

$$\dot{p}_1 = -(i(\omega_a - \omega_1) + \gamma_\perp)p_1 + \frac{g^2}{i\hbar}(\Psi_1 D_s + \Psi_2 d_\Delta), \tag{5.3}$$

in which $d_\Delta(\boldsymbol{x})$ is the time-independent amplitude of $D_\Delta(\boldsymbol{x}, t)$ ($D_\Delta(\boldsymbol{x}, t) = d_\Delta(\boldsymbol{x})e^{-i(\omega_1-\omega_2)t}$). A similar equation can be written for p_2 with the subscripts 1,2 exchanged and $d_\Delta(\boldsymbol{x}) \to d^*_\Delta(\boldsymbol{x})$ in Eq. (5.3).

For the zeroth order expansion, we neglect D_Δ and recover the stationary inversion $D^{(0)}(\boldsymbol{x}, t) = D_s(\boldsymbol{x})$ and the zeroth order polarization

$$p^{(0)}_\mu(\boldsymbol{x}) = \frac{g^2}{i\hbar}\frac{D_s(\boldsymbol{x})\Psi_\mu(\boldsymbol{x})}{\gamma_\perp - i(\omega_\mu - \omega_a)}. \tag{5.4}$$

By inserting $p^{(0)}_\mu(\boldsymbol{x})$ into Eq. (5.2), we obtain the fist order correction to $D(\boldsymbol{x}, t)$, a non-zero $d_\Delta(x)$:

$$\begin{aligned} d_\Delta(x) &= \frac{\gamma_\parallel}{i(\omega_1 - \omega_2) - \gamma_\parallel}\frac{\gamma_\perp^2 - i\gamma_\perp(\omega_1 - \omega_2)/2}{\gamma_\perp^2 + (\omega_1 - \omega_a)(\omega_2 - \omega_a) - i\gamma_\perp(\omega_1 - \omega_2)}\frac{D_s\Psi_1(x)\Psi_2^*(x)}{e_c^2} \\ &\equiv f_n(\omega_1, \omega_2)\frac{D_s\Psi_1(x)\Psi_2^*(x)}{e_c^2}. \end{aligned} \tag{5.5}$$

Here the dimensionless quantity $f_n(\omega_1, \omega_2)$ can be thought as a correlation function between the lasing frequencies. It has the property that $f_n(\omega_2, \omega_1) = (f_n(\omega_1, \omega_2))^*$, and its modulus is peaked at $\omega_1 = \omega_2$. When $\Delta \equiv \omega_1 - \omega_2$ is of the same order as $\gamma_\perp$, the modulus of f_n is largely determined by the ratio $\gamma_\parallel/\Delta$. When this ratio is small, f_n and d_Δ are negligible and we recover the results with the SIA. As the ratio increases, f_n becomes more important and we need to consider its correction to the polarization

$$p^{(1)}_1(\boldsymbol{x}) = \frac{g^2}{i\hbar}\frac{1 + f_n(\omega_1, \omega_2)|\Psi_2(\boldsymbol{x})|^2}{\gamma_\perp - i(\omega_1 - \omega_a)}D_s(\boldsymbol{x})\Psi_1(\boldsymbol{x}). \tag{5.6}$$

$p_2^{(1)}(\boldsymbol{x})$ satisfies the same equation with the subscripts 1 and 2 interchanged. So far we have used $D_s(\boldsymbol{x})$ as a known quantity without specifying its actual form. By replacing the polarization by $p_\mu^{(1)}(\boldsymbol{x})$ in Eq. (5.1), we have

$$D_s^{(1)}(\boldsymbol{x}) = \frac{D_0(x)}{1+\sum_\nu \Gamma_\nu |\Psi_\nu(\boldsymbol{x}')|^2 + f_d(\omega_1,\omega_2)|\Psi_1(\boldsymbol{x}')\Psi_2(\boldsymbol{x}')|^2}, \tag{5.7}$$

and the coefficient f_d of the interference term is a real function of the lasing frequencies

$$f_d(\omega_1,\omega_2) = \frac{\gamma_\parallel}{\gamma_\perp}\frac{(2+\sum_{\nu=1}^2 w_\nu^2)(1-w_1w_2)}{\prod_{\nu=1}^2(1+w_\nu^2)^2} \tag{5.8}$$

where w_ν is the shorthand notation for the dimensionless quantity $(\omega_\nu-\omega_a)/\gamma_\perp$. Notice $D_s^1(\boldsymbol{x})$ differs from the zeroth order result by having a new term proportional to $|\Psi_1(x)\Psi_2(x)|^2$ in the denominator, and its prefactor $f_d(\omega_1,\omega_2)$ is explicitly proportional to the second small parameter $\gamma_\parallel/\gamma_\perp$ and symmetric in its two arguments. The full correction to the non-linear polarization in Eq. (5.6) is obtained by replacing $D_s^{(0)}$ with $D_s^{(1)}$, which leads to the corrected version of Eq. (2.19) of the SALT:

$$\Psi_2(\boldsymbol{x}) = \frac{i\gamma_\perp D_0\omega_2^2}{\gamma_\perp - i(\omega_2-\omega_a)}\int d\boldsymbol{x}'\frac{(1+f_n(\omega_1,\omega_2)|\Psi_1(\boldsymbol{x}')|^2)\,G(\boldsymbol{x},\boldsymbol{x}';\omega_2)\Psi_2(\boldsymbol{x}')}{(1+\sum_\nu \Gamma_\nu|\Psi_\nu(\boldsymbol{x}')|^2+f_d(\omega_1,\omega_2)|\Psi_1(\boldsymbol{x}')\Psi_2(\boldsymbol{x}')|^2)}, \tag{5.9}$$

in which we have restored the natural units of the the electric field. $\Psi_1(\boldsymbol{x})$ satisfies the same equation with the subscripts 1 and 2 interchanged.

Eq. (5.9) predicts corrections to the universal behavior of the threshold and modal intensities we mentioned before, with the exception of the value of the first threshold and the intensity of the first lasing mode before the second threshold. This is because the correction terms to $\Psi_1(\boldsymbol{x})$ all vanish below the second threshold (there needs to be two modes to have beats). However, the theory predicts a non-trivial correction to the threshold of the second mode. Note that the correction to $\Psi_2(\boldsymbol{x})$ (Eq. (5.9)) in the numerator does not vanish below the second threshold but contributes self-consistently to that threshold. This correction can be regarded as modifying the dielectric function of the microcavity to take the form $\epsilon'(\boldsymbol{x}) = \epsilon(\boldsymbol{x})/[1+\frac{\gamma_\parallel}{\Delta}f_n(\omega_2,\omega_1)|\Psi_1(\boldsymbol{x})|^2]$; the effective dielectric function then becomes complex and varying in space according to the intensity of the first mode.

This in turn changes the threshold for the second mode. If the modes are on opposite sides of the atomic frequency as we assumed and $\omega_2 < \omega_1$, the imaginary part of the effective index is always amplifying and tends to decrease the second threshold; we find this effect dominates over the change in the real part and increasing $\gamma_{\|}$ uniformly decreases the thresholds. The opposite effect is possible and observed in other cases we have studied (not shown). In Fig. 5.3 we show the results of MB simulations as $\gamma_{\|}$ is varied from 0.001 to 0.1 (with $\gamma_{\perp} = 4$). Note that the universal behavior (in units scaled by $\gamma_{\|}$) is well obeyed until $\gamma_{\|} = 0.1$, encompassing most lasers of interest. The qualitative effect predicted by the perturbation theory is clearly seen, the higher thresholds are reduced as $\gamma_{\|}$ is increased. The effect is small for the 2nd threshold but large for the third as we expect as the corrections scale with the product of the intensities of lower modes. Fig. 5.3(b) shows that the perturbation theory for the third threshold (a suitable generalization of the two-mode Eq. (5.9)) yields semi-quantitative agreement with the threshold shifts found from the simulations. Note that the simulations also find additional modes turning on for $\gamma_{\|} = 0.1$ but their intensities are very small and they are not shown in Fig. 5.3.

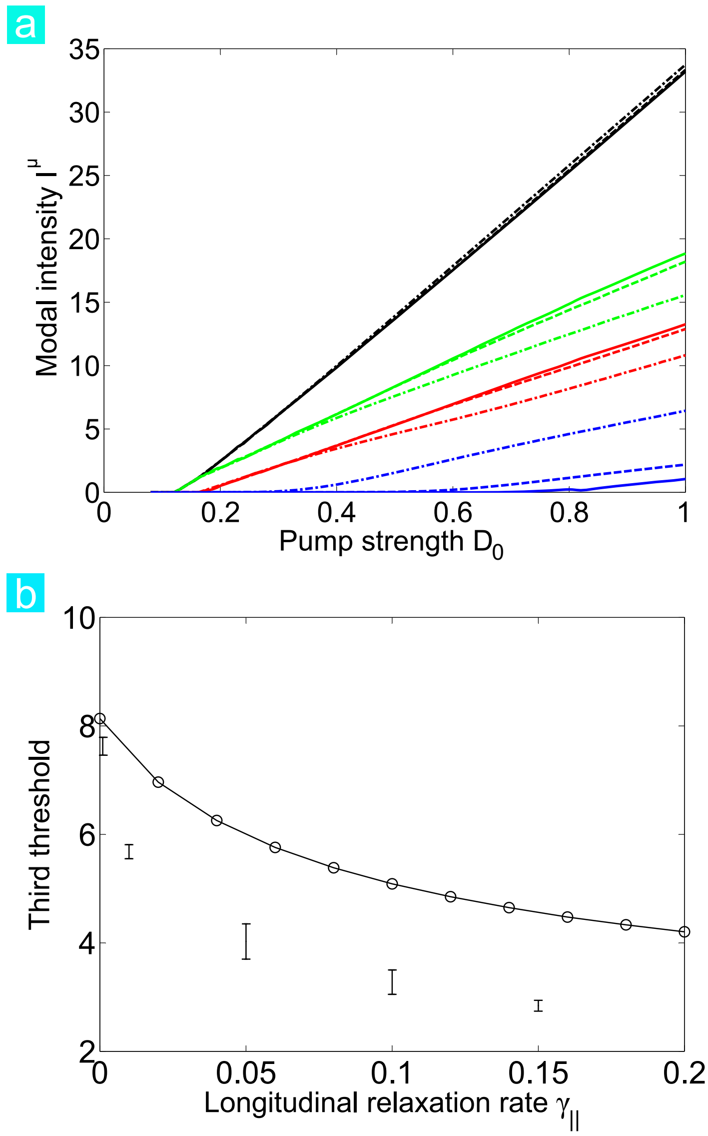

Figure 5.3: (a) Modal intensities for the microcavity edge emitting laser of Fig. 3.1 as $\gamma_{||}$ is varied ($n = 1.5$, $k_aL = 20$, $\gamma_\perp = 4.0$ and mode-spacing $\Delta \approx 1.8$. Solid lines are SALT results from Fig. 5.1(a) (with $\gamma_{||} = 0.001$); dashed lines are $\gamma_{||} = 0.01$ and dot-dashed are $\gamma_{||} = 0.1$. The color scheme is the same as in Fig. 5.1(a). (b) Shifts of the third threshold as a function of $\gamma_{||}$. The perturbation theory (circles, with the line to guide the eyes) predicts semi-quantitatively the decrease of the threshold as $\gamma_{||}$ increases found in the MB simulations. The MB threshold is not sharp and we add an error bar to denote the size of the transition region.

Chapter 6

ARC lasers

ARC lasers have smooth boundaries deformed from a circle; the most well studied shapes include the quadrupole [28, 89, 90, 91, 92] and the limacon [15, 93, 94]. The boundary of the quadrupole is described by $R(\phi) = R_0[1 + \epsilon \cos(2\phi)]$, where ϕ is the polar angle and R_0 is the average radius. The limacon has a similar boundary with $\cos(2\phi)$ replaced by $\cos(\phi)$, thus it only has one symmetry axis along the $\phi = 0$ direction. In Ref. [14] a series of quadrupole-shaped quantum cascade lasers (QCLs) with ϵ varying from 0 to 0.2 were fabricated, and it was found that the peak output intensity of the laser increases rapidly with the deformation. Meanwhile, the inplane directionality of the output beams change from isotropic to four narrow peaks in the $\phi = (j/2 + 1/4)\pi\,(j = 0, 1, 2, 3)$ directions. The special emission pattern was attributed to the second order bow-tie modes [14] (see Fig. 6.2), but it was unclear why they were favored over other cavity modes with higher Q-values. In this chapter we apply the SALT to the quadrupole cavities and analyze the mechanisms leading to these surprising observations. Due to the high-Q nature of quadrupole cavities, we scale the pump strength D_0 by $k_a R^{-2}(\sim 10^3$ in the cases studied below) for convenience. This convention is also used in the succeeding chapter.

6.1 Directional emission: mode selection

In this section we focus on explaining why the second bow-tie modes are the first lasing modes when $\epsilon \geqslant 0.16$. Here we briefly review the evolution of cavity modes in a quadrupole

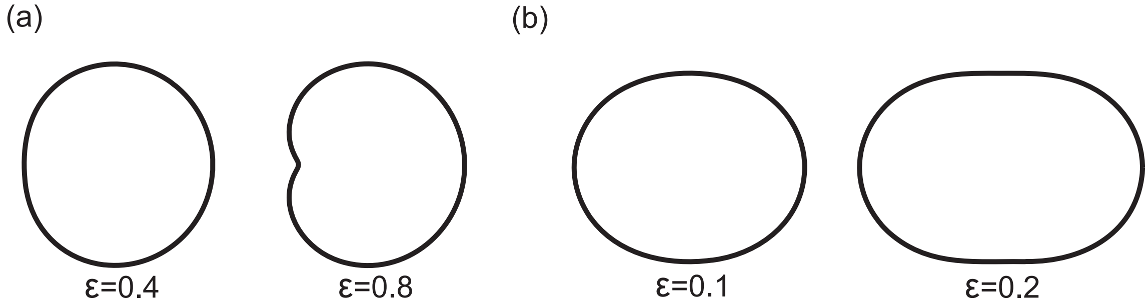

Figure 6.1: Examples of asymmetric resonant cavity (ARC) lasers. (a) Limacçns with $\epsilon = 0.4, 0.8$. (b) Quadrupoles with $\epsilon = 0.1, 0.2$.

cavity when the deformation increases from zero. In the semi-classical limit ($kR \gg 1$) the solutions of the Helmholtz equation, including both the CF states and the QB modes, have their classical correspondences in the ray model [28], which assumes light travels in straight lines and neglects wave effects such as interference. In this model one follows an ensemble of rays which undergo specular reflections when they impinge on the boundary, and records the coordinates of their bouncing points and the momenta of the emerging rays. The coordinate is normally chosen to be the azimuthal angle (ϕ) on the boundary or the arclength measured from $\phi = 0$, and the the conjugate momentum is conveniently expressed as the sine of the incident angle χ since the energy, or the length of the momentum vector, is conserved in a closed cavity. The Poincaré surface of section (SOS) [95, 96] is the projection of the phase space motion onto the boundary in terms of these two quantities.

At zero deformation, i. e., in a microdisk cavity, the motion of the ray follows a straight line in the SOS with a constant $\sin \chi$ since the angular momentum is conserved. There are infinite numbers of these trajectories, but only those satisfying the Einstein-Brillouin-Keller quantization criterion give rise to the cavity modes [97, 98, 99]. In standard ray model analysis the cavity is assumed to be closed and a ray is trapped indefinitely. In lasers however, the leakage, including both the evanescent tunneling and the refraction loss, gives rise to the output beam and the open boundary condition needs to be adopted [100, 28, 31]. This is incorporated by assigning an intensity to each ray and using the modified Fresnel Law [101] to calculate the remaining and refracted intensities each time the ray collides

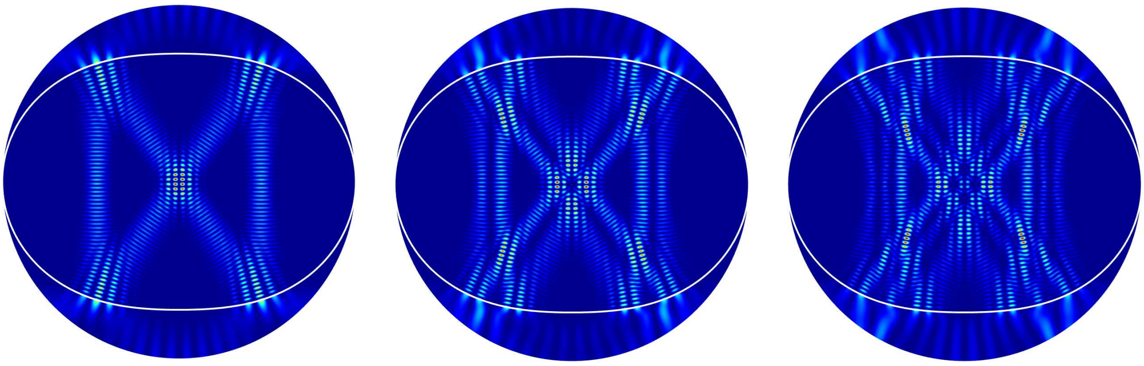

Figure 6.2: False color plots of the 0th, 1st and 2nd bow-tie modes with $\{-,-\}$ parity in a quadrupole cavity at $\epsilon = 0.16$ and with refractive index $n = 3.3 + 0.02i$. Other parameters used are: $R_0 = 34.5238\ \mu m$ and $k_a = 1.216\ \mu m^{-1}$. The circular region shown is the last scattering surface chosen for this calculation, and the white curve indicates the true cavity boundary.

with the boundary. Note that even when χ is above the critical angle $\chi_c = \sin^{-1}(1/n)$ there are still output beams due to the evanescent tunneling [23]. It results in the extreme WG modes introduced in Section 3.3 (see Fig. 3.10(a)), which have high Q-values and will be the first lasing modes when gain is added to the cavity.

When the circular cavity becomes deformed, the angular momentum is no longer a conserved quantity; $\sin\chi$ oscillates in the SOS, which follows unbroken curves close to $\sin\chi = 1$ [102] but becomes partially chaotic for small $\sin\chi$ [14, 51]. Structures formed by closed curves appear in the SOS which correspond to stable motions; these structures are known as "islands" and the structureless chaotic region are sometimes called the "chaotic sea". Two of such islands are located near $(\sin\chi, \phi) = (0, \pm\pi/2)$, representing the diametral Fabry-Perot modes along the minor (compressed) axis. When the deformation becomes greater than 0.1 the bow-tie orbits, together with the unstable V-shaped orbits, emerge from these two islands (see Fig. 6.3). The bow-tie islands move upwards in the SOS when ϵ increases, and they become the only large island near or above the critical angle when $\epsilon \geqslant 0.16$. The QB modes supported by these orbits have the same frequency spacing as in the experiment, and the ones with the second-order transverse excitation give the observed directionality. Thus the authors in Ref. [14] suggested that the lasing modes are most likely the second-order bow-tie modes at large deformations.

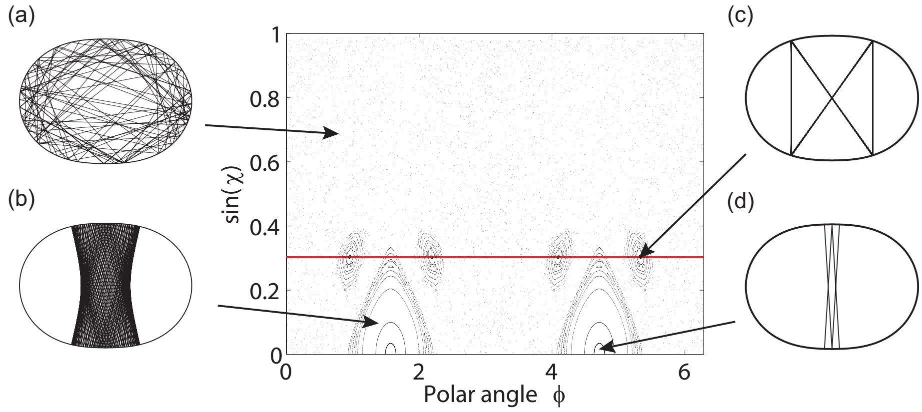

Figure 6.3: Surface of section for a quadrupole cavity of refractive index $n = 3.3$ at deformation $\epsilon = 0.16$ (center). Four types of modes are shown: (a) chaotic (b) diametral (c) bow-tie (d) V-shaped, but only (b) and (c) are stable. The red horizontal line indicates the critical angle $\sin(\chi) = 0.303$.

However, two crucial questions remain to be answered. First, although the islands of the bow-tie modes in the SOS are the most noticeable ones near or above the critical angle, there are other modes further above the critical angle. Fig. 6.4 shows the CF frequencies calculated at $\epsilon = 0.16$ near the gain center $k_a = 1.2160\,\mu m^{-1}$. The bow-tie modes are found to be near the bottom of the CF spectrum, with quality factors higher than the low-lying diametral Fabry-Perot modes but lower than the deformed WG modes and other "librational" modes (in contrast to "rotational" modes such as the WG modes). Therefore, we need to determine the factors that favor the bow-tie modes over the other ones with higher quality factors. Türeci *et al* [90] suggested that a spatially inhomogeneous pump due to the reduction of injected current near the edge of the cavity may favor the bow-ties modes over the WG modes as it overlaps more with the former. They used the third order Haken-Sauermann theory discussed in Chapter 1, and found the thresholds of the bow-tie modes are greatly reduced by using a Gaussian pump profile peaked at the center of the cavity. But the chosen pump profile also favors other librational modes which have lower thresholds and larger output intensity at pump power. Similar to the first question but probably more challenging, one finds that the second-order bow-tie modes have the lowest quality factors compared to the zeroth-order and first-order the bow-tie modes, making it puzzling why they turn on before the others.

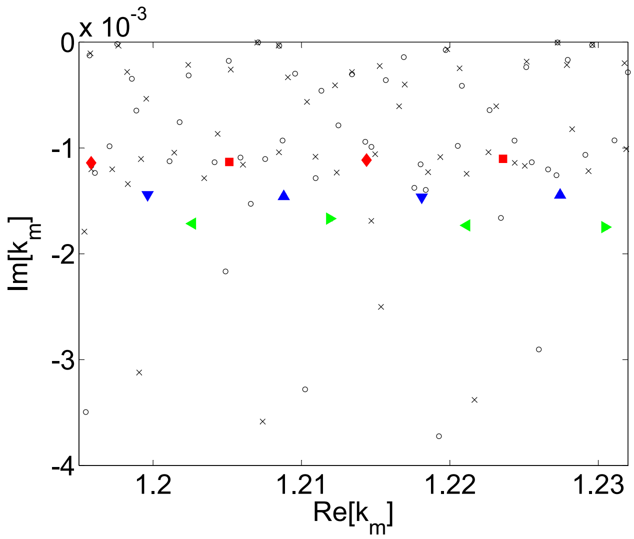

Figure 6.4: Complex frequencies of CF states in a quadrupole cavity at deformation $\epsilon = 0.16$. Shown are modes with either $\{+,+\}$ (circles) and $\{+,+\}$ (crosses) symmetry. Bowties modes are indicated by red squares ($\{-,-\}$) and diamonds ($\{+,+\}$), blue right ($\{-,-\}$) and left ($\{+,+\}$) triangles, green up ($\{-,-\}$) and down ($\{+,+\}$) triangles. The CF states are calculated at $k = 1.2160\mu m^{-1}$, and the cavity index and average radius are $n = 3.3$ and $R_0 = 34.5238\,\mu m$.

To answer these questions, we analyze the possible factors that can change the order of lasing thresholds given by the SALT. The modes in a quadrupole cavity we consider have high quality factors, and the threshold matrix is approximated diagonal even though the pump may not be homogeneous. Therefore, we use Eq. (4.4) in our analysis which states that the threshold is proportional to κ_m, the imaginary part of the complex frequency. Two factors contribute to κ_m: the cavity loss κ_{cav} and the out-coupling loss κ_{out}. The CF frequencies shown in Fig. 6.4 are calculated assuming $\kappa_{cav} = 0$, and $\kappa_m = \kappa_{out}$ which is inversely proportional to the quality factor, or equivalently, the lifetime of the mode. In a QCL, however, the cavity loss usually dominates [14] and it affects modes with high quality factors more since they have a longer lifetime inside the cavity. Therefore, a large κ_{cav} reduces the fractional difference of a high-Q and a lower-Q modes. But this effect alone cannot change the order of their threshold. Another factor in Eq. (4.4) that affects the order of thresholds is the distance of the CF frequency to the gain center on the real axis. Since the CF spectrum is very dense (see Fig. 6.4), it is unlikely that only the thresholds of the bow-tie modes are reduced. One important factor which is not considered in Eq. (4.4) is the spatial pump profile. If the overlap of the pump $D(\boldsymbol{x})$ with one type of mode is greater than the others, their thresholds are all reduced by a larger fraction which leads to the reordering of lasing modes. The above mentioned points were also tested in Ref. [90] using the QB modes, but the results were not as clear as what we are going to demonstrate.

Following these two findings we assume the cavity is lossy and the pump $D(\boldsymbol{x})$ peaks near the center of the cavity when applying the SALT. Instead of adding a phenomenological κ_{cav} to the imaginary parts of the CF frequencies, we use a complex cavity index ϵ_c with a positive imaginary part instead. Many processes contribute to the the added imaginary part in a QCL including phonon and free carrier absorption and impurity scattering [103, 104]. Here we also consider another process contributing to the cavity loss, which is related to the stimulated absorption of emitted photons in the unpumped region with gain. Since the energy of the lasing modes ($\hbar\omega^\mu$) are close to the energy difference of the two gain levels which undergo the lasing transition, the unpumped gain region acts as a saturable absorber. If there is no other degrees of freedom to which the gain medium couples, it stops absorbing light in the unpumped gain region once the system becomes transparent ($D(x) = 0$), i. e., there are equal numbers of photon being absorbed and re-emitted at the same time. But processes such as inelastic collisions in an atomic gas and phonon interactions in a semiconductor cause part of the energy stored in the inverted gain medium decays into other forms of energy (e. g., heat) other than light. Therefore, the stimulated absorption rate must be larger than the stimulated emission rate to balance the non-radiative decay from the upper level to the lower level when the above mentioned equilibrium is established. This means that there will be more atoms in the lower level than in the upper level, leading to a persistent absorption.

The laser cavities used in Ref. [14] are made of InGaAs/InAlAs which also act as the gain medium, and we use $n = 3.3+0.0005i$ inside the pump region and $n = 3.3+0.0035i$ in the unpumped region. For the pump profile $D(\boldsymbol{x})$, we assume that it is a constant inside the ohmic contact applied to the top and bottom surfaces of the lasers (see Fig. 1.2(b)) and zero elsewhere. Note that bow-tie modes of $\{-,+\}$ and $\{+,+\}$ symmetries are quasi-degenerate; The same is true for bow-tie modes of $\{+,-\}$ and $\{-,-\}$ symmetries [99]. Therefore, we take into account 300 modes with $\{+,-\}$ and $\{-,+\}$ symmetries in the vicinity of the gain center, including the deformed whispering-gallery modes, and we find the six modes with the lowest non-interacting thresholds are the zeroth-order bow-tie modes. Fig. 6.5 shows all the thresholds below $D_0 = 0.14$ and the corresponding frequencies, and we can see clearly the frequencies of the six lowest threshold form a equally-spaced sequence with $\delta_k = 0.009\mu m^{-1}$ (or $\delta_\lambda = 38.2\mu m$), very similar to that found in the experiment. This result is robust when the area of stadium pump profile is scaled in the range $[0.7, 1.7]$ times that of the ohmic contact, and it confirms that the bow-tie modes can be the first lasing modes despite their relatively low quality factors.

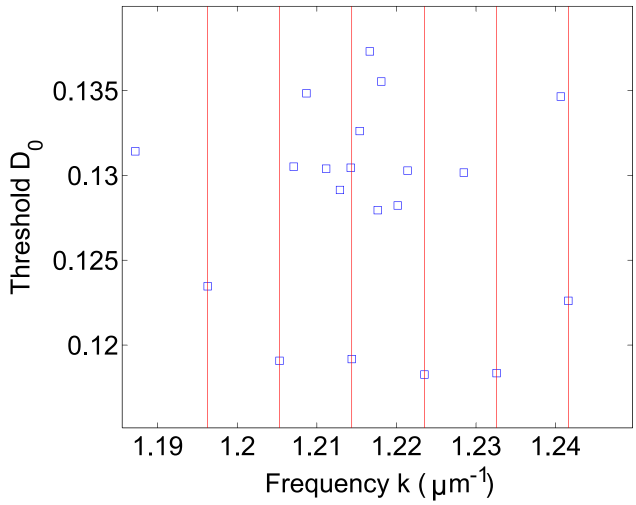

Figure 6.5: Non-interacting threshold versus frequency in a quadrupole cavity with deformation $\epsilon = 0.16$. The vertical lines mark the frequencies of the six modes with the lowest non-interacting threshold, which turn out to be all zeroth-order bow-tie modes.

In this calculation we also found that each lasing mode is essentially one CF state, which is consistent with our previous claim that the "single-pole" approximation is good for high-Q modes. We will use the "single-pole" approximation in the following discussions. The structure of the self-consistent equation (2.50) also states that the lasing modes have certain parities if the pump profile is symmetric about both the horizontal and vertical axes. In other words, each lasing mode is made up of CF states of the same reflection symmetry. This is a consequence of the fact that the spatial hole burning is a function of the intensity of the lasing modes, not their complex amplitudes.

With the above mentioned parameters, however, the second-order bow-tie modes have relatively large threshold. To distinguish the second-order bow-tie modes from the zeroth-order and first-order ones, we first note that their internal intensities have different radial variations: the second-order ones are weakest near the edge of the cavity (see Fig. 6.2). Therefore, we test a series of disk-shaped pump profiles whose radius r_{pump} varies from R_{minor} to $0.4R_{minor}$ *with bow-tie modes only*, and we find the second-order bow-ties do have the lowest threshold at small r_{pump} when the absorption is relative high. For example, the average threshold of the four second-order bow-tie modes closest to the gain center is the lowest one when $r_{pump} < 0.75R_{minor}$ if we assume $n = 3.3 + 0.02i$ in the cavity (see Fig. 6.6(a)), and the difference between it and the average thresholds of the other bow-tie modes peaks at $r_{pump} = 0.55R_{minor}$. We use this setup to test the above threshold behavior of all the bow-tie modes, and find that there are only second-order bow-tie modes lasing up to the pump value $D_0 = 0.265$ where a first-order bow-tie turns on. Fig. 6.6(b) shows the far-field pattern just before this mode turns on and it peaks at $\theta = 43°$, agreeing reasonably well with the experiment result considering no mode other than the second order bow-tie modes emit in the $\theta \approx 43°$ direction.

To compare quantitatively the results given by the SALT with the experiment result in Ref. [14], we need to know the exact pump profile $D(\boldsymbol{x})$ which is difficult to obtain. But with the reasonable estimation for $D(\boldsymbol{x})$ based on the limited knowledge we have, we were able to show in the discussion above that the bow-tie modes in a quadrupole cavity at deformation $\epsilon = 0.16$ can be the first modes to lase and the second-order ones can have the lowest threshold among all the bow-tie modes. There might be some physical processes we leave out in the SALT that are important in QCLs, as we couldn't find a parameter regime in which the second-order bow-tie modes are the only lasing modes above threshold when all modes are considered.

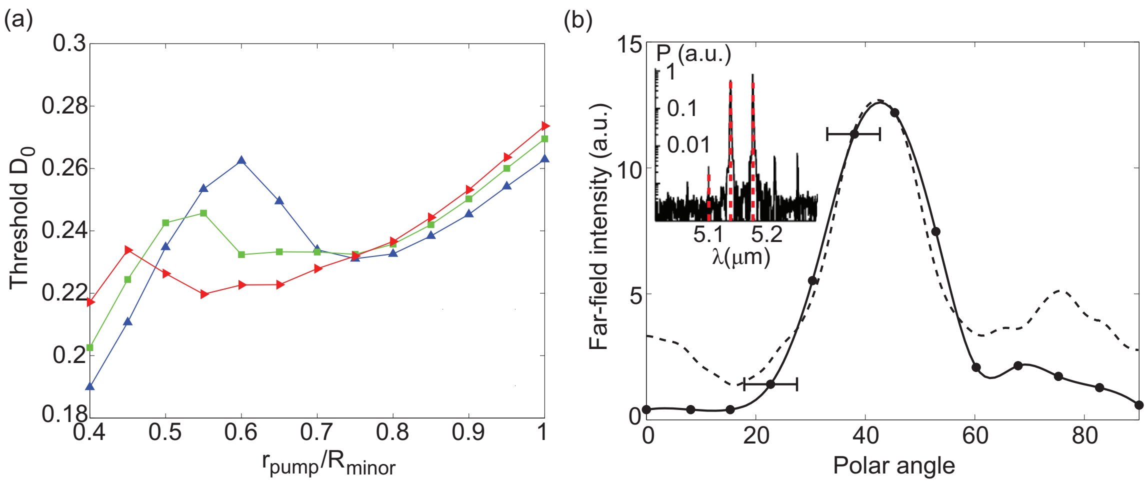

Figure 6.6: (a) Average non-interacting thresholds (power per unit area) of different orders of bow-tie modes as a function of pump radius in a quadrupole cavity with $\epsilon = 0.16$ and a refractive index $n = 3.3 + 0.02i$. The symbols used are: up triangles (0st), squares (1st), and right triangles (2nd). Other parameters used are: $R_0 = 34.5238$, $n = 3.3 + 0.02i$, $k_a = 1.216\,\mu m^{-1}$ and $\gamma_\perp = 0.1$. (b) Far-field pattern of all the lasing modes at $D_0 = 0.262$. The filled circles are the data taken from Ref. [14] and connected by a spline curve (solid line). The dashed line indicates the result given by the SALT using an aperture of 15° as in the experiment. Inset: Laser spectrum taken from Ref. [14] (solid line) and the SALT result (dashed lines).

6.2 Output power increase as a function of deformation

Another important observation in Ref. [14] is the quasi-exponential increase of the emitted power as the deformation ϵ increases. Our calculations show that this feature is quite general and doesn't depend much on the pump profile and cavity index *as long as* the cavity loss dominates the total loss. For example, we plot in Fig. 6.7 the integrated far-field intensity of all lasing modes in various deformed quadrupole cavities using $r_{pump} = 0.7R_{minor}$ and $n = 3.3+0.02i$. In (a) we note that the first thresholds in all of these cavities are close to each other ($D_{th}^{(1)} = 0.2 \sim 0.25$) despite the huge difference of the average out-coupling loss of the lasing modes. To understand this observation we point out that the threshold is determined by the total loss of the laser, which is the sum of the cavity loss and the out-coupling loss. Since the cavity loss ($\mathrm{Im}\,[n] = 0.02$) in this case prevails against the out-coupling loss, the latter only has a minor influence on the threshold values.

The output intensity, however, is determined by the average out-coupling loss of the lasing modes and the pump intensity above the threshold. Therefore, as the average Q-value is spoiled when the deformation becomes large, the out-coupling increases as 1/Q-value, leading to the quasi-exponential power increase. This is most clear in (b) where we extract the peak output powers at $D_0 = 0.5$ in Fig. 6.7(a). When performing the comparison we keep the length of the minor axis R_{minor} fixed while changing ϵ as in Ref. [14]. At each deformation 30 modes of $\{-,-\}$ symmetry with the lowest non-interacting thresholds are included in the calculation, some of which are suppressed from turning on even at the peak pump value $D_0 = 0.5$. At small deformations ($\epsilon = 0.01, 0.02$) most of the output comes from a few deformed whispering-gallery modes which are leakier than the others. At $\epsilon = 0.01$ there happens to be one such leaky whispering-gallery lasing mode very close to k_a, and its average angular momentum turns out to be smaller than those in the $\epsilon = 0.02$ case. Thus we see a small drop in the peak output power when ϵ increases from 0.01 to 0.02. The large increase of the output power at $\epsilon = 0.10$ is due to the turning on of a few "fish" modes and one diametral mode with a large transversal quantization number (see Fig. 6.8), which have much stronger out-coupling compared with the lasing modes at deformation $\epsilon = 0.08$. Above $\epsilon = 0.16$ bow-tie modes and other librational modes dominate, which increase the output power even further.

A similar output boost as a function of deformation is also observed in elliptic cavities, in which the ray dynamics is regular and no chaos is present. Thus we conclude that the output power enhancement is due to the Q-spoiling of the cavity as the deformation increases and this phenomenon is insensitive to the ray dynamics in the cavity.

We have done extensive calculation for the threshold modes in the limacqn ARC laser [106] which doesn't require the full nonlinear SALT. This work is not reported in this thesis.

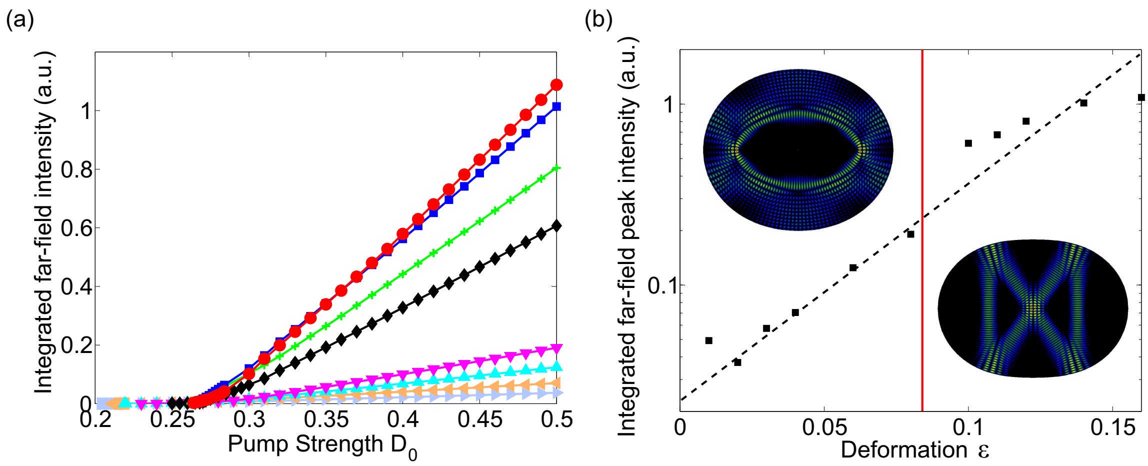

Figure 6.7: (a) Far-field intensities as functions of the pump strength in various deformed quadrupole cavities. The symbols used are: right triangles ($\epsilon = 0.02$), left triangles ($\epsilon = 0.04$), up triangles ($\epsilon = 0.06$), down triangles ($\epsilon = 0.08$), diamonds ($\epsilon = 0.1$), pluses ($\epsilon = 0.12$), squares ($\epsilon = 0.14$) and circles ($\epsilon = 0.16$). (b) Quasi-exponential increase of the peak output power (at $D_0 = 0.5$) as the deformation of the quadruple cavity increases. The dashed line representing an exponential curve is to used to guide the eyes. The red vertical line divide ϵ into two regimes. The lasing modes in the regime on its left are rotational modes, with the left inset showing a scarred double-triangle mode at $\epsilon = 0.8$; the lasing modes in the regime on its right are dominated by librational modes, with the right inset showing a 0th-order bow-tie modes at $\epsilon = 0.16$.

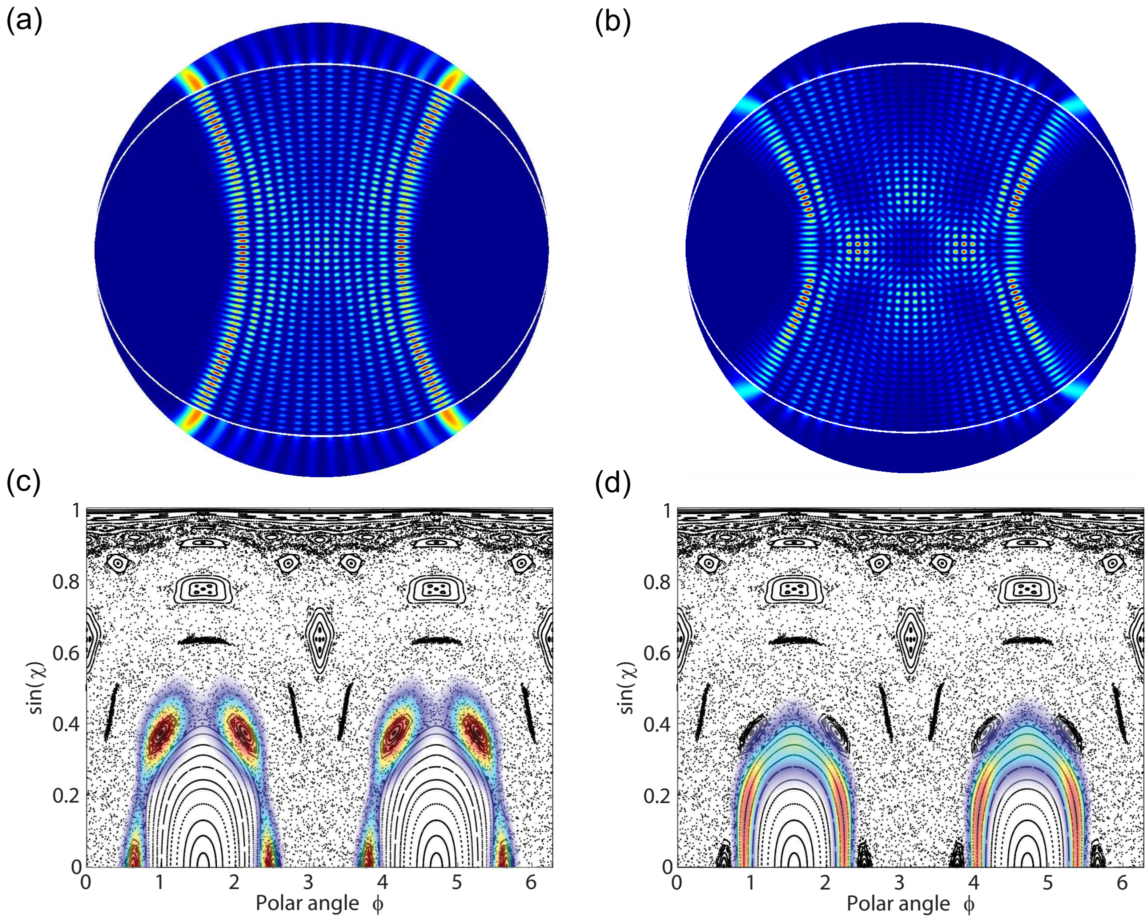

Figure 6.8: False color plot of a fish mode (a) and a diametral mode (b) in a quadurpole cavity at deformation $\epsilon = 0.10$. Only the intensity within the circular last scattering surface is shown, and the white curve indicates the cavity boundary. (c) and (d) show the projection of their Husimi function [51, 105] onto the Poincaré surface of section, which is a smoothed version of the Wigner Transform.

Chapter 7

Random lasers

Random lasing (RL) action *with coherent feedback*, in which a series of discrete narrow spectral peaks emerge in a disordered system with gain, was first demonstrated by Cao *et al* [37]. The study of the photon statistics [39] confirmed the coherence of the emitted light, which distinguishes it from the earlier results [107, 108] which were attributed to amplified spontaneous emissions in random media.

Time-dependent simulations of random lasers in dimensions other than 1D are time-consuming and computationally challenging since the index homogeneities are sub-wavelength. In this case the high efficiency of the SALT is more pronounced; our model, which was introduced in Section 3.5, consists of randomly placed nano-particles in a disk-shaped gain region of radius R. The CF states $\Psi_\mu(\boldsymbol{x})$ at frequency k are defined by equations (2.33) and (2.35)

$$\begin{aligned}\left[\nabla^2 + \epsilon_c(\boldsymbol{x})k_p^2\right]\varphi_p(\boldsymbol{x},\omega) &= 0, \quad (r < R),\\ \left[\nabla^2 + \epsilon_> k^2\right]\varphi_p(\boldsymbol{x},\omega) &= 0, \quad (r > R),\end{aligned}$$

with the out-going boundaries condition, which means the CF states outside the gain region are superpositions of the out-going Hankel functions. A typical example for a calculation of the multi-mode electric field both inside the "cavity" and outside is rendered in three-dimensions in Fig. 7.1. The system we consider has strongly-overlapping linear resonances; in the language of resonator theory, its finesse, f, (the ratio of the resonance spacing on the real axis to the typical distance of a resonance from the real axis) is much less than unity (see Fig. 7.2).

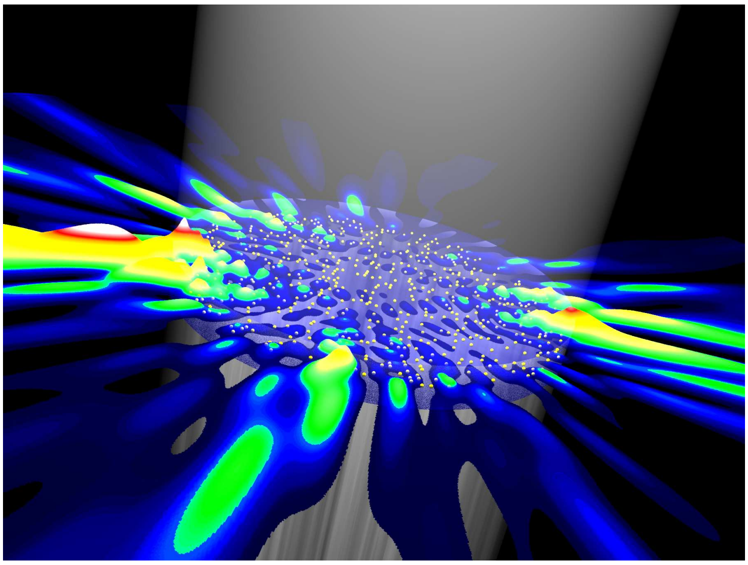

Figure 7.1: Three dimensional rendering of the electric field from SALT numerical calculations in the RL discussed below (see Fig. 7.2), in which the yellow spheres represent the nano-particles in a cylindrically symmetric gain medium. The electric field, where color and height indicate intensity, represents the steady state solution of the Maxwell-Bloch equations at $D_0 = 123.5$. The system is illuminated uniformly by incoherent light, shown in this figure as coming from above (courtesy of Robert J. Tandy).

The integral in Eq. (2.50) is now over the gain region, whose boundary is chosen to be the last scattering surface as we assume that there are no scatterers outside the gain region. As noted, the threshold matrix is diagonal only when $D_0(\boldsymbol{x})/\epsilon_c(\boldsymbol{x})$ is a constant. Here $\epsilon_c(x)$ varies in space due to the randomly placed nanoparticles, and we expect the threshold matrix to be non-diagonal and there can in principle be many CF states contributing to one threshold lasing mode. However since the CF states $\varphi_m(\boldsymbol{x})$ and $\varphi_p(\boldsymbol{x})$ that appear in the integral of Eq. (2.50) are uncorrelated fluctuating functions of space, it turns out that the threshold matrix in RLs is approximately diagonal and the threshold modes are dominated by one, pseudo-random CF state (see Fig. 7.3).

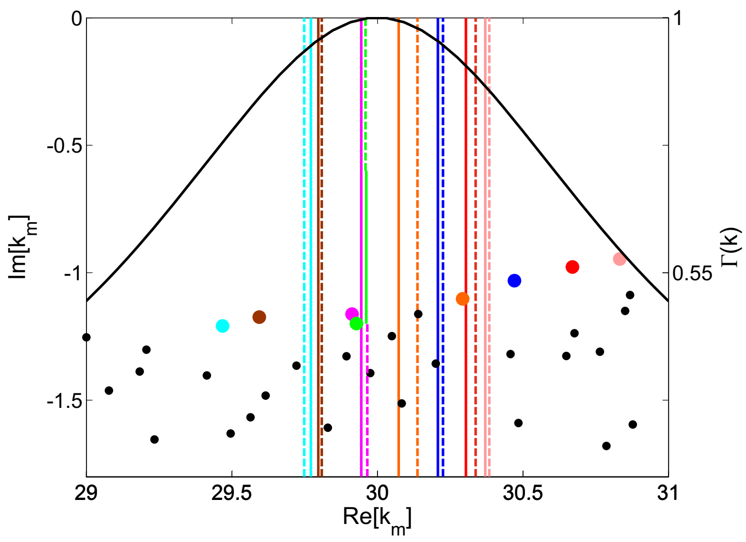

Figure 7.2: Lasing frequencies of a RL. Black circles represent the complex frequencies of the CF states. Because their spacing on the real axis is much less than their distance from the axis the system has no isolated linear resonances and the "cavity" has average finesse less than unity ($f \approx .05$). Solid colored lines represent the actual frequencies k_μ of the lasing modes at pump $D_0 = 123.5$; dashed lines denote the values $k_\mu^{(0)}$ arising from the single largest CF state contributing to each mode (the CF frequency is denoted by the corresponding colored circle). The thick black line represents the atomic gain curve $\Gamma(k)$, peaked at the atomic frequency, $k_a R = 30$. Because the cavity is very leaky the lasing frequencies are strongly pulled to the gain center in general, however the collective contribution to the frequency is random in sign.

7.1 Diffusive versus quasi-ballistic

A key conception in the description of light propagation in disordered media is the (scattering) mean free path l_s [109, 110], which is the average distance between two successive scattering events encountered by a photon. When l_s is longer than the system size, photons generated in the gain region follow approximately ballistic motion, escaping rapidly to the outside with a small chance of being scattering by the nano-particles. When the system size, the density of scatterers or the scattering cross section is increased such that the l_s is comparable than the system size, a photon experiences multiple scattering before it diffuses out, leading to a longer life-time inside the gain region. In three dimensions beyond a critical amount of scattering which makes the l_s smaller than the wavelength, the diffusion stops and we enter the Anderson localization regime [111, 112]; the wavefunction

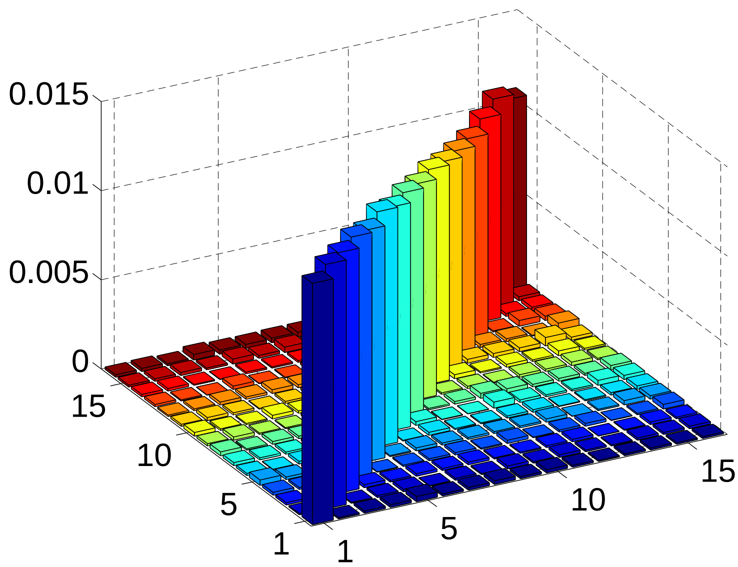

Figure 7.3: Typical values of the threshold matrix elements $\mathcal{T}^{(0)}$ in a two-dimensional RL schematized in the inset Fig. 7.2 using sixteen CF states. The off-diagonal elements are one to two orders of magnitude smaller than the diagonal ones. The natural unit of the pump strength (D_{0c}) determines the scale of the diagonal matrix elements (~ 0.015), the inverse of which gives the scale of the threshold (~ 70).

of the lasing modes decays exponentially inside the cavity giving rise to extremely high-Q modes. RLs were once proposed as a way to observe Anderson localization of light [113], but not until recently was such an observation reported [114]. In this chapter we consider RLs operating away from the localization regime, and the results to be presented below are in either the diffusive regime or the quasi-ballistic regime.

The first SALT calculations for RLs were done without a reliable method for calculating the mean free path [65], and we incorrectly assumed that the system was in the diffusive regime because the spectrum of the CF states was strongly changed from that in the pure ballistic regime and the CF wavefunctions appeared pseudo-random in the regime as disorder was varied (e. g., see the inset of Fig. 7.4(a)). Now we know that $l_s \gtrsim 30R$ in the cases we investigated, and we will refer to this regime as the quasi-ballistic regime. Recent work [115] shows that SALT calculations in the diffusive regime is possible but challenging because it requires the grid spacings Δ_r and $R\Delta_\theta$ used in the discretization method (Section 3.4) to be much smaller than the wave length, which in turn is much smaller than the mean free path, now only a fraction of the system size in the diffusive regime. Some phenomena are different from the results in the quasi-ballistic regime as we will briefly discussed below.

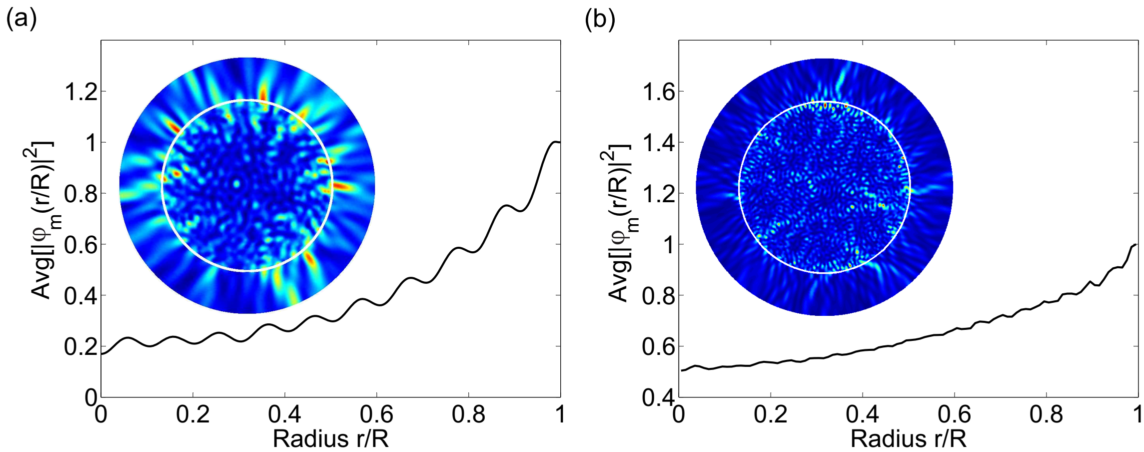

Figure 7.4: Spatial variation of the CF states in the quasi-ballistic regime (a) and in the regime approaching the diffusive regime (b). The curve in (a) shows the corrected data from Fig. 4 in Ref. [65]. The mean free paths are about $70R$ and $3R$ in these two cases, and the insets show the false color plots of the multi-mode electric field far above threshold. kR used in (a) is $kR = 30$, the radius and index of the nanoparticles is $r = R/80$ and $n = 1.2$, and the filling fraction is 20%. The parameters used (b) are given in the caption of Fig. 7.8.

7.1.1 Spatial inhomogeneity of lasing modes

We first discuss a noticeable difference of RLs in these two regimes, the spatial inhomogeneity of the electric field shown in Fig. 7.4. The intensity of the multi-mode electric field in the quasi-ballistic regime displays a striking property: it is consistently brighter at the edge of the disk than at its center, even though the gain is uniform and there are no special high-Q modes localized near the edge. To demonstrate that this effect is not a statistical fluctuation associated with this particular disorder configuration we have averaged the behavior of the entire basis set of CF states over disorder configurations. The result is a non-random average growth of intensity towards the boundary. The origin of this effect is known from earlier work on Distributed Feedback Lasers with weak reflectivity [116]; if the single-pass loss is large, then the single-pass gain must also be large in order to lase, leading to a visible non-uniformity of the lasing mode, with growth in the direction of the loss boundary (on average the radial direction for the RL). As the RL has fractional finesse (which is not achievable in a one-dimensional geometry) this effect is much larger in these systems and should be observable. This effect means that the electric field fluctuations in RLs will differ substantially from the random matrix/quantum chaos fluctuations of linear cavity modes [117], first because each mode is a superposition of pseudo-random CF states and second because these CF states themselves are not uniform on average. We find that this effect to become weaker as the disorder strength is increased and eventually becomes negligible (see Fig. 7.4(b)).

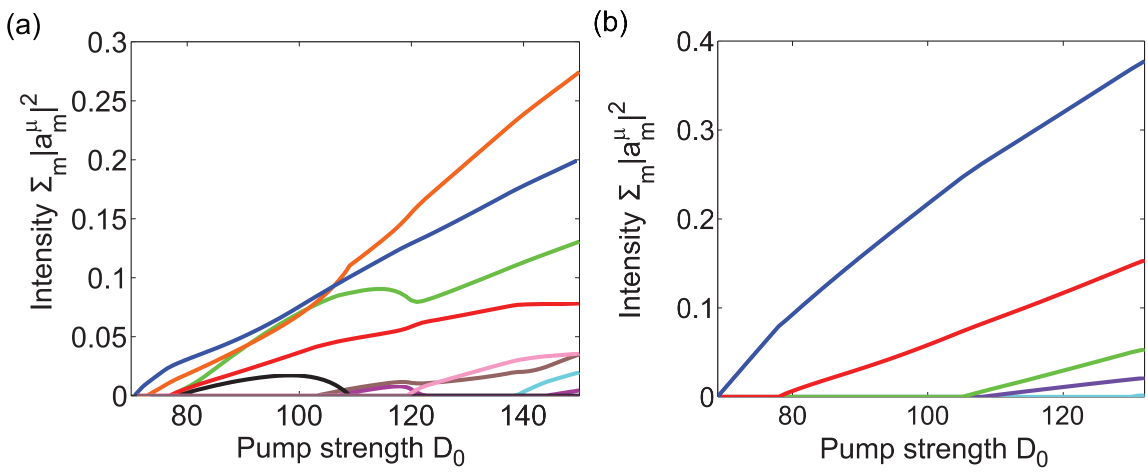

Figure 7.5: Modal intensities of a RL as a function of D_0 in the quasi-ballistic regime (a) and in the diffusive regime (b). Parameters used here are the same as in Fig. 7.4.

7.1.2 Modal intensities versus pump strength

In the quasi-ballistic regime the behaviors of modal intensities, measured by the length of the vector of CF coefficients $I = \sum_{m=1}^{N_{CF}} |a_m^\mu|^2$, show complex non-monotonic behaviors (see Fig. 7.5(a)). Interestingly, we see that modes can be "killed" (e. g., the black mode) and some of them can "reincarnate" themselves at a higher pump (the purple mode).

Analysis reveals that these complex behaviors are due to the strong spatial hole burning interactions in these systems as we will see below. In contrast, the modal intensities of a RL in the diffusive regime increase monotonically as a function of the pump strength (Fig. 7.5(b)), which is similar to what we have shown for the conventional multi-mode laser (Fig. 4.4). However, we do observe strong modal interaction in the diffusive regime also as we now show by analyzing the eigenvalues of the interacting threshold matrices defined in Section 4.2 and the frequency distribution of lasing modes.

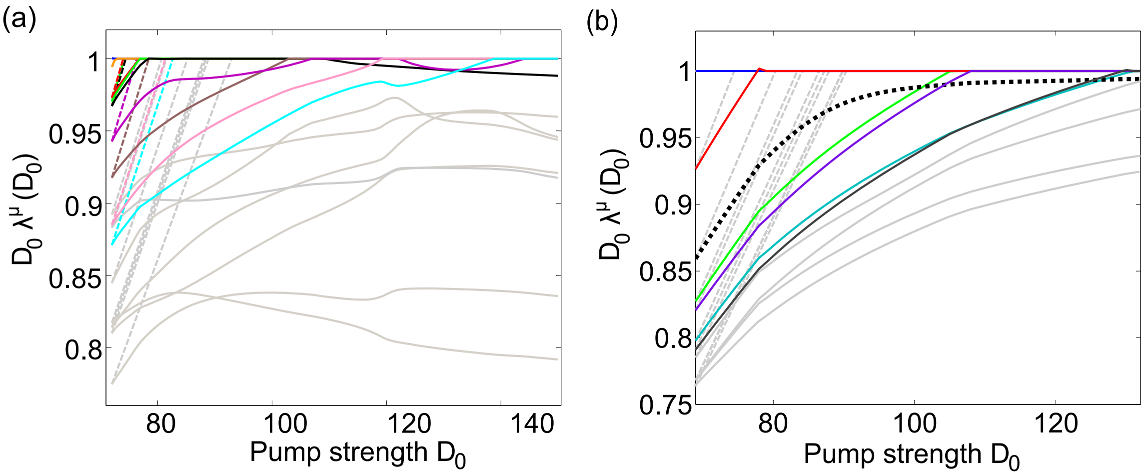

Figure 7.6: Evolution of the quantities $D_0\lambda^\mu(D_0)$ of a RL as the pump is increased in the quasi-ballistic regime (a) and in the diffusive regime (b). The lasing threshold corresponds to the line $D_0\lambda^\mu = 1$. The full colored lines represent the modes which start lasing within the calculated range of D_0, and the gray dashed lines represent the non-interacting thresholds for the modes shown. The mode represented by the dark dotted line in (b) is the third mode in the absence of mode interaction, but it doesn't turn on at all when the interaction is included. Parameters used here are the same as in Fig. 7.4.

7.1.3 Lasing frequencies versus pump strength

In Fig. 7.7 we plot the lasing frequencies of the modes shown in Fig. 7.5 when the pump is increased. Of the eight lasing modes in the quasi-ballistic case, there are six which form three pairs nearby in frequency and their behavior is highly correlated. Evaluation of the overlap of the $\mathbf{a}^\mu$ vector associated with each pair of modes confirms that not only their frequencies, but also their decomposition into CF states is similar. When two lasing

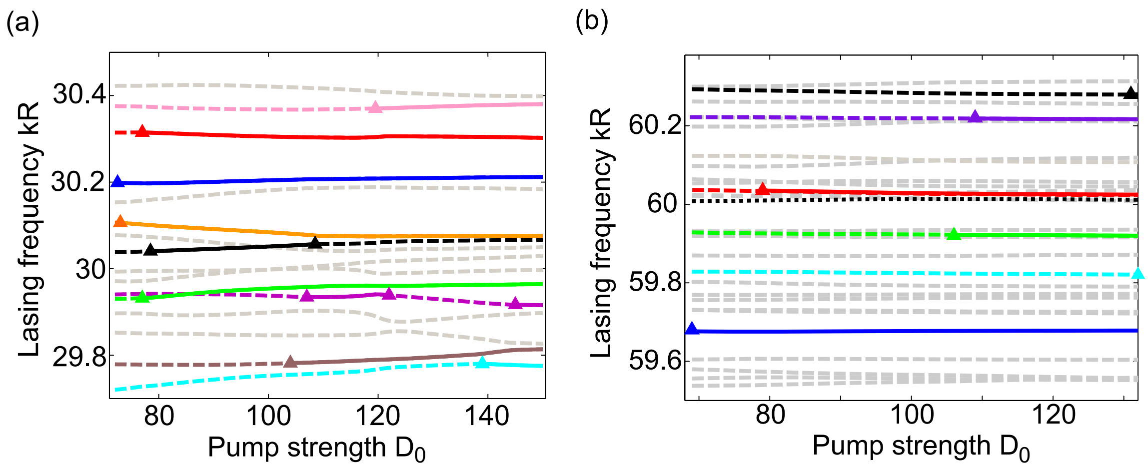

Figure 7.7: Lasing frequencies of a RL versus pump above (solid) and below (dashed) threshold in the quasi-ballistic regime (a) and in the diffusive regime (b). Gray dashed lines indicate the frequencies of the modes that don't turn on. The black dotted line in (b) represents the dotted line in Fig. 7.6(b). Parameters used here are the same as in Fig. 7.4.

frequencies approach one another, instead of repelling, one of the frequencies disappears (e.g., the "black" frequency in Fig. 7.7(a)), because the corresponding mode is driven to zero, an effect which cannot happen in a linear system. Recall that these frequencies are not the eigenvalues of a random matrix but rather the parameter values k_μ at which the random operator $\mathcal{T}_{mn}$ has a real eigenvalue.

It is possible to analyze this condition in terms of the interacting threshold matrices. In order for frequency degeneracy to occur this random complex matrix would have to have two degenerate real eigenvalues at the same value of k_μ. We argue that level repulsion in the complex plane prevents this from happening. However, instead of leading to frequency repulsion, this effect leads to frequency locking, i. e., the two interacting modes merge into one. We can confirm this effect by noting that after one modes "dies", the CF decomposition of the surviving mode has large components associated with the mode which was driven to zero. So instead of the "exchange of identity" familiar from linear level repulsion, we find "merger of identity". In a time-dependent treatment, this kind of cooperative frequency locking is well-known, and it has been studied in a chaotic cavity laser in [88]. The interesting "reincarnation" behavior happens when the frequency of a "killed" mode moves far enough away from that of the dominant mode (see the modes represented by the purple and green line in Fig. 7.7(a)). In the specific case shown, all the non-lasing modes at the highest pump we study have decreasing $D_0\lambda^\mu(D_0)$ as the pump is increased (Fig. 7.6(a)). Therefore, they are highly unlikely to be lasing at a higher pump value and the spectrum will stay well spaced (solid lines in Fig. **??**(a)).

Although the modal intensities in the diffusive regime behave quasi-linearly, the modal interaction does lead to important consequences. For example, we observe strong frequency repulsion as shown in Fig. 7.8, which convinces us that we are not in the regime of Anderson localization [19, 118]. For each of the 100 disorder configurations we study, the pump strength is increased until we reach the six-mode regime. The distribution of the frequency spacing is clearly different from that in the absence of interaction (taken from the frequencies of threshold lasing modes); the chances of having extremely large or small spacing is reduced ($\langle \Delta k^2 \rangle$ reduces from 5.59×10^{-3} to 4.52×10^{-3} while $\langle \Delta k \rangle$ is roughly the same), and the spectrum is more equally spaced as a result.

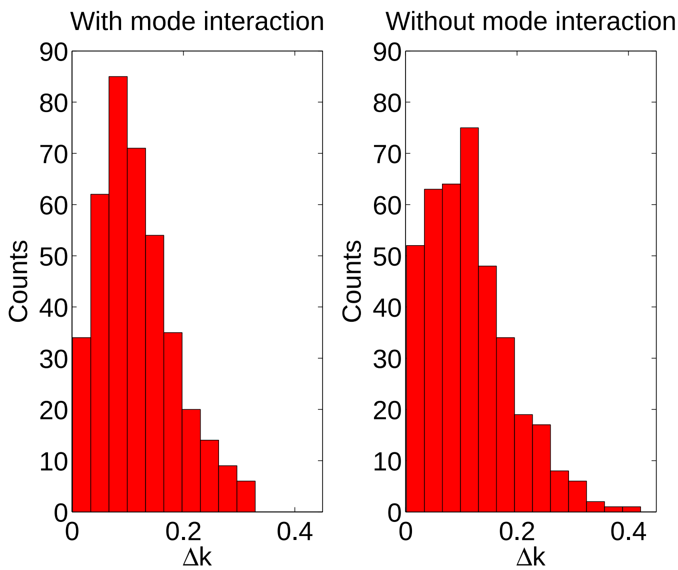

Figure 7.8: Distribution of nearest-neighbor lasing frequency spacing of diffusive RLs with mode interaction (a) and without mode interaction (b). 100 disorder configurations are studied and we increase the pump strength until it reaches the six-mode regime. In our calculation $kR = 60$, the radius and index of the nanoparticles are $r = R/30$ and $n = 1.4$, the filling fraction is 20%, and the mean free path is about $3R$.

Note that this phenomenon is not caused by shifting of individual lasing frequencies as a function of the pump strength; the pump-dependence of the lasing frequencies is rather weak in the diffusive regime (see Fig. 7.7(b)). The reason of the statistical change can be understood in the following way. Modes having similar spatial profiles tend to have similar lasing frequencies; the modal interaction through spatial hole burning suppresses the modes which have similar spatial profiles to those already lasing from turning on. Consequently, the lasing modes don't overlap much spatially and their frequencies are more likely to be well separated. For example, the mode which have the third lowest threshold in the absence of interaction (black dotted line in Fig. 7.7(b) and Fig. 7.6(b)) overlaps strongly with the second lasing mode (red line) and their frequencies are close to each other; the modal interaction highly suppresses the former and it doesn't turn on in the range we explore. As a result, the frequency spacing between the red mode and the nearest lasing mode increases from 0.03 to 0.1.

Although the suppressed mode doesn't turn on in the example above, it passes its identity to the second lasing mode as D_0 increases. In the absence of interaction the second lasing mode is dominated by the $28th$ CF state ($\xi_{28}^{(2)} = 98\%$), and the $30th$ CF state, which dominates the suppressed mode, has only a negligible contribution to the second lasing mode ($\xi_{30}^{(2)}$=1.5%). Here we have a larger basis compared to what we used in the 1D calculation, and the definition of ξ_m^μ is modified accordingly ($\xi_m^{(\mu)} \equiv |a_m^\mu|^2/\sum_n |a_n^\mu|^2$) to reduce the weights of the large number of near-zero components. At the largest pump value we investigate, the second lasing mode is mixed with a much larger amount of the suppressed mode, and $\xi_m^{(2)}$ becomes double-peaked with $\xi_{28}^{(2)} = 60.1\%$ and $\xi_{30}^{(2)} = 28.3\%$. Meanwhile, the suppressed mode also takes in a larger percentage of the second lasing mode and becomes double-peaked with $\xi_{30}^{(3)} = 53.9\%$ and $\xi_{28}^{(3)} = 28.5\%$. So we see these two modes overlaps more heavily as the pump increases, and the "modal gain" of the suppressed mode in Fig. 7.6(b) becomes more flat at higher pump and it never reaches its threshold as a result. This mixing phenomenon we describe is not a rare event. It happens for all the modes in the system; the example we give is just the most noticeable one.

7.2 Effects of fluctuations

The interaction effects in RLs are strongly non-linear and hence highly sensitive to statistical fluctuations, especially in the quasi-ballistic regime. To illustrate this in Fig. 7.9(a) we contrast the peak intensities of Fig. 7.5(a), for which the pump was uniform in space ($d_0(x) = 0$) to a case in which we have added to the uniform pump a random white noise term $d_0(x)$ of standard deviation $\pm 30\%$ (normalized to the same total power). For this non-uniform pump the third uniform mode (green) now turns on first. It is thus able to suppress the seventh uniform mode (purple) over the entire range of pump powers and acquires almost a factor of three greater intensity at the same average pump power. The intensities of all the interacting pairs show similar high sensitivity to pump profile, while their frequencies remain relatively stable. Similar behavior is also found in the diffusive regime (see Fig. 7.9(b)), which was observed in shot to shot spectra of RLs in experiments [46]. To better understand why the lasing frequency is stable we resort to the SALT for analytic insights into the question of what determines the frequencies of RLs. By imposing the gauge condition $\text{Im}[a_1^\mu] = 0$ for the dominant CF component at threshold, we derive from Eq. (2.50) that

$$k^\mu = k_a + \frac{1}{\kappa_1^\mu + \gamma_\perp}\left[-\frac{D_0\gamma_\perp \text{Im}\left[\sum_p a_p^\mu A_{1p}^\mu\right]}{a_1^\mu} + (q_1^\mu - k_a)\gamma_\perp\right], \tag{7.1}$$

in which q_m^μ and $-\kappa_m^\mu$ are the real and imaginary part of the CF frequency k_m^μ, and A_{mn}^μ is matrix element of the symmetric integral operator in Eq. (2.50). Here we use the approximation $(k^\mu)^2 - k_m^2 \approx 2k_a$ to emphasize the physical picture below, but it is not necessary in our calculation. We measure all frequencies from the atomic transition frequency k_a and write Eq. (7.1) as

$$\begin{aligned} k^\mu &= \frac{1}{1+\kappa_1^\mu/\gamma_\perp}\left[q_1^\mu - D_0\left(\text{Im}\left[A_{11}^\mu\right] + \sum_{p\neq 1}\text{Im}\left[A_{1p}^\mu\,\frac{a_p^\mu}{a_1^\mu}\right]\right)\right] \\ &\equiv k_\mu^{(0)} + k_\mu^{(c)}. \end{aligned} \tag{7.2}$$

$k_\mu^{(0)} = (q_1^\mu \gamma_\perp)/(\gamma_\perp + \kappa_1^\mu)$ is the weighted mean of the real part of the cavity resonance frequency and the atomic frequency. We encountered this "conventional" term in Section 4.1 when the threshold matrix was diagonal (Eq. (4.3)). For a typical high finesse system $k_\mu^{(0)}$ is very close to the cavity frequency $\text{Re}[k_\mu]$ with a small shift ("pull") towards the atomic line; $k_\mu^{(c)}$ is a collective contribution due to all the other CF states which has no analog in conventional lasers. In our parameter regime both the conventional and collective terms are important (although the conventional term is larger) and the lasing frequencies have no simple relationship to the "cavity frequencies". The collective term is random in sign and does not always generate a pull towards line center (Fig. 7.2). Eq. (7.2) shows explicitly that the lasing frequency k^μ is independent of the "gauge" condition we choose because only the relative phases of a_p^μ matter. Although we mentioned that the change in D_0 can be visualized as a modification to the effective dielectric function, here we separate the effective of the gain and stick to the CF basis of the cavity dielectric function $\epsilon_c(x)$. The "conventional term" $k_\mu^{(0)}$ in Eq. (7.2) is determined only by $\epsilon_c(x)$ and it stays the same with the pump fluctuation; since D_0 is the total pump power which we assume to be a constant and each mode is still approximately diagonal at threshold, the main contribution to the shift of $k_\mu^{(c)}$ comes from the change of $A_{mn}^\mu = \int_{cavity} d\boldsymbol{x}\,(1 + d_0(x))\varphi_m(\boldsymbol{x})\varphi_n(\boldsymbol{x})$. If the white noise $d_0(x)$ fluctuates uniformly in space as we assumed, then the average value of A_{mn}^μ is the same as in the uniform pumping case. The variance of A_{mn}^μ certainly depends the fluctuation amplitude of $d_0(x)$, but in a well-controlled experiment the latter is normally small which gives rise to the frequency stability.

7.3 Pump induced far-field directionality

One interesting question about RLs is what happens to the lasing modes in a partially pumped RL. Xu *et al.* [119] found that in the diffusive regime the spatial profile of lasing modes in one-dimension layered systems is significantly different from that of the corresponding cavity mode. Andreasen *et al.* [64, 67] investigated similar systems but with weaker scattering from the disorder and found new modes are formed which have high threshold but good directionality. We will analyze this observation in Chapter. 8 using a uniform edge-emitting laser. Here the question is whether we can utilize this observation

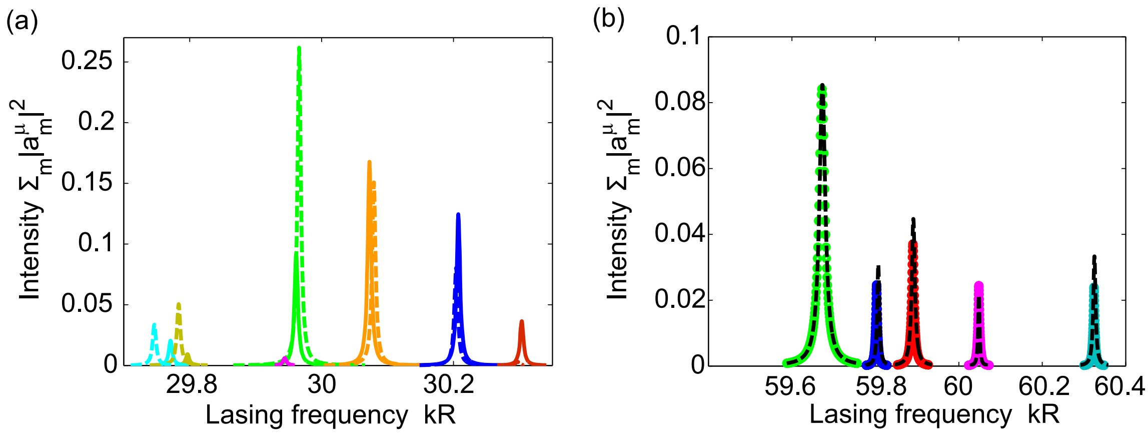

Figure 7.9: Intensity and frequency fluctuations of a RL in the quasi-ballistic regime (a) and in the diffusive regime (b). For fixed impurity configuration we compare lasing frequencies and intensities in the multi-mode regime for uniform pump (solid lines in (a) and circles in (b)) and uniform pump with 30% spatial white noise added (dashed lines).

to engineer the emission directionality of a RL. It is well known that in high-Q cavities one can pump certain areas of a laser to select certain modes [14, 120, 121]. For example, by pumping near the perimeter of a quasi-stadium laser diode with concentric end mirrors one can select the ring mode instead of the axis mode [120], and we discussed how the mode selection affects the emission pattern in a quadruple-deformed micro-cavity in the previous chapter. By selecting different cavity modes one has some freedom of choosing the desired emission directionality, but this procedure is limited by the fact that the pump cannot distort or reshape the spatial pattern of the lasing modes in high-Q cavities.

Our calculations in 2D RLs predict that good emission directionality can be obtained from locally pumped RLs if the scattering is weak enough (in quasi-ballistic regime; see Fig. 7.10(b)). As the scattering strength increases, the threshold value of a given mode is lowered. As a result, the lasing modes are not well confined within the pump region due to the reduced discontinuity of the imaginary part of the effective dielectric function at the boundary of the pump region. Therefore, lasing modes in the diffusive regime with local pumping look similar to those when a uniform pumping is employed and they emit randomly in all directions (Fig. 7.10(a)). The role of the disorder in the quasi-ballistic regime is quite interesting. Instead of scrambling the phase of the feedback, they enhance the feedback by supplying a more complicated network which effectively increases the system size and reduces the threshold. To illustrate this point we remove the scatterers in the system shown in Fig. 7.10(b), and the threshold of the corresponding lasing mode (with the fundamental transverse excitation) increases by 12.5%.

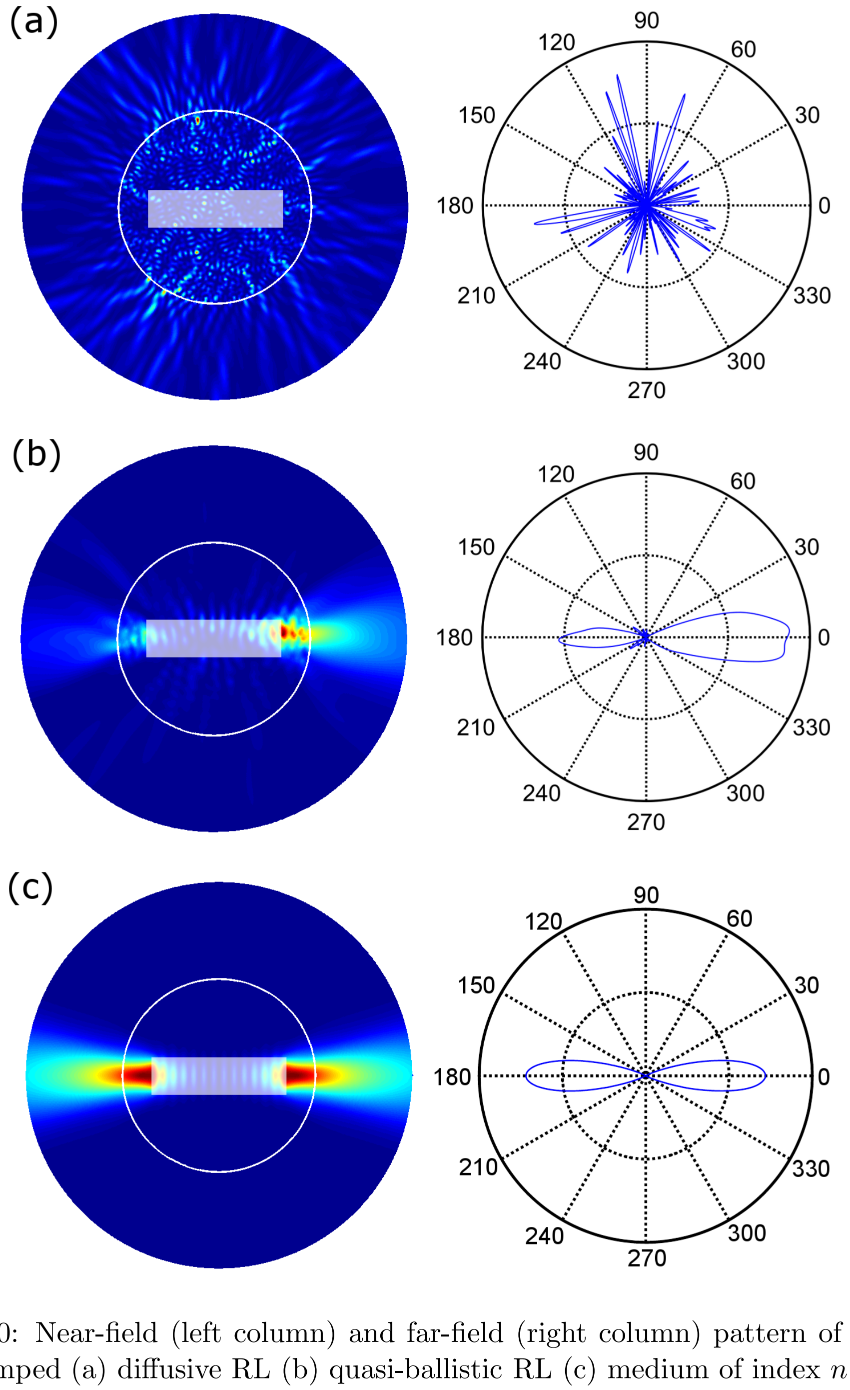

Figure 7.10: Near-field (left column) and far-field (right column) pattern of a TLM in a locally pumped (a) diffusive RL (b) quasi-ballistic RL (c) medium of index $n = 1$ (air).

Chapter 8

Threshold lasing modes in one-dimensional cavities with an inhomogeneous gain profile

In this chapter we address the question of what determines the lasing frequencies for a given pump power in a simple 1D edge-emitting laser. We found that the scattering from the gain boundaries inside the cavity play an important role; this is especially the case in relative low-Q cavities.

8.1 Conventional wisdom

The conventional wisdom on this problem is based on the cavity mode analysis: Cavity modes with longer lifetime and frequencies closer to the gain center utilize the gain better, thus they have the lowest thresholds and appear in the spectrum first when the pump power is above their thresholds. It is known that the lasing frequencies may shift from the cavity frequencies due to the interaction with gain, i. e., the line-pulling effect (4.3), but each laser frequency is still assumed to corresponds to one cavity mode. As the name suggests, cavity modes are only determined by the properties of the cavity and they are independent of the spectral and spatial characters of the gain medium and the pump. In Section 3.2.3 we showed that the threshold lasing modes in a laser with an inhomogeneous gain medium are the gain region CF states, whose spatial profiles can be different from cavity modes. What we haven't analyzed yet is whether the lasing frequencies still have a one-to-one relationship with the frequency of the passive cavity modes. It has been recently reported that lasing modes other than the cavity modes are found numerically in one-dimensional disordered systems with weak scattering [64, 67]. To understand why the conventional wisdom could be faulty, we reexamine how the cavity frequencies are determined in the most simple picture [3].

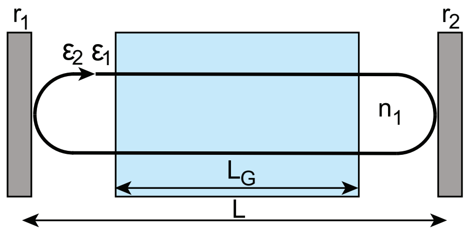

Figure 8.1: Schematic diagram of a simple Fabry-Perot cavity formed by two mirrors with reflection coefficients r_1 and r_2. The central block indicates the gain region.

The cavity shown in Fig. 8.1 is defined by two end mirrors with reflection coefficient r_1 and r_2, and the gain medium resides in the center block which doesn't necessarily fill the whole cavity. The gain medium is characterized by its length L_G and the amplification coefficient (or threshold) α_m. The light bounces back and forth between the two mirrors, amplified when propagating in the gain medium before it eventually leaks out when refracted by the two mirrors. The ratio of the light amplitudes before and after it finishes a round trip in the cavity can be written as:

$$\mathcal{E}_2/\mathcal{E}_1 = r_1 r_2 \exp(2\alpha_m L_G - 2in_1kL), \tag{8.1}$$

where the two terms in the exponent represent the amplification and the phase shift, respectively. One underlying requirement of laser action is coherent feedback, and in the one-dimensional case it simply requires $\mathcal{E}_2$ and $\mathcal{E}_1$ to be superposed coherently. The criterion is meet when the phase shift $2n_1kL$ is an integer times 2π, or $k = m\pi/n_1L\,(m = 1, 2, 3, \dots)$. From this derivation we see the cavity frequency k is independent of the both the amplification coefficient α_m and the gain length L_G. In Eq. (8.1) no phase shift due to the reflections by the two mirrors is added because it is zero when light is reflected from the optically dilute side of an interface. For other setups (boundary conditions) the possible phase shifts are known once the cavity is given, and they don't change the basic conclusion. However, the gain medium modifies both the real part and imaginary part of the refractive index (a detailed discussion can be found in Section 2.5 or [3]), but no reflection from the boundaries of the gain region is considered in Eq. (8.1). This can only be justified in high-Q cavities where the threshold is low and the change of the refractive index due to the gain can be neglected. Therefore, one needs to be careful when applying the conclusion of Eq. (8.1) to low-Q cavities including the one-dimensional disordered systems mentioned above [64, 67].

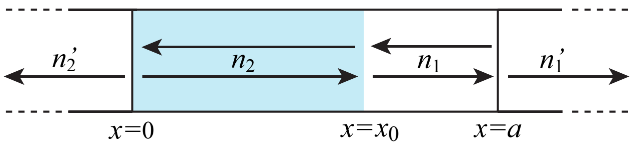

Figure 8.2: Schematic diagram of a two-sided 1D edge-emitting laser. The blue block indicates the gain region.

8.2 Linear gain analysis of threshold lasing modes

Below we find and analyze new modes introduced *by* the gain medium in one-dimensional slab cavities similar to the one shown in Fig. 3.5 using the linear gain model introduced in Section 2.5. These modes are shown to be related to the new modes found in [64, 67]. For generality we assume the one-dimensional laser emits through both sides (see Fig. 8.2). Eq. (2.59) in this case reduces to the following form:

$$\frac{1}{n_2}\sin(\theta_2 + n_2 k\, x_0)\cos(\theta_1 + n_1 k\,(a - x_0)) + \frac{1}{n_1}\cos(\theta_2 + n_2 k\, x_0)\sin(\theta_1 + n_1 k\,(a - x_0)) = 0. \tag{8.2}$$

Here k is the real-valued lasing frequency and n_2 is the index in the gain region with a negative imaginary part, representing the amplifying effect. The real part of n_2 may differ from

n_1, which is taken to be real. The angles $\theta_\mu \equiv \arcsin(\frac{n_\mu}{\sqrt{n_\mu^2 - {n'_\mu}^2}}) \equiv \arccos(\frac{-i}{\sqrt{n_\mu^2 - {n'_\mu}^2}})$ ($\mu = 1, 2$) are introduced to simplify this equation, and they can be written explicitly as

$$\theta_\mu = \frac{\pi}{2} + \frac{i}{2}\ln(\frac{n_\mu + n'_\mu}{n_\mu - n'_\mu}). \tag{8.3}$$

Here n'_μ ($\mu = 2, 1$) are the indices of the two semi-infinite media outside the cavity, and we take them to be unity (air) in the following discussion. The one-sided case (see Fig. 3.1) can be treated as a special case where the refractive index outside the left side of the cavity is infinite. In the following discussion we will take n'_μ to be unity, which doesn't affect the phenomena we are going to reveal. We use the linear gain model and assume the real part of the index region 2 is unchanged ($n_2 = n_1 + in_i$) in the presence of the gain medium following Eq. (2.60). The solutions which make the two terms in Eq. (8.2) vanish seperately have

$$k = \frac{m\pi - i\ln(\frac{n_1+1}{n_1-1})}{2n_1(a - x_0)}, \quad m = 0, \pm1, \pm2, ..., \tag{8.4}$$

which can be real only if $\mathrm{Im}[n_1]$ is negative[1], meaning the corresponding modes are amplified in the region $x \in [L_G, L]$ in the absence of the gain. These unphysical solutions can be dropped safely in our analysis, and Eq. (8.2) can be rewritten as

$$\frac{1}{n_2}\tan(\theta_2 + n_2 k\, x_0) + \frac{1}{n_1}\tan(\theta_1 + n_1 k\,(a - x_0)) = 0. \tag{8.5}$$

Conventional modes and surface modes

Eq. (8.5) has two distinct sets of solutions at large k. The first set can be approximated by expanding the above equation to the zeroth order of n_i (etc., $n_2 = n_1$ and $\theta_2 = \theta_1$) except in the term $n_2 k\, a$), which gives the equally spaced frequencies

$$k = \frac{m\pi}{n_1 a}, \quad m = 0, 1, 2, ... \tag{8.6}$$

They are determined by the properties of the cavity (n_1 and a) only and resemble the passive cavity modes. For this reason we will refer to them as the conventional modes.

[1] $\mathrm{Re}[n_1]$ is assumed to be real

Their mode profiles (see Fig. 8.3(a)), however, look different from those of the passive cavity modes as they are amplified in the gain region. The corresponding solution of n_i can then be shown to be

$$n_i = -\frac{n_1}{m\pi}\frac{a}{x_0}\ln(\frac{n_1+1}{n_1-1}) < 0. \tag{8.7}$$

Its absolute value, which is proportional to the corresponding lasing threshold, decreases when the gain region is extended, or if the light confinement is enhanced (larger n_1) as one expects.

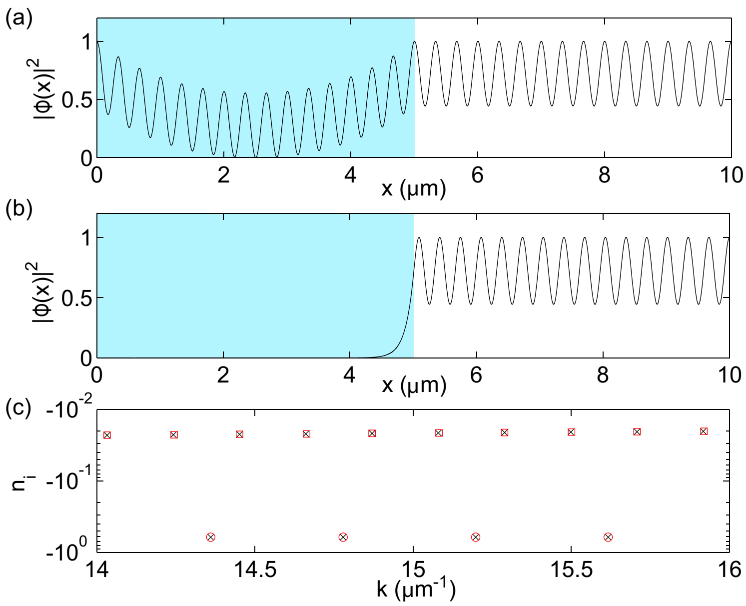

Figure 8.3: (a) Mode profile of a conventional mode ($k = 6.2886\,\mu m^{-1}$, $n_i = 0.0511$) in a one-dimensional cavity of length $a = 10\,\mu m$ and index $n = 1.5$. It is amplified symmetrically in the gain medium, which resides in the left half of the cavity (light blue region). (b) Mode profile of a surface mode ($k = 6.4013\,\mu m^{-1}$, $n_i = -0.6124$) localized inside the right edge of the gain regime. (c) The conventional modes (squares) and surface modes (circles) with $k \in [14\,\mu m^{-1}, 16\,\mu m^{-1}]$. The crosses are the approximations given by Eq. (8.6-8.9). The spacing of the conventional modes is defined by the whole cavity while the larger spacing of the surface modes is defined by the gain-free region.

The other set of solutions, which we will refer to as the surface modes (see Fig. 8.3(b)), have larger $|n_i|$'s , which makes $\tan(\theta_2 + n_2 k\, x_0)$ approximately $-i$ when $|n_i|kx_0 \gg 1$. In this limit n_i is independent of x_0:

$$n_i = (1 - n_1)\sqrt{n_1} < 0, \tag{8.8}$$

and the lasing frequencies

$$k = \frac{m\pi + \arctan(\sqrt{n_1})}{n_1\,(a - x_0)}, \quad m = 0, 1, 2, ... \tag{8.9}$$

are also equally spaced. If these frequencies were associated with the effective cavity formed by the two sides of the gain region, δk would be proportional to the length of the gain region x_0, not the length of the gain-free region $(a - x_0)$ as shown in Eq. (8.9). We will come back to the origin of these modes later in this discussion. The surface modes can be hard to find numerically if we solve Eq. (8.2) instead of Eq. (8.5). We know that $\sin(\alpha)$ and $\cos(\alpha)$ are not truly infinite unless $abs(\mathrm{Im}[\alpha]) \to \infty$, but the computer treats them as infinite if $abs(\mathrm{Im}[\alpha])$ is large enough that $\exp(-|\mathrm{Im}[\alpha]|)$ falls below the machine precision β. When this happens, the Jacobian of the left hand side of Eq. (8.2) becomes zero (here α is $(\theta_2 + n_2 k x_0)$) and it is impossible for the numerical solver to converge. If we assume $\beta = 10^{-30}$, $|\mathrm{Im}[\alpha]|$ only needs to be larger than 35 to make this happen, which translates to $k > 5\,\mu m^{-1}$ in the case where $n_1 = 1.5$ and $x_0 = 10\,\mu m$. In Eq. (8.5), however, the argument of the second term has an imaginary part of $\frac{1}{2}\ln(\frac{n_1+1}{n_1-1})$, which makes it immune of this problem unless $(n_1 - 1) \sim \beta$.

Interaction of conventional modes and surface modes

Fig. 8.3(c) shows $\{k, n_i\}$ of the two set of modes in a cavity of length $a = 10\,\mu m$ and index $n = 1.5$. In this case the thresholds of the surface modes are orders of magnitude larger than the conventional modes unless k is minute, which explains why the former have never been observed in experiments with a similar setup. If we fix the observation window of k and decrease the index of the cavity n_1, the thresholds of the conventional modes increase slowly (logarithmically) while those of the surface modes decreases much faster (super-linearly), and eventually they meet each other in the (k, n_i) plane. When this happens, the modes near the crossing point interact strongly, and the approximations 8.7

and 8.8 are no longer good. The strong interaction leads to the vanishing of a subset of the conventional modes and the surface modes (see Fig. 8.4 and 8.5), which changes the mode spacing dramatically.

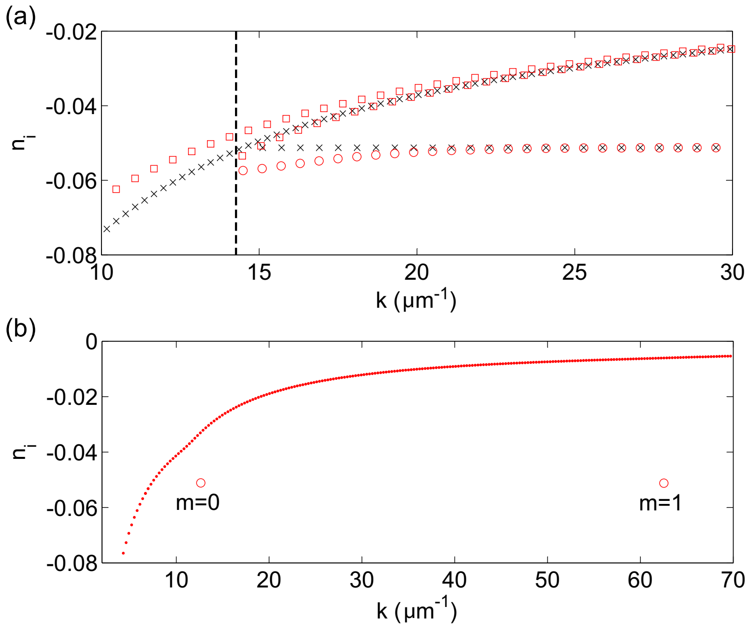

Figure 8.4: (a) Conventional modes (squares) and surface modes (circles) with $k \in [10\,\mu m^{-1}, 30\,\mu m^{-1}]$ in a one-dimensional cavity of length $a = 10\,\mu m$ and index $n = 1.05$. The gain medium (light blue region) resides in the left half of the cavity ($x_0 = 5\,\mu m$). A subset of the conventional modes vanish with the surface modes below the transition frequency $k_t \approx 14\,\mu m$ (dashed line). The crosses are the approximations given by Eq. (8.6-8.9). (b) Similar to (a) but with $x_0 = 9.94\,\mu m$ and squares replaced by dots for clarity. The surface modes (with the m=0 and m=1 ones shown) are far enough from the conventional modes that their interaction is negligible.

The way the two sets of modes interact depends on the ratio x_0/a. Fig. 8.4(a) shows the $x_0/a = 0.5$ case, where the vanishing of the modes happens as soon as the thresholds of the conventional modes and surface modes become close. Just beyond the transition frequency k_t we see pairs of conventional mode and surface mode whose wavelengths are very close to each other. n_i's of the conventional modes oscillate around the values given by the monotonically decreasing function of k given by Eq. (8.7), and higher order terms of n_i in Eq. (8.5) need to be considered to capture this modulation. If we gradually increase the length of the gain region to cover the whole cavity, the frequencies of the conventional modes stay at the values given by Eq. (8.6) with small shifts, while the frequencies of the surface modes blue-shift systematically to infinity with increasing spacings (Fig. 8.4(b)). In this process the thresholds of the surface modes barely change, and when the first possible surface mode (m=0 in Eq. (8.9)) shifts to a k value large enough that its threshold is again much higher than those of the nearby conventional modes, the interaction between the two sets of mode is negligible as we expect from a cavity with an almost homogeneous gain medium. For other values of x_0/a, for example $x_0/a \approx 0.415$ in Fig. 8.5, there is a transition region where the conventional modes and surface modes interact strongly, and the modes in this regime can disappear and then appear at a nearby k value when the ratio changes slightly. This behavior is very similar to that of the abnormal modes found in Ref. [64], and we believe they share the same origin.

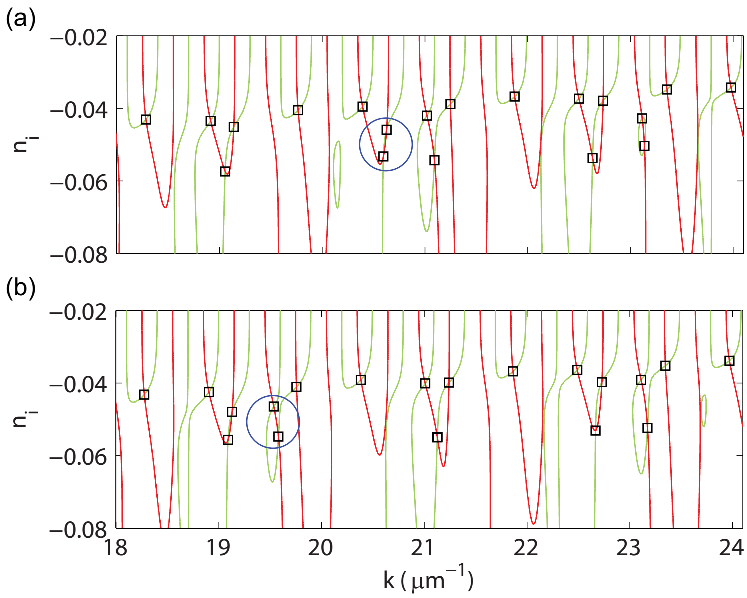

Figure 8.5: Lasing modes (squares) in the transition region $k \in [18\,\mu m^{-1}, 24.1\,\mu m^{-1}]$ when $x_0 = 4.149\,\mu m$ (a) and $x_0 = 4.158\,\mu m$ (b). The cavity is the same as described in the caption of Fig. 8.4. While most of the modes are stable when x_0 is slightly changed, the two modes near $k = 20.6\,\mu m^{-1}$ disappears and two new modes appear near $k = 19.5\,\mu m^{-1}$. The green and red lines are the zeros of the real and imaginary part of the left hand side of Eq. (8.2), respectively.

Uniform curves and x_0-dependency

To see why the interaction between the conventional modes and surface modes depend on the ratio x_0/a, we formulate Eq. (8.5) in a different way. For a given cavity index n_1, Eq. (8.5) has four variables: n_i which is proportional to the threshold, the lasing frequency k, the cavity length a and the length of the gain region x_0. So far we have been considering varying x_0 with a fixed a and looking for the pairs of solutions $\{k, n_i\}$. In fact, by introducing the dimensionless quantities $S = x_0/a$ and $P = kx_0$, we not only reduce the number of unknowns by one (the other unknown quantity is n_i) and can also derive an equation for just P and n_i (assuming n_1 is real):

$$\mathbf{Im}\left\{\arctan\left[\frac{n_1}{n_2}\tan(\theta_2 + n_2 P)\right]\right\} = -\frac{1}{2}\ln\left(\frac{n_1+1}{n_1-1}\right), \tag{8.10}$$

where n_2 and θ_2 are functions of n_1 and n_i as defined before. Since this equation doesn't depend on S, it gives a set of "universal curves" (see Fig. 8.6) on which the data shown in Fig. 8.4 and Fig. 8.5 should fall. Notice the horizontal axis in Fig. 8.6 is now P instead of k, and we see how the conventional modes (the upper side of the open curve) meet the surface modes (the lower side of the open curve) and form closed loops at small P. The gaps between the curves means that for a given length of the gain medium there are "dead zones" where no lasing modes can exist no matter what the length of the cavity is.

To have a better understanding of our origin problem in which x_0 is varied while a is kept fixed, we want to project the solutions of Eq. (8.5) to the $\{S, ka(= P/S)\}$ plane. This can be done by repeatedly solving Eq. (8.5) with different S's, but here we will use a more clever method. By substituting n_i and P by the points on the universal curves, we can immediately calculate the corresponding value of S by

$$S^{-1} = 1 + \frac{m\pi - \theta_1 - \arctan\left[\frac{n_1}{n_2}\tan(\theta_2 + n_2 P)\right]}{n_1 P}, \tag{8.11}$$

which is also derived from Eq. (8.5) and the results are families of complex curves above the $\{P, n_i\}$ plane. We can then easily map these curves to the $\{S, ka\}$ plane which is shown in Fig. 8.7. This is the analogy of the level diagram under the influence of an

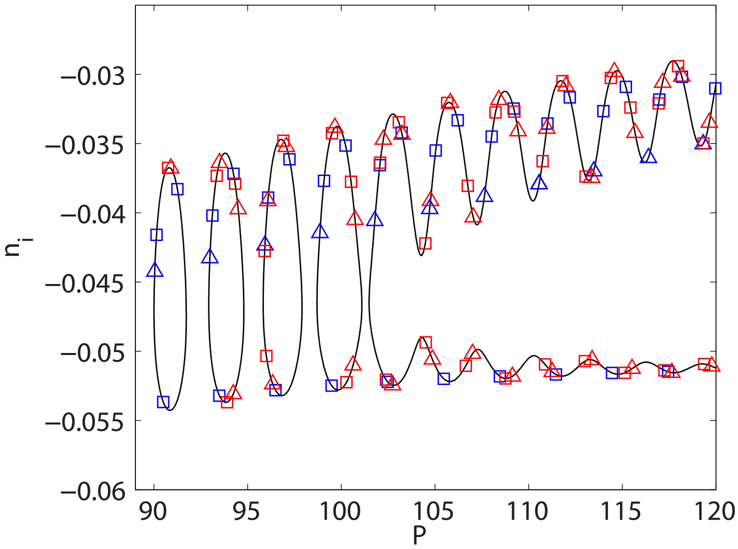

Figure 8.6: Universal curves of the solutions $\{P(\equiv kx_0), n_i\}$ given by Eq. (8.10). The symbols represent the data from Fig. 8.4 (blue squares: $x_0 = 5\,\mu m$, blue triangles: $x_0 = 9.94\,\mu m$) and Fig. 8.5 (red squares: $x_0 = 4.149\,\mu m$, red triangles: $x_0 = 4.158\,\mu m$).

external parameter in the study of resonances/eigenmodes in complex mesoscopic billiards and optical cavities [122, 123], but now in an active system with the external parameter being the ratio of the length of the gain medium to the cavity length. The conventional modes and surface modes have continuous levels at large ka even at their intersections. The conventional modes are insensitive to the change of x_0 as given by Eq. (8.6), so the corresponding levels are horizontal (one of them is highlighted by the green curve in Fig. 8.7(a)). The levels of the surface modes have a positive slope (blue tilted lines) reflecting the blue-shift of surface mode frequencies as x_0 increases given by Eq. (8.9). Both types of levels become broken right at their crossings when ka is small (Fig. 8.7(b)). As a consequence, a pair of conventional mode and surface mode become degenerate 1) right before they disappear when S moves into the gap and 2) right after they appear when S moves out of the gap. This explains why the frequencies of the vanishing pairs of modes are very close as seen in Fig. 8.4(a). Since the crossings don't line up vertically, the disappearing and appearing can happen simultaneously for difference pairs of modes as shown in the circles in Fig. 8.7(c). In some special cases the crossings are almost vertically aligned as the one shown in Fig. 8.7(b), and a subset of the conventional modes and the surface modes disappear altogether below the level corresponding to the transition frequency k_t.

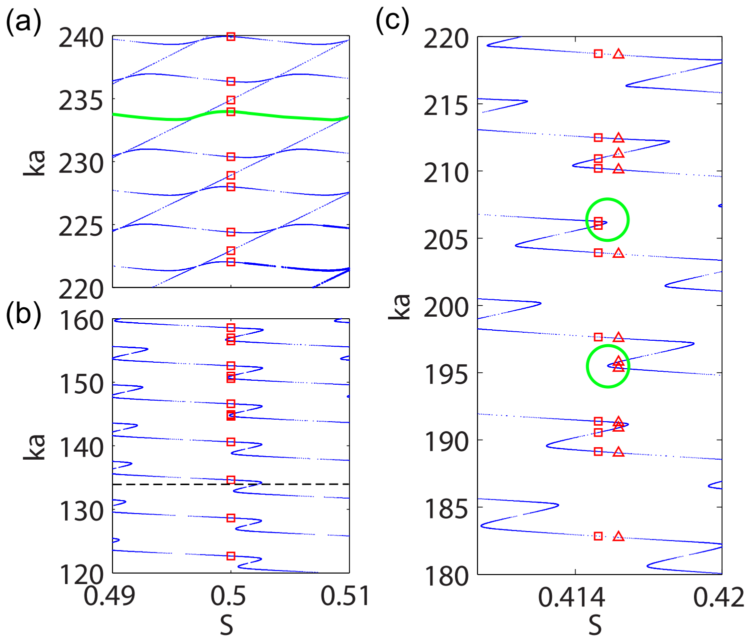

Figure 8.7: Level diagram of a one-dimensional cavity near $S = 0.5$ (a)(b) and $S = 0.415$ (c). In (a) and (b) the red squares are the solutions shown in Fig. 8.4(a), and we see again a subset of conventional modes disappear with the surface modes below the level corresponding to the transition frequency k_t (dashed line in (b)). Panel (c) shows the change of the solutions of when S increases from 0.4149 to 0.4158, and the green circles highlight the region where a pair of surface mode and conventional mode disappear near $ka = 206$ and another pair appear near $ka = 195$.

Surface mode and resonant scattering

The dramatic difference of the mode profiles of the surface mode and the conventional mode inside the gain medium (Fig. 8.3(a) and (b)) can be viewed as a consequence of having different total reflection coefficient r_2 at the right edge of the gain region. The mode profile in the gain region can be decomposed into two amplified waves traveling in opposite directions: $\phi(x) = a_> \exp(i(n_1 + in_i)k(x - x_0)) + a_< \exp(-i(n_1 + in_i)kx)$, where

$a_{>,<}$ are the maximal amplitudes of these two components. Their ratio

$$\left|\frac{a_>}{a_<}\right| = |r_1|\exp(-n_i P) = \sqrt{\left|\frac{r_1}{r_2}\right|} \tag{8.12}$$

determines how symmetric the mode profile is. In the last step we used the round trip phase and amplitude condition inside the gain region $r_1 r_2 \exp[2i(n_1 + in_i)P] = 1$. Now we see the surface modes must have very small $|r_2|$ to have the highly asymmetric profile inside the gain region. This can be achieved if the lasing frequency is close to the resonant scattering frequency of the structure on the right side of the gain region, here a dielectric block of length $(a - x_0)$ and index n_1 (see Fig. 8.8).

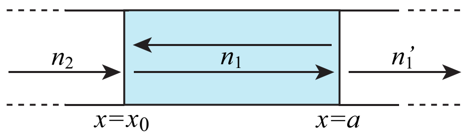

Figure 8.8: Schematic diagram of resonant scattering in a dielectric block.

Normally for such a block connecting two semi-infinite media of index n_2 and $n_1' = 1$, the resonant scattering condition requires either the system is symmetric or $n_2 = n_1^2$ in the absence of gain or loss. In both cases the reflection coefficients at the two sides of the block are the same. But if the materials have loss or gain, the resonant scattering can happen for refractive indices with arbitrary real parts. For example, if n_1 is real as in our system and $\mathrm{Im}[n_2] \neq 0$, the resonant scattering condition requires

$$(\mathrm{Im}[n_2])^2 = (\mathrm{Re}[n_2] - 1)(n_1^2 - \mathrm{Re}[n_2]), \tag{8.13}$$

which gives exactly the same result given by Eq. (8.8) when $\mathrm{Re}[n_2]$ is taken to be the same as n_1. It follows that the resonant scattering frequencies are also the same as given by Eq. (8.9). In fact, although the approximation we used to derive Eq. (8.8) $|\mathrm{Im}[n_2]|kx_0 \gg 1$ doesn't require the gain region to be much longer than the gain-free region $(x_0 \gg (a-x_0))$ if the wavelength is already much shorter than the latter, it is certainly satisfied when this condition is meet. Under this condition the laser cavity shown in Fig. 8.2 is equivalent to the single block structure considered here *if* the wave in the gain region is dominantly right-traveling. Thus we see that the mechanism leading to the surface modes arises from a coherent effect involving the gain-free region, it is not surprising that the spacing of the surface modes is inversely proportional to $(a - x_0)$ rather than the length of the "effective cavity" x_0. This argument also explains why we don't see any surface states localized at the left side of the gain region which requires $|r_1| \ll |r_2|$. Since r_1 is determined simply by the index contrast of the gain region and the environment (air), it cannot be very small due to the reflection from the imaginary part of the index of the gain medium. But one needs to be careful when plotting the mode profile of surface modes with large $|n_1 k x_0|$. Although the extremely small amount of reflection from the right side of the gain region is amplified while traveling to the left, its amplitude should still be very small when it reaches the left side of the cavity. However, since the reflection coefficient at the resonant scattering frequencies can be smaller than the machine precision β and the amplification $\exp(-n_1 k x_0)$ may be larger than β^{-1}, one may find their product to be very large numerically, which gives the illusion that the surface states can localize on the left side of the gain region.

Coupling of surface modes

Instead of having the gain medium in the left part of the cavity, if now we assume that the gain region sits in the center of the cavity and we want to ask whether there are any surface states that are determined cooperatively by the two gain-free regions or "cross talks" between the surface modes localized on the left and on the right side of the gain region. From Eq. (8.12) we know that if the resonance frequencies of the left and right gain-free regions don't coincide, then there doesn't exist surface modes which localize on both sides of the gain region and the frequencies of the surface modes localized on either side don't change. When the two resonance frequencies do coincide, for example, in the case that the gain region is placed right in the center, then we see these double localized surface modes with either even or odd parity. But in this case since the amplitude of the wave function at the center is vanishingly small, the energy (lasing frequencies) of the modes with different parities are almost identical; they appear as a quasi-degenerate pair in the $k - n_i$ plane (see Fig. 8.9). This is different from the conventional modes, whose wave numbers differ by 1/2 for two successive ones of odd and even parities. If we reduce the length of the gain region while keeping the widths of the gain-free regions fixed, eventually the surface modes disappear as the necessary condition $|n_i|kx_0 \gg 1$ is no longer satisfied.

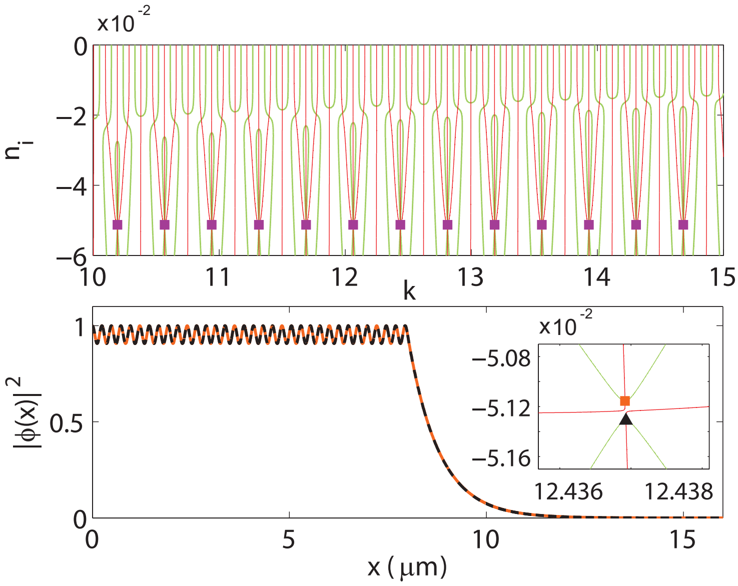

Figure 8.9: (a) TLM solutions of a one-dimensional slab cavity of length $a = 32$ with a gain region of length $x_0 = 16$ sitting in the center. The squares are the predicted value given by Eq. (8.8), which are quasi-degenerated pairs of different parities. The green and red lines are the zeros of the real and imaginary part of the left hand side of Eq. (8.2), respectively. (b) Spatial profiles of the TLMs close to $k = 12.437$ in the left half of the cavity. Inset: The quasi-degenerated TLMs solutions of even (black) and odd (orange) parities.

As a conclusion, we showed in this chapter that interference effect due to the scattering from the gain boundaries gives rise to new modes other than the cavity modes of the passive system. Our analysis is done in a 1D cavity with uniform index, but similar phenomenon is also found in random systems [64, 67]. These new modes generally have much higher thresholds than the conventional modes, but their differences become small when the index of the cavity is reduced. Possible applications of these modes are under investigation.

Chapter 9

Conclusion and open questions

In this thesis we have presented the Steady-state Ab Inito Laser Theory (SALT) developed from the previous work [52] done in our group, and we have demonstrated its applications to lasers in various geometries. Four journal papers based on the SALT have been published [62, 63, 65, 66] and five related works [67, 106, 124, 125, 126] are under preparation.

Starting with the semiclassical Maxwell-Bloch (MB) equations, a set of self-consistent equations have been derived using two approaches *without* invoking the slowly varying envelope approximation (SVEA). In the first approach the effect of the gain medium is shown to add a complex dielectric function to that of the passive cavity, and the time-independent SALT equation (SALT I) takes the form of a second-order self-consistent differential equation; in the second approach the polarization of the gain medium is treated as the source of the Helmholtz equation the electric field satisfies, and a Green's function is employed to invert this equation, leading to a self-consistent integral equation (SALT II), equivalent to SALT I. The full nonlinear lasing modes and their frequencies are the output of the SALT, and they bear no *a priori* relationship to the passive cavity modes and frequencies. In both SALT equations the nonlinearity of the gain medium is treated to the infinite order; the widely used third order theory was shown to fail badly. The Bloch equations describing single lasing transition are generalized to include multi-level lasing schemes, which can be formulated as a two-level problem using a pump-dependent transverse relaxation rate.

The constant-flux (CF) state and the gain-region CF (GRCF) states have been defined inside the last scattering surface of arbitrary shape, and two interpretations of their orthogonality relation are discussed. The differences and relationship of the CF states and the quasi-bound (QB) states, used in standard cavity analysis, are highlighted. The basis consisting of CF states is used to expand the SALT equations, which leads to a map for the complex expansion coefficients. The fixed points of this map give the lasing states, and stable algorithms for finding the fixed points of this nonlinear map are developed. At threshold this map reduces to a linear eigenvalue problem parameterized by the frequency k. When k is tuned to a set of discrete values, the inverse of the corresponding eigenvalue of the threshold matrix gives the lasing threshold in the absence of modal interaction; these k values are the corresponding lasing frequencies. The SALT equations are shown to be basis-independent using the example of a 1D cavity with a non-uniform gain profile; the thresholds, modal intensities and thresholds are found to be identical in the CF basis and in the GRCF basis.

In the nonlinear above threshold calculation, the threshold matrix is generalized to include spatial hole burning, and it is a powerful tool to monitor the modal interactions even of modes *below their thresholds*. Two algorithms are introduced to solve the full nonlinear SALT, using either an simple iterative method or the standard nonlinear solver in MatLab. The convergence of the former is illustrated using a simple 1D cavity, and the integration of these algorithms with the interacting threshold matrix is discussed. Using these algorithms we have explored various properties in simple 1D cavities, which are verified quantitatively by comparing them to the result of brute-force numerical simulations. Excellent agreement is achieved in the regime where the stationary inversion approximation is valid, and the SALT is shown to be much more efficient. We have presented a perturbative approach to include non-stationary inversions at the beating frequencies of nearby lasing modes. Its prediction for the shifts of higher thresholds in a three mode case is found to be in qualitative agreement with the numerical simulations.

We have calculated the CF states in various geometries, which are essential in solving the nonlinear SALT equations in many cases. In 1D Fabry-Perot and DFB lasers, the CF states are found using either a discretization method or a transfer matrix method. In 2D the former is generalized with a special treatment of the outgoing boundary condition; its accuracy is verified using a microdisk laser where analytical results are available. We have applied this method to 2D random lasers and asymmetric resonance cavity (ARC) lasers, including quadruples and limaçons. Using these calculated CF states, we have discussed possible mechanisms of the mode selection in a quadrupole cavity at deformation $\epsilon = 0.16$. When the pump power is increased above threshold, both the spectrum and the far-field emission pattern are found to be in qualitative agreement with the experimental data reported in Ref. [14]. The SALT also predicts the observed quasi-exponential growth of the peak output power when the deformation is increased. In random lasers, modeled as a disk-shaped gain region containing an aggregate of sub-wavelength particles, the CF states are found to be statistically similar to the QB modes, but there is no one-to-one correspondence between them when the main free path is comparatively long. Strong modal interactions are observed in both the diffusive regime and the quasi-ballistic regime, which leads to frequency repulsion and even non-monotonic variation of modal intensities in the latter case. Lasing frequencies are found to be stable when a white noise is added to the pump, while modal intensities fluctuate strongly. The pump induced directionality is studied, which could lead to possible applications of the random laser.

We have pointed out that the scattering from the gain boundaries in a low-Q laser with a spatial inhomogeneous gain profile can lead to non-conventional modes. Such modes are found for a 1D edge-emitting laser, and their relationship with the resonance tunneling in the gain-free region has been demonstrated. These new modes localize on the gain side of the gain/gain-free interface, and their interactions with the conventional cavity modes are investigated when the gain boundary is shifted.

Although we have explored many aspects of the SALT, there are still a few questions we would like to investigate further. One of them is the vectorial generalization of the SALT equations. The preliminary results have been given in Section 2.2, but how to calculate the CF states in 3D for an arbitrary $\epsilon_c(\boldsymbol{x})$ remains an challenge. Another question is whether a more effective method to calculate the GRCF states can be developed, which will facilitate the exploration of the gain-induced non-conventional modes in dimensions other than 1D. So far we haven't considered the noise due to spontaneous emission. Within the framework of the semiclassical theory, whether a Langevin type stochastic noise term can be integrated in the SALT needs to be studied. Entering the regime of quantum optics, it is still unclear what are the correspondences of the CF states. For each lasing mode at the external frequency k, there exist an infinite number of CF states with complex wavevectors $\{k_m\}$. Whether one can associate creation operators for CF states with cavity photon states requires further investigation. A generalization to operator electromagnetic fields is necessary to understand fundamental properties such as the laser linewidth and photon statistics. As for the applications of the SALT, our goals in the near future include predicting the lasing properties in the newly proposed aperiodic deterministic lasers and a further investigation of the quadrupole cavity with more detailed information about the spatial pump profile.

Appendix A

Analytical approximations of CF frequencies in a 1D uniform index laser

In Section 3.2 we showed that in a 1D laser cavity with uniform index there is a CF frequency close to a given QB frequency $\tilde{k}_m$ when the external frequency is close to $\mathrm{Re}[\tilde{k}_m]$. This behavior is shown to be robust for all the QB frequencies in the one-dimensional case in Ref. [52] where a first order approximation is given for each k_m at the specified external frequency $k = \mathrm{Re}[\tilde{k}_m]$. In this appendix we derive a similar result using a different approach which can be easily generalized to include higher order corrections.

For simplicity, we take $n_2 = 1$ outside the cavity and n_1 to be real inside the cavity, and drop the subscript of the latter. We first take the logarithm of Eq. (3.7) and use $\exp(2ink)|_{k=\mathrm{Re}[\tilde{k}_m]} = -1$, which gives

$$i(m + 1/2)\pi(1 + \epsilon_m) = i(m + 1/2)\pi + \frac{1}{2}\ln(\frac{1 + \frac{1}{n} + \epsilon_m}{1 - \frac{1}{n} + \epsilon_m}). \tag{A.1}$$

ϵ_m is defined as the ratio $n_1 k_m / n_2 k$ in Section 3.2. The complex branch of the logarithm on the $r.h.s$ is chosen to be consistent with the QB solutions, and ϵ is defined by $(k_m - \tilde{k}_m)/\tilde{k}_m$.

By expanding the second term on the $r.h.s$ to the first order of ϵ_m

$$\ln(\frac{1+\frac{1}{n}+\epsilon_m}{1-\frac{1}{n}+\epsilon_m}) \approx \frac{1}{2}\ln(\frac{n+1}{n-1}) - \frac{n}{n^2-1}\,\epsilon_m \tag{A.2}$$

and solving for ϵ_m, we obtain

$$\epsilon_m^{(1)} \approx \frac{\ln(\frac{n+1}{n-1})}{\frac{2n}{n^2-1}+i(2m+1)\pi}. \tag{A.3}$$

To compare the result with that given in Ref. [52], we note

$$\begin{aligned} \mathrm{Re}\,[k_m]-k &= \mathrm{Re}\,[\epsilon_m]\,k \\ &= \ln(\frac{n+1}{n-1})\frac{\frac{2n}{n^2-1}}{(\frac{2n}{n^2-1})^2+(2nka)^2}k. \end{aligned} \tag{A.4}$$

In the limit $ka \gg \frac{1}{n^2-1}$ the first term in the denominator can be neglected which leads to Eq. (A11) in Ref. [52]. The difference of the imaginary parts of the CF and QB frequencies is given by

$$\begin{aligned} \mathrm{Im}\,[k_m]-\mathrm{Im}\left[\tilde{k}_m\right] &= \mathrm{Im}\left[\epsilon_m^{(1)}\right]k-\mathrm{Im}\left[\tilde{k}_m\right] \\ &= \ln(\frac{n+1}{n-1})\frac{1}{2na}\frac{1}{1+(n^2-1)^2k^2a^2} \\ &\approx \frac{\ln(\frac{n+1}{n-1})}{2n(n^2-1)^2k^2a^3}, \end{aligned} \tag{A.5}$$

Compared with Eq. (A12) in Ref. [52], Eq. (A.5) is smaller by a factor of $[1+\ln(\frac{n+1}{n-1})]$, which is about 1.55 if $n=2$. To increase the precision of the approximation we expand Eq.(A.2) to $o(\,(\epsilon_m^{(1)})^2)$

$$\ln(\frac{1+\frac{1}{n}+\epsilon_m^{(1)}}{1-\frac{1}{n}+\epsilon_m^{(1)}}) \approx \ln(\frac{n+1}{n-1}) - \frac{2n}{n^2-1}\,\epsilon_m^{(1)} + \frac{2n^3}{(n^2-1)^2}\,(\epsilon_m^{(1)})^2, \tag{A.6}$$

and the second order approximation of ϵ_m is given by

$$\begin{aligned} \epsilon_m^{(2)} &= \frac{1}{i(2m+1)\pi}\left(\ln(\frac{n+1}{n-1}) - \frac{2\,n}{n^2-1}\,\epsilon_m^{(1)} + \frac{2\,n^3}{(n^2-1)^2}\,(\epsilon_m^{(1)})^2\right) \\ &= \epsilon_m^{(1)} + \frac{1}{i(2m+1)\pi}\frac{2\,n^3}{(n^2-1)^2}\,(\epsilon_m^{(1)})^2. \end{aligned} \tag{A.7}$$

In Fig. A.1 we compare the first- and second-order results with the numerical values of ϵ_m. The first order approximation works quite well for the real parts of the complex CF frequencies, but a higher order approximation is required for the imaginary parts requires to achieve a comparable accuracy. Besides the k-dependence of the difference of the corresponding CF and QB frequencies shown in Fig. A.1, Eq. (A.4) and (A.5) also tell us that the difference becomes small when n is large. Since the first lasing mode in this simple one-dimensional system is a CF state, this finding partially explains why it is a good approximation to take QB modes in a high-Q cavity as the lasing modes.

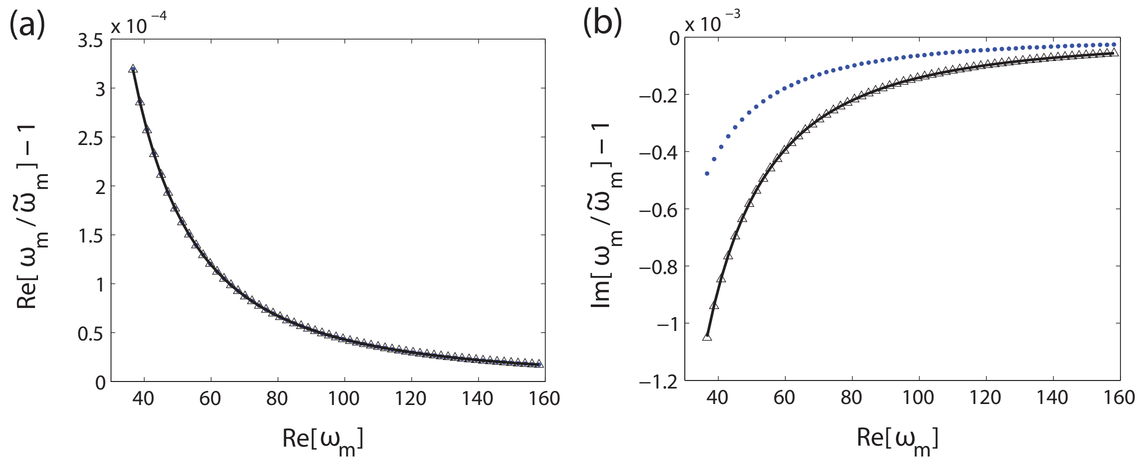

Figure A.1: Differences of the CF and QB frequencies in a 1D edge-emitting cavity as a function of the real part of the QB frequency. The refractive index is $n = 2$. (a) The real parts of the frequencies, and (b) the imaginary parts. In both plots, the solid-lines represent the numerical results, the triangles represent the second order result (Eq. (A.7)) and the dotted lines represent the first order result (Eq.(A.3)). In Fig. A.1(a) the dotted line is so close to the other two that it can hardly be seen.

In fact a global approximation for all k_m at the *same* external frequency k is possible based on the observation that $\varsigma_m' = (k_m/\tilde{k}_m) - 1$ is small for all m's when k is large (see

Fig. A.2(a)). We start by rewriting Eq. (A.2) as

$$nk_m a = (1+\varsigma_m')\tilde{Z}_m = (m+\frac{1}{2})\pi - \frac{i}{2}\ln\frac{n'(1+\varsigma_m')+1}{n'(1+\varsigma_m')-1}, \tag{A.8}$$

in which $\tilde{Z}_m \equiv n\tilde{k}_m a$ and $n' \equiv \frac{\tilde{Z}_m}{k}$. Compared with our previous approach in Section 2.4, the zeroth order expansion of Eq. (A.8) gives a complex ς_m', which leads to a correction to both the real and imaginary parts of the CF eigenvalues

$$\varsigma_m'^{(0)} = \frac{\ln\frac{(n'+1)(n-1)}{(n'-1)(n+1)}}{2i\tilde{Z}_m} = \frac{\ln\frac{(n\frac{\tilde{k}_m}{k}+1)(n-1)}{(\frac{n\tilde{k}_m}{k}+1)(n-1)}}{i(2m+1)\pi + \ln\frac{n-1}{n+1}}. \tag{A.9}$$

It works well for large m's as one can see in Fig. A.2. For small m's the $\tilde{Z}_m$ is of the order of 10^1 and the first order correction needs to be considered

$$\varsigma_m'^{(1)} = \frac{\ln\frac{(n'+1)(n-1)}{(n'-1)(n+1)}}{2i\tilde{Z}_m + \frac{2n'}{n'^2-1}}, \tag{A.10}$$

or equivalently

$$\varsigma_m'^{(1)} = \frac{\ln\frac{(n'+1)(n-1)}{(n'-1)(n+1)} - \frac{2n'}{n'^2-1}\varsigma_m'^{(0)}}{2i\tilde{Z}_m} \tag{A.11}$$

by expanding the denominator of Eq. (A.10). $\varsigma_m'^{(2)}$ can be obtained similarly to how we derived $\varsigma_m^{(2)}$ in in Section 2.4

$$\varsigma_m'^{(2)} = \frac{\ln\frac{(n'+1)(n-1)}{(n'-1)(n+1)} - \frac{2n'}{n'^2-1}\varsigma_m'^{(1)} + \frac{2n'^3}{(n'^2-1)^2}\varsigma_m'^{(1)^2}}{i\tilde{Z}_m}. \tag{A.12}$$

The first order approximation (A.11) and second order approximation (A.12)) work exceptionally well for the CF eigenvalues away from the "valley" of the spectrum. The m-dependent index n' becomes close to unity in the valley, and the small quantity $\varsigma_m'/(n'^2-1)$ is no longer tiny (though in most cases it is still smaller than 1) which prevents higher order corrections from converge quickly.

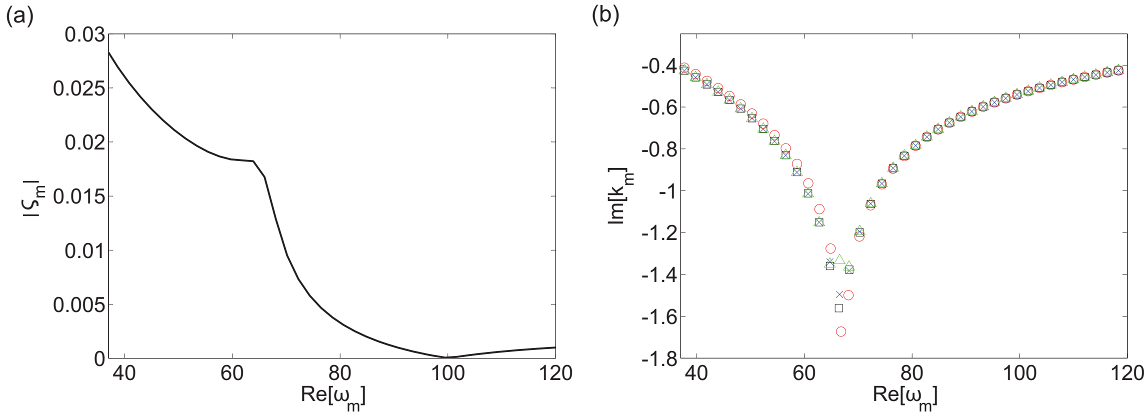

Figure A.2: (a) $\varsigma'_m \equiv k_m/\tilde{k}_m - 1$ as a function of Re$[k_m]$. ς'_m reaches its minimum at Re$[k_m] \sim k \sim$ Re$[\tilde{k}_m]$ and is larger on the left of the valley due to the phase shift of Re$[k_m]$ from half integer times of π to integer times of π. (b) CF eigenvalues (blue crosses) and their approximation values: 0th order (red circles), 1st order (black squares) and 2nd order (green triangles).

Appendix B

Orthogonality of GRCF states in multi-layer 1D cavities

In this appendix we prove the orthogonality of the GRCF states in the multi-layer case shown in Fig. B.1. We choose to have $2p$ layers in the cavity for the convenience of labeling the layers, but the result is independent of this choice. The gain medium is distributed uniformly in the odd-number layers of index n_1 and the wavevector is the CF frequency k_m; In the even-number layers the index is n_2 and the wavevector is the same as the external k. The equation that defines the GRCF in this cavity can be written as

$$\begin{cases} (\nabla^2 + n_1^2\, k_m^2)\, \varphi_m(x,\omega) = 0, & x_{2i-2} < x < x_{2i-1}, \\ (\nabla^2 + n_2^2\; k^2)\, \varphi_m(x,\omega) = 0, & x_{2i-1} < x < x_{2i}, \\ (\nabla^2 + \quad k^2 \quad)\, \varphi_m(x,\omega) = 0, & x > a, \end{cases} \tag{B.1}$$

in which $i = 1, 2, 3, ..., p$.

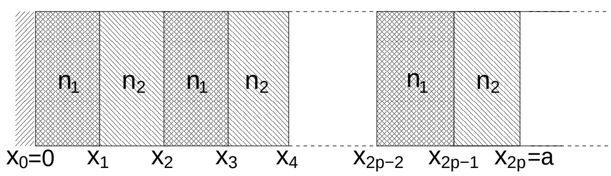

Figure B.1: Schematic of a one-dimensional edge-emitting cavity with alternate layers of refractive index n_1 and n_2.

To prove the orthogonality of the GRCF states, we first consider the following quantity

$$
\begin{aligned}
& (k_m^2 - k_n^2) \int_{x_{2i-2}}^{x_{2i-1}} dx \, \varphi_m(x,\omega) \, \varphi_n(x,\omega) \\
= & \int_{x_{2i-2}}^{x_{2i-1}} dx \, \left[\varphi_m(x,\omega) \nabla^2 \varphi_n(x,\omega) - \varphi_m(x,\omega) \nabla^2 \varphi_n(x,\omega)\right] \\
= & \int_{x_{2i-2}}^{x_{2i-1}} dx \, \nabla \cdot \left[\varphi_m(x,\omega) \nabla \varphi_n(x,\omega) - \varphi_m(x,\omega) \nabla \varphi_n(x,\omega)\right] \\
= & \left[\varphi_m(x,\omega) \frac{\partial \varphi_n(x,\omega)}{\partial x} - \varphi_n(x,\omega) \frac{\partial \varphi_m(x,\omega)}{\partial x}\right]_{x_{2i-2}}^{x_{2i-1}} .
\end{aligned}
\tag{B.2}
$$

In the last step we used the Green's theorem to reduce the integral to the difference of the "cross flux" at the two edges of the gain layers. By summing over the above equations with different i, we have an expression for the overlapping integral of φ_m and φ_n in the gain region

$$
\begin{aligned}
& (k_m^2 - k_n^2) \int_{gain} dx \, \varphi_m(x,\omega) \, \varphi_n(x,\omega) \\
\equiv & (k_m^2 - k_n^2) \sum_{i=1}^{p} \int_{x_{2i-2}}^{x_{2i-1}} dx \, \varphi_m(x,\omega) \, \varphi_n(x,\omega) \\
= & \sum_{i=1}^{p} \left[\varphi_m(x,\omega) \, \frac{\partial \varphi_n(x,\omega)}{\partial x} - \varphi_n(x,\omega) \frac{\partial \varphi_m(x,\omega)}{\partial x}\right]_{x_{2i-2}}^{x_{2i-1}} \\
= & \left[\varphi_m(x,\omega) \, \frac{\partial \varphi_n(x,\omega)}{\partial x} - \varphi_n(x,\omega) \frac{\partial \varphi_m(x,\omega)}{\partial x}\right]_{x_{2p}}^{x_1} \\
& + \sum_{i=2}^{p} \left[\varphi_m(x,\omega) \, \frac{\partial \varphi_n(x,\omega)}{\partial x} - \varphi_n(x,\omega) \frac{\partial \varphi_m(x,\omega)}{\partial x}\right]_{x_{2i-2}}^{x_{2i-1}} \\
= & -\sum_{i=1}^{p} \left[\varphi_m(x,\omega) \, \frac{\partial \varphi_n(x,\omega)}{\partial x} - \varphi_n(x,\omega) \frac{\partial \varphi_m(x,\omega)}{\partial x}\right]_{x_{2i-1}}^{x_{2i}} .
\end{aligned}
\tag{B.3}
$$

In the last but one step we removed the term $[\varphi_m(x,\omega) \, \partial_x \varphi_n(x,\omega) - \varphi_n(x,\omega) \partial_x \varphi_m(x,\omega)]_{x_0}$ using the hard wall boundary condtion at $x = 0$, and added the term $[\varphi_m(x,\omega) \, \partial_x \varphi_n(x,\omega) - \varphi_n(x,\omega) \partial_x \varphi_m(x,\omega)]_{x_{2p}}$ which vanishes because of the outgoing boundary condition we impose at the emitting edge of the cavity. In the gain-free regions we repeating the derivation which leads to Eq. (B.2), and we find all the terms on the $r.h.s$ of Eq. (B.3) vanish:

$$\begin{aligned} 0 &= (k^2 - k^2) \int_{x_{2i-1}}^{x_{2i}} dx \, \varphi_m(x,\omega) \, \varphi_n(x,\omega) \\ &= \int_{x_{2i-1}}^{x_{2i}} dx \, \nabla \cdot [\varphi_m(x,\omega) \nabla \varphi_n(x,\omega) - \varphi_m(x,\omega) \nabla \varphi_n(x,\omega)] \\ &= \left[\varphi_m(x,\omega) \frac{\partial \varphi_n(x,\omega)}{\partial x} - \varphi_n(x,\omega) \frac{\partial \varphi_m(x,\omega)}{\partial x} \right]_{x_{2i-1}}^{x_{2i}}, \end{aligned} \tag{B.4}$$

Therefore, we prove that the GRCF states are orthogonal in the gain regions

$$\int_{gain} dx \, n_1^2 \, \varphi_m(x,\omega) \, \varphi_n(x,\omega) = \delta_{mn} \tag{B.5}$$

with the proper normalization. We remind the reader that the "cross flux" has no physical meaning despite the similarity of its definition to the real flux. Therefore, it is conserved in the gain-free layers (Eq. (B.4)) even in the presence of absorption (a complex n_2).

Appendix C

Spectral method

Instead of directly solving for the CF state as we did in Section 3.4, we can also solve for its Fourier transform coefficients:

$$\varrho_m(r) \equiv \frac{1}{2\pi} \int_0^{2\pi} \phi(r,\theta)\, e^{-im\theta}. \tag{C.1}$$

Substituting Eq. (C.1) into the Helmholtz equation and equating the Fourier coefficients, we have

$$\left(\frac{\partial^2}{\partial r^2} + \frac{1}{r}\frac{\partial}{\partial r} - \frac{m^2}{r^2} \right) \varrho_m(r) + k_I^2 \sum_n \sigma_{m-n}(r)\, \varrho_n(r) = 0. \tag{C.2}$$

$\sigma_n(r)$ is the Fourier coefficients of the spatial dependent dielectric function $\epsilon(r,\theta)$, and n runs from $-M$ to M where M is the absolute value of the cutoff angular momentum. We will direct discretize this equation since we have shown that it leads to the same result of the variational method in Section 3.4. $\varrho_{\mu,\,m} \equiv \varrho_m(r)|_{\,r=r_\mu}$ satisfies

$$\frac{r_{\mu-\frac{1}{2}}\, \varrho_{\mu-1,\,m} + r_{\mu+\frac{1}{2}}\, \varrho_{\mu+1,\,m} - 2\, r_\mu\, \varrho_{\mu,\,m}}{r_\mu (\Delta_r)^2} - \frac{m^2}{r_\mu^2} \varrho_{\mu,\,m} \,+\, k_I^2 \sum_n \sigma_{\mu,\,m-n}\, \varrho_{\mu,\,n} = 0, \tag{C.3}$$

and the boundary condition at $r = R$ is given by Eq. (3.42), or

$$\varrho_{N_r+1,m} = \varrho_{N_r,m} \left(1 + \frac{k\Delta_r H_m^{+'}(kR)}{H_m^{+}(k\, r_{N_r+1}) - k\Delta_r H_m^{+'}(kR)} \right). \tag{C.4}$$

$\{\varrho_{\mu,\,m}\}$'s are obtained by solving the eigenvalue problem

$$H\Phi_I = k_I^2 B\Phi_I. \tag{C.5}$$

We relabel the second subscript of $\varrho_{\mu,\,m}$ by ν and let it run from 1 to $N_m \equiv 2M+1$. H is a tri-diagonal matrix with nonzero elements on the 0 and $\pm N_m$ diagonals with

$$\begin{cases} H_{(\mu-1)N_m+\nu,\,(\mu-1)N_m+\nu} & = \frac{2}{(\Delta_r)^2} + \frac{m^2}{r_\mu^2} \\ & \quad -\delta_{\mu,\,N_r}\frac{r_{\mu+\frac{1}{2}}}{r_\mu(\Delta_r)^2}\left(1+\frac{k\Delta_r H_m^{+'}(kR)}{H_m^+(k\,r_{N_r+1})-k\Delta_r H_m^{+'}(kR)}\right), \\ H_{(\mu-1)N_m+\nu,\,\mu N_m+\nu} & = H_{\mu N_m+\mu,\,(\mu-1)N_m+\nu} = -\frac{r_{\mu+\frac{1}{2}}}{r_\mu(\Delta_r)^2}\,. \end{cases} \tag{C.6}$$

B is a block diagonal matrix

$$B = \begin{pmatrix} \sigma_1 & & & \\ & \sigma_2 & & \\ & & \cdots & \\ & & & \sigma_{N_r} \end{pmatrix}, \tag{C.7}$$

and σ_μ is a $(2M+1)$ by $(2M+1)$ matrix

$$\sigma_\mu = \begin{pmatrix} \sigma_{\mu,\,0} & \sigma_{\mu,\,-1} & \cdots & \sigma_{\mu,\,1-N_m} \\ \sigma_{\mu,\,1} & \sigma_{\mu,\,0} & \cdots & \sigma_{\mu,\,2-N_m} \\ \cdots & \cdots & \cdots & \cdots \\ \sigma_{\mu,\,N_m-1} & \sigma_{\mu,\,N_m-2} & \cdots & \sigma_{\mu,\,0} \end{pmatrix}. \tag{C.8}$$

The eigenvectors

$$\Phi_I = \{\varrho_{1,\,1},\ \varrho_{1,\,2},\ \ldots,\ \varrho_{1,\,N_m},\ \varrho_{2,\,1},\ \varrho_{2,\,2},\ \ldots,\ \varrho_{2,\,N_m},\ \ldots,\ \varrho_{N_r,\,1},\ \ldots,\ \varrho_{N_r,\,N_m}\}^T \tag{C.9}$$

don't necessarily need to be orthogonal since they are not the real space CF states. If $\epsilon(r,\,\theta)$ is symmetric about the x-axis (e.g. limaçon and quadruple cavities), we only need to solve for $\varrho_{m\geq 0}(r)$ $(N_m = M+1)$ and use the parity to determine $\varrho_{m<0}(r)$.

Appendix D

Finding lasing frequencies above threshold in the iterative method

In this appendix we discuss the details of how to implement of the "gauge" condition in finding the non-trivial solutions of Eq. (2.50) above threshold. Suppose that there are Q lasing modes at a given pump strength and we have iterated Eq. (2.50) p times to obtain $\{\boldsymbol{a}^\mu(p)\}$ and $\{k^\mu(p)\}$. To find the Q $k^\mu(p+1)$ we impose the "gauge" condition by solving a set of Q equations:

$$0 = \mathrm{Im}\left[a^\mu_{m_\mu}(p+1)\right] = \mathrm{Im}\left[G^\mu_{m_\mu}(k^1(p+1), k^2(p+1), ..., k^Q(p+1); \{\boldsymbol{a}^\mu(p)\})\right]. \qquad \text{(D.1)}$$

$a^\mu_{m_\mu}$ is largest CF coefficient of the μth mode, and $G^\mu_{m_\mu}$ is the $r.h.s$ of Eq. (2.50) which is now taken a function of $\{k^\mu(p+1)\}$ only; the other quantities in it, including $\{\boldsymbol{a}^\mu(p)\}$, are treated as known quantities. We obtain $\boldsymbol{a}^\mu(p)$ by calculating the real parts of G^μ_m once $\{k^\mu(p+1)\}$ are found. Notice the k-dependence of $G^\mu_{m_\mu}$ comes not only from the prefactor in Eq. (2.50) but also from the k-dependence of the CF basis $\{\Psi^\mu(k^\mu;\boldsymbol{x}), k_m(k^\mu)\}$. Therefore, solving Eq. (D.1) during each iteration can be quite time consuming in the multi-mode regime if there is no analytical expression for $k_m(k^\mu)$ (e. g., in asymmetric resonant cavities lasers).

To speed up each iteration we relax the "gauge" condition by replacing Eq. (D.1) by

$$0 = \mathrm{Im}\left[a^{\mu}_{m_\mu}(p+1)\right] = \mathrm{Im}\left[G'^{\mu}_{m_\mu}(k^{\mu}(p+1); \{k^{\nu\neq\mu}(p), \boldsymbol{a}^{\mu}(p)\})\right], \tag{D.2}$$

in which $G'^{\mu}_{m_\mu}$ is treated as a function of $k^{\mu}(p+1)$ only. Thus the set of Q coupled equations become separate, and it takes much less time to solve them. One can easily check that the fixed points of Eq. (D.1) and Eq. (D.2) are the same. One can further relax the "gauge condition" by drop the the k-dependence of the CF basis which turns Eq. (D.2) into quadratic equation of $k^{\mu}(p+1)$. Once $k^{\mu}(p+1)$ is obtained we calculate $\{\Psi^{\mu}(k^{\mu}(p+1); \boldsymbol{x}), k_m(k^{\mu}(p+1))\}$ and use them in G'^{μ}_{m} for the next iteration.

Bibliography

[1] A. Einstein. Zur quantentheorie der strahlung (on the quantum theory of radiation). *Physika Zeitschrift*, 18:121–128, 1917.

[2] David Larsson. http://www.fotonik.dtu.dk/English/Research/ResearchActivities/NanoDevices_research/VCSELs.aspx.

[3] A. E. Siegman. *Lasers*. University Sience Books, Mill Valley, California, USA, 1986.

[4] T. Suhara. *Semiconductor laser fundamentals*. CRC Press, New York, USA, 2004.

[5] K. Utaka, K. Kobayash, K. Kishino, and Y. Suematsu. $1.5 - 1.6$ μm GalnAsP/InP integrated twin guide lasers with first-order distributed Bragg reflectors. *Electron. Lett.*, 16:455–456, 1980.

[6] K. Utaka, K. Akiba, K. Sakai, and Y. Matsushima. Room-temperature CW operation of distributed-feedback buried-heterostructure InGaAsP/lnP lasers emitting at 1.57 μm. *Electron. Lett.*, 17:961–963, 1981.

[7] J. K. Guenter, R. A. Hawthorne III, D. N. Granville, M. K. Hibbs-Brenner, and R. A. Morgan. Reliability of protonimplanted VCSELs for data communications. *Proc. SPIE*, 2683:102–113, 1996.

[8] Fumio Koyama. Recent advances of VCSEL photonics. *J. Lightwave Technol.*, 24:4502–4513, 2006.

[9] J. Tatum. VCSELs in the information age. *SPIE Optics in Information Newsletter*, April 2001.

[10] A. F. J. Levi, R. E. Slusher, S. L. McCall, T. Tanbunek, D. L. Coblentz, and S. J. Pearton. Electrically pumped, room-temperature microdisk semiconductorlasers with submilliampere threshold currents. *IEEE Trans. Electron Devices*, 39:2651–2651, 1992.

[11] S. L. McCall, A. F. J. Levi, R. E. Slusher, S. J. Pearton, and R. A. Logan. Whispering-gallery mode microdisk lasers. *Appl. Phys. Lett.*, 60:289–291, 1992.

[12] L. Collot, V. Lefevreseguin, M. Brune, J. M. Raimond, and S. Haroche. Very high-q whispering-gallery mode resonances observed on fused-silica microspheres. *Europhys. Lett.*, 23:327–334, 1993.

[13] J. C. Knight, G. Cheung, F. Jacques, and T. A. Birks. Phase-matched excitation of whispering-gallery-mode resonances by a fiber taper. *Opt. Lett.*, 22:1129, 1997.

[14] C. Gmachl, F. Capasso, E. E. Narimanov, J. U. Nöckel, A. D. Stone, J. Faist, D. L. Sivco, and A. Y. Cho. High-power directional emission from microlasers with chaotic resonators. *Science*, 280:1556–1564, 1998.

[15] J. Wiersig and M. Hentshcel. Combining directinal light output and ultralow loss in deformed microdisks. *Phys. Rev. Lett.*, 100:033901, 2008.

[16] O. Painter, R. K. Lee, A. Scherer, A. Yariv, J. D. OBrien, P. D. Dapkus, and I. Kim. Two-dimensional photonic band-gap defect mode laser. *Science*, 284:1819–1821, 1999.

[17] S Noda, A Chutinan, and M Imada. Trapping and emission of photons by a single defect in a photonic bandgap structure. *Nature*, 407:608–610, 2000.

[18] N. M. Lawandy, R. M. Balachandran, A. S. L. Gomes, and E. Sauvain. Laser action in strongly scattering media. *Nature*, 368:436, 1994.

[19] P. Pradhan and N Kumar. Localization of light in coherently amplifying random media. *Phys. Rev. B*, 50:9644, 1994.

[20] S. Qian, J. B. Snow, H. Tzeng, and R. K. Chang. Lasing droplets: Highlighting the liquid-air interface by laser emission. *Science*, 231:486–488, 1986.

[21] A. Mekis, J. U. Nöckel, G. Chen, A. D. Stone, and R. K. Chang. Ray chaos and Q spoiling in lasing droplets. *Phys. Rev. Lett.*, 75:2682–2685, 1995.

[22] S. Chang, R. K. Chang, A. D. Stone, and J. U. Nöckel. Observation of emission from chaotic lasing modes in deformed microspheres: displacement by the stable-orbit modes. *J. Opt. Soc. Am. B*, 17:1828–1834, 2000.

[23] R. K. Chang and A. J. Campillo. *Optical processes in microcavities*. World Scientific, 1996.

[24] D. Rafizadeh, J. P. Zhang, S. C. Hagness, A. Taflove, K. A. Stair, S. T. Ho, and R. C. Tiberio. Waveguide-coupled AlGaAs / GaAs microcavity ring and disk resonators with high finesse and 21.6-nm free spectral range. *Opt. Lett.*, 22:1244–1246, 1997.

[25] F. Vollmer, D. Braun, A. Libchaber, M. Khoshsima, I. Teraoka, and S. Arnold. Protein detection by optical shift of a resonant microcavity. *App. Phys. Lett.*, 80, 2002.

[26] M. Hossein-Zadeh and K. J. Vahala. Fiber-taper coupling to whispering-gallery modes of fluidic resonators embedded in a liquid medium. *Opt. Exp.*, 14:10800–10810, 2006.

[27] J. Hu, N. Carlie, N. Feng, L. Petit, A. Agarwal, K. Richardson, and L. Kimerling. Planar waveguide-coupled, high-index-contrast, high-Q resonators in chalcogenide glass for sensing. *Opt. Lett.*, 33:2500–2502, 2008.

[28] J. U. Nöckel and A. D. Stone. Ray and wave chaos in asymmetric resonant optical cavities. *Nature*, 385:45–47, 1997.

[29] B. Crespi, G. Perez, and S. Chang. Quantum Poincaré sections for two-dimensional billiards. *Phys. Rev. E*, 47:986–991, 1993.

[30] S. Lacey, H. Wang, D. H. Foster, and J. U. Nöckel. Directional tunneling escape from nearly spherical resonators. *Phys. Rev. Lett.*, 91:033902, 2003.

[31] H. G. L. Schwefel, N. B. Rex, H. E. Türeci, R. K. Chang, A. D. Stone, and J. Zyss. Dramatic shape sensitivity of directional emission patterns from similarly defomred cylindrical polymer lasers. *J. Opt. Soc Am. B*, 21:923–934, 2004.

[32] C. Yan, Q. J. Wang, L. Diehl, M. Hentschel, J. Wiersig, N. Yu, C. Pflügl, F. Capasso, M. A. Belkin, T. Edamura, M. Yamanishi, and H. Kan. Directional emission and universal far-field behavior from semiconductor lasers with limaçon-shaped microcavity. *Appl. Phys. Lett.*, 94:251101, 2009.

[33] Itay Shomroni. http://commons.wikimedia.org/wiki/File:Micro_disk_resonator_sem.JPG.

[34] K. Srinivasan and O. Painter. Momentum space design of high-Q photonic crystal optical cavities. *Opt. Exp.*, 10:670–684, 2002.

[35] Y. Akahane, T. Asano, B. Song, and S. Noda. High-Q photonic nanocavity in a two-dimensional photonic crystal. *Nature*, 425:944–947, 2003.

[36] X. Wu, A. Yamilov, X. Liu, S. Li, V. P. Dravid, R. P. H. Chang, and H. Cao. Ultraviolet photonic crystal laser. *App. Phys. Lett.*, 85:3657–3659, 2004.

[37] H. Cao, Y. G. Zhao, S. T. Ho, E. W. Seelig, Q. H. Wang, and R. P. H. Chang. Random laser action in semiconductor powder. *Phys. Rev. Lett.*, 82:2278, 1999.

[38] X. Jiang and C. M. Soukoulis. Time dependent theory for random lasers. *Phys. Rev. Lett.*, 85:70–73, 2000.

[39] H. Cao, Y. Ling, J. Y. Xu, C. Q. Cao, and P. Kumar. Photon statistics of random lasers with resonant feedback. *Phys. Rev. Lett.*, 86:4524, 2005.

[40] P. Sebbah and C. Vanneste. Random laser in the localized regime. *Phys. Rev. B*, 66:144202, 2002.

[41] H. Cao. Lasing in random media. *Waves random media*, 13:R1–R39, 2003.

[42] H. Cao, X. Jiang, Y. Ling, J. Y. Xu, and C. M. Soukoulis. Mode repulsion and mode coupling in random lasers. *Phys. Rev. B*, 67:161101, 2003.

[43] S. Mujumdar, M. Ricci, R. Torre, and D. S. Wiersma. Amplified extended modes in random lasers. *Phys. Rev. Lett.*, 93:053903, 2004.

[44] H. Cao. Review on latest developments in random lasers with coherent. *J. Phys. A: Math. Gen.*, 38:10497–10535, 2005.

[45] L. I. Deych. Effects of spatial non-uniformity on laser dynamics. *Phys. Rev. Lett.*, 95:043902, 2005.

[46] K. van der Molen, A. P. Mosk, and A. Lagendijk. Intrinsic intensity fluctuations in random lasers. *Phys. Rev. A*, 74:053808, 2006.

[47] C. Vanneste, P. Sebbah, and H. Cao. Lasing with resonant feedback in weakly scattering random systems. *Phys. Rev. Lett.*, 98:143902, 2007.

[48] L. Dal Negro, J. H. Yi, V. Nguyen, Y. Yi, J. Michel, and L. C. Kimerling. Spectrally enhaced light emission from aperiodic photonic structures. *App. Phys. Lett.*, 86:261905, 2005.

[49] H. Lei, J. Chen, G. Nouet, S. Feng, Q. Gong, and X. Jiang. Photonic band gap structures in the Thue-Morse lattice. *Phys. Rev. B*, 75:205109, 2007.

[50] S. V. Boriskina and L. Dal Negro. Sensitive label-free biosensing using critical modes in aperiodic photonic structures. *Opt. Exp.*, 16:12511–12522, 2008.

[51] H. E. Tureci, H. G. L. Schwefel, P. Jacquod, and A. D. Stone. Modes of wave-chaotic dielectric resonators. *Prog. Opt.*, 47:75–138, 2005.

[52] H. E. Türeci, A. D. Stone, and B. Collier. Self-consistent multimode lasing theory for complex or random lasing media. *Phys. Rev. A*, 74:043822, 2006.

[53] H. Haken. *Light*. North-Holland, Amsterdam, Netherlands, 1985.

[54] Christine Y. Wang, L. Diehl, A. Gordon, C. Jirauschek, F. X. Kärtner, A. Belyanin, D. Bour, S. Corzine, G. Höfler, M. Troccoli, J. Faist, and Federico Capasso. Coherent instabilities in a semiconductor laser with fast gain recovery. *Phys. Rev. A*, 75:031802, 2007.

[55] M. Sargent, M. O. Scully, and W. E. Lamb. *Laser Physics*. Addison-Wesley, Reading, MA, 1974.

[56] J. Andreasen and H. Cao. Finite-difference time-domain formulation of stochastic noise in macroscopic atomic systems. *J. Lightwave Technol.*, 27:4530–4535, 2009.

[57] T. Harayama, S. Sunada, and K. S. Ikeda. Theory of two-dimensional microcavity lasers. *Phys. Rev. A*, 72:013803, 2005.

[58] A. Taflove and S. Hagness. *Computational Electrodynamics: The Finite-Difference Time-Domain Method*. Artech House, Boston, MA, USA, 3rd edition, 2005.

[59] C. Conti, M. Leonetti, A. Fratalocchi, L. Angelani, and G. Ruocco. Condensation in disordered lasers: theory, 3D+1 simulations and experiments. *Phys. Rev. Lett.*, 101:143901, 2008.

[60] H. Fu and H. Haken. Multifrequency operations in a short-cavity standing-wave laser. *Phys. Rev. A*, 43:2446–2454, 1991.

[61] H. Haken and H. Sauermann. Nonlinear interaction of laser modes. *Z. Phys.*, 173:261–275, 1963.

[62] Li Ge, R. J. Tandy, A. D. Stone, and H. E. Türeci. Quantitative verification of ab initio self-consistent laser theory. *Opt. Exp.*, 16:16895, 2008.

[63] H. E. Türeci, A. D. Stone, Li Ge, S. Rotter, and R. J. Tandy. Ab initio self-consistent laser theory and random lasers. *Nonlinearity*, 22:C1, 2009.

[64] J. Andreasen and H. Cao. Creation of new lasing modes with spatially nonuniform gain. 34:3586–3588, 2009.

[65] H. E. Tureci, Li Ge, S. Rotter, and A. D. Stone. Strong interactions in multimode random lasers. *Science*, 320:643–646, 2008.

[66] H. E. Türeci, A. D. Stone, and Li Ge. Theory of the spatial structure of nonlinear lasing modes. *Phys. Rev. A*, 76:013813, 2007.

[67] J. Andreasen, C. Vanneste, Li Ge, and H. Cao. Effects of spatially nonuniform gain on lasing modes in weakly scattering random systems. *Phys. Rev. A.*, 81:043818, 2010.

[68] J. D. Jackson. *Classical Electrodynamics*. Wiley, New York, US, 3rd edition, 1998.

[69] S. L. McCall and E. L. Hahn. Self-induced transparency. *Phys. Rev.*, 183:457–485, 1969.

[70] Jr. G. L. Lamb. Analytical descriptions of ultrashort optical pulse propagation in a resonant medium. *Rev. Mod. Phys.*, 43:99–124, 1971.

[71] L. A. Lugiato, G. L. Oppo, J. R. Tredicce, L. M. Narducci, and M. A. Pernigo. Instabilities and spatial complexity in a laser. *J. Opt. Soc. Am. B*, 7:1019–1033, 1990.

[72] K. Staliunas, M. F. H. Tarroja, and C. O. Weiss. Transverse mode locking, antilocking and self-induced dynamics of class-b lasers. *Opt. Commun.*, 102:69–75, 1993.

[73] P. Mandel, C. Etrich, and K. Otsuka. Multifrequency operations in a short-cavity standing-wave laser. *IEEE J. Quantum Electron.*, 29:836–843, 1993.

[74] V. Zehnlé. Theoretical analysis of a bimode laser. *Phys. Rev. A*, 57:629–643, 1998.

[75] P. L. Kapur and R. Peierls. The dispersion formula for nuclear reactions. *Proc. R. Soc. A*, 166:277–295, 1938.

[76] P. Yeh. *Optical waves in layered media*. Wiley, New York, USA, 1988.

[77] K Mohseni and T. Colonius. Numerical treatment of polar coordinate singularities. *J. Comput. Phys.*, 157:787–795, 200.

[78] Stefan Rotter. *Ballistic quantum transport at high energies and high magnetic fields*. PhD thesis, Vienna University of Technology, Austria, 2003.

[79] S. L. Adler and T. Piran. Relaxation methods for gauge field equilibrium equations. *Rev. Mod. Phys.*, 56:1–40, 1984.

[80] S. E. Koonin and D. C. Meredith. *Computational physics.* Addison Wesley, Massachusetts, 1990.

[81] P. C. Waterman. Symmetry, unitarity and geometry in electromagnetic scattering. *Phys. Rev. D*, 3:825–839, 1971.

[82] E. E. Narimanov, G. Hackenbroich, P. Jacquod, and A. D. Stone. Semiclassical theory of the emission properties of wave-chaotic resonant cavities. *Phys. Rev. Lett.*, 83:4991C4994, 1999.

[83] M. I. Mishchenko, L. D. Travis, and A. A. Lacis. *Scattering, Absorption, and Emission of Light by Small Particles.* Cambridge University Press, Cambridge, UK, 2002.

[84] A. I. Rahachou and I. V. Zozoulenko. Scattering matrix approach to the resonant states and Q values of microdisk lasing cavities. *Appl. Opt.*, 43:1761–1772, 2004.

[85] J. Wiersig. Boundary element method for resonances in dielectric microcavities. *J. Opt. A: Pure Appl. Opt.*, 5:53–60, 2003.

[86] B. Bidégaray. Time discretizations for maxwell-bloch equations. *Numer. Meth. Partial Differential Equations*, 19:284–300, 2003.

[87] T. Harayama, P. Davis, and K. S. Ikeda. Stable oscillations of a spatially chaotic wave function in a microstadium laser. *Phys. Rev. Lett.*, 90:063901, 2003.

[88] H. E. Türeci and A. D. Stone. Mode competition and output power in regular and chaotic dielectric cavity lasers. *Proc. SPIE*, 5708:255–270, 2005.

[89] Z. Liu and Y. Lai. Chaotic scattering in deformed optical microlasing cavities. *Phys. Rev. E*, 65:046204, 2002.

[90] Hakan E. Türeci and A. Douglas Stone. Mode competition and output power in regular and chaotic dielectric cavity lasers. *Proc. SPIE*, 5708:255–270, 2005.

[91] R. Schäfer, U. Kuhl, and H-J. Stöckmann. Directed emission from a dielectric microwave billard with quadrupolar shape. *New Jour. of Phys.*, 8:46, 2006.

[92] S. Lee, J. Yang, S. Moon, J. Lee, K. An, J. Shim, H. Lee, and S. W. Kim. Universal output directionality of single modes in a deformed microcavity. *Phys. Rev. A*, 75:011802(R), 2007.

[93] S. Shinohara, M. Hentschel, J. Wiersig, T. Sasaki, and T. Harayama. Ray-wave correspondence in limaon-shaped semiconductor microcavities. *Phys. Rev. A*, 80:031801, 2009.

[94] Q. Song, W. Fang, B. Liu, S. Ho, G. S. Solomon, and H. Cao. Chaotic microcavity laser with high quality factor and unidirectional output. *Phys. Rev. A*, 80:041807(R), 2009.

[95] A. J. Lichtenberg and M. A. Lieberman. *Regular and chaotic dynamics*. Springer-Verlag, New York, USA, 1992.

[96] L. E. Reichl. *The transition to chaos in conservative classical systems: quantum manifestations*. Springer-Verlag, New York, USA, 1992.

[97] W. R. Greenberg, A. Klein, I. Zlatev, and C. Li. From heisenberg matrix mechanics to semiclassical quantization: Theory and first applications. *Phys. Rev. A*, 54:1820–1837, 1996.

[98] A. D. Stone. Einstein's unknown insight and the problem of quantizing chaotic motion. *Phys. Today*, 58:37–43, 2005.

[99] H. E. Türeci. *Directionality and Vector Resonances of Regular and Chaotic Dielectric Microcavities*. PhD thesis, Yale University, USA, 2004.

[100] J. U. Nöckel, A. D. Stone, G. Chen, H. L. Grossman, and R. K. Chang. Directional emission from asymmetric resonant cavities. *Opt. Lett.*, 21:1609–1611, 1996.

[101] H. G. L. Schwefel, H. E. Türeci, A. Douglas Stone, and R. K. Chang. Progress in asymmetric resonant cavities: Using shape as a design parameter in dielectric microcavity lasers. *Optical Processes in Microcavities*, 2003.

[102] V. I. Arnold. *Mathematical methods of classical mechanics*. Springer, 1989.

[103] P. Y. Yu and M. Cardona. *Fundamentals of semiconductors: physics and materials properties*. Springer, New York, USA, 3rd edition, 2005.

[104] J. Faist, A. Tredicucci, F. Capasso, C. Sirtori, D. L. Sivco, J. N. Baillargeon, A. L. Hutchinson, and A. Y. Cho. High-power continuous-wave quantum cascade lasers. *IEEE J. Quantum Electron.*, 34:336–343, 1998.

[105] M. Hentschel, H. Schomerus, and R. Schubert. Husimi functions at dielectric interfaces: Inside-outside duality for optical systems and beyond. *Europhys. Lett.*, 62:636–642, 2003.

[106] Q. Song, Li Ge, H. Cao, A. D. Stone, J. Wiersig, J.-B. Shim, J. Unterhinninghofe, W. Fang, and G. S. Solomon. Directional laser emission from a wavelength-scale wave-chaotic microcavity. accepted by Phys. Rev. Lett., Jul. 2010.

[107] N. M. Lawandy, R. M. Balachandran, A. S. L. Gomes, and E. Sauvain. Laser action in strongly scattering media. *Nature*, 368:436, 1994.

[108] Masood Siddique, R. R. Alfano, G. A. Berger, M. Kempe, and A. Z. Genack. Time-resolved studies of stimulated emission from colloidal dye solutions. *Opt. Lett.*, pages 450–452, 1996.

[109] P. Sheng. *Introduction to Wave Scattering, Localization and Mesoscopic Phenomena*. Springer, Berlin, Heidelberg, 2nd edition, 2006.

[110] E. Akkermans and G. Montambaux. *Mesoscopic physics of electrons and photons*. Cambridge U. Press, New York, USA, 2007.

[111] Patrick A. Lee and T. V. Ramakrishnan. Disordered electronic systems. *Rev. Mod. Phys.*, 57:287–337, 1985.

[112] Sajeev John. Strong localization of photons in certain disordered dielectric superlattices. *Phys. Rev. Lett.*, 58:2486–2489, 1987.

[113] Diederik S. Wiersma and Ad Lagendijk. Light diffusion with gain and random lasers. *Phys. Rev. E*, 54:4256–4265, 1996.

[114] J. Fallert, R. J. B. Dietz, J. Sartor, D. Schneider, C. Klingshirn, and H. Kalt. Coexistence of strongly and weakly localized random laser modes. *Nat. Photon.*, 3:279–282, 2009.

[115] Y. D. Chong, Stefan Rotter, Li Ge, and A. D. Stone. Signature of random lasing in the diffusive regime. In preparation, Feb 2010.

[116] H. Kogelnik and C. V. Shank. Coupled-wave theory of distributed feedback lasers. *J. Appl. Phys.*, 43:2327–2335, 1972.

[117] A. Kudrolli, S. Sridhar, A. Pandey, and R. Ramaswamy. Coupled-wave theory of distributed feedback lasers. *Phys. Rev. E*, 49:R11, 1994.

[118] V. Milner and A. Z. Genack. Photon localization laser: Low-threshold lasing in a random amplifying layered medium via wave localization. *Phys. Rev. Lett.*, 94:073901, 2005.

[119] X. Wu, J. Andreasen, H. Cao, and A. Yamilov. Effect of local pumping on random laser modes in one dimension. *J. Opt. Soc. Am. B*, 24:A26–A33, 2007.

[120] T. Fukushima, T. Harayama, P. Davis, P. O. Vaccaro, T. Nishimura, and T. Aida. Ring and axis mode lasing in quasi-stadium laser diodes with concentric end mirrors. *Opt. Lett.*, 27:1430–1432, 2002.

[121] G. D. Chern, H. E. Tureci, A. D. Stone, R. K. Chang, M. Kneissl, and N. M. Johnson. Unidirectional lasing from ingan multiple-quantum-well spiral-shaped micropillars. *Appl. Phys. Lett.*, 83:1710–1712, 2003.

[122] J. Wiersig. Formation of long-lived, scarlike modes near avoided resonance crossings in optical microcavities. *Phys. Rev. Lett.*, 97:253901, 2006.

[123] J. Wiersig. Goos-Hänchen shift and localization of optical modes in deformed microcavities. *Phys. Rev. Lett.*, 78:016201, 2008.

[124] Y. D. Chong, Li Ge, H. Cao, and A. D. Stone. Perfect coherent absorbers. *Phys. Rev. Lett.*, 105:053901, 2010.

[125] Li Ge, H. E. Türeci, and A. D. Stone. Mode selection and output power increase in quadrupole laser cavities. In preparation, Feb 2010.

[126] Li Ge, Y. D. Chong, H. Cao, and A. D. Stone. Gain controlled states in one-dimensional laser cavities. In preparation, Feb 2010.